Master's thesis

NTNU
Norwegian University of Science and Technology
Faculty of Information Technology and Electrical Engineering
Department of Computer Science

Salar Adel

Towards Automatic Inspection in Additive Manufacturing using Computer Vision

Master's thesis in Computer Science
Supervisor: Frank Lindseth
Co-supervisor: Mathias Hauan Arbo & Eirik Njåstad
June 2023

NTNU
Norwegian University of
Science and Technology

Salar Adel

Towards Automatic Inspection in Additive Manufacturing using Computer Vision

Master's thesis in Computer Science
Supervisor: Frank Lindseth
Co-supervisor: Mathias Hauan Arbo & Eirik Njåstad
June 2023

Norwegian University of Science and Technology
Faculty of Information Technology and Electrical Engineering
Department of Computer Science

NTNU
Norwegian University of
Science and Technology

Abstract

The advancement of Additive Manufacturing systems has led to increased complexity in the wider diversity of materials and enhanced Degrees of Freedom, which has caused an increased interest in potentially solve some of the industry's challenges related to repairs and production. However, these systems do have few integrated inspection capabilities to both evaluate the quality and monitoring the manufacturing process. The use of computer vision in Directed Energy Deposition has traditionally been concentrated on various camera technologies and setups, each specially tailored to a specific Additive Manufacturing system. These methods have demonstrated potential for in-process monitoring, error detection and correction. Nevertheless, research remains limited in terms of fully integrating inspection systems with Additive Manufacturing processes utilizing robot manipulators, and comprehensively exploring the challenges associated with using computer vision on diverse metal types and geometric shapes. In this thesis, a novel framework is proposed to be integrated with a Directed Energy Deposition system, to enable real-time automated inspection during the manufacturing process. This framework utilizes 3D reconstruction to examine height disparities, providing insights and potential possibilities for optimizing in the manufacturing process. Furthermore, incorporating a 3D reconstruction method that takes advantage of the capabilities of both a laser line scanner and a robotic manipulator, which expands the possibilities for inspection options. Lastly, the measured errors were experimentally leveraged, with correction made to achieve the target height of a manufactured test specimen. These results contribute to the field, offering an approach for automated inspection in Additive Manufacturing processes.

Sammendrag

Utviklingen av additiv produksjon har ført til økt kompleksitet på grunn av et større utvalg av materialer og utvidede frihetsgrader i systemene. Dette har økt interessen når det gjelder å løse noen av de industrielle utfordringene, inkludert både reparasjoner og produksjon. Imidlertid har disse systemene har per nå ingen innebygde inspeksjonsmuligheter for å både kvalitetskontroll og overvåke produksjonsprosessen. Gjennom utviklingen av additiv tilvirkning i metall, har unike oppsett med bruk av forskjellige kamerateknologier blitt anvendt for å utnytte ulike metoder innenfor datasyn. Disse metodene har vist potensiale for overvåking under prosessen, feildeteksjon og korrigering. Det er imidlertid fortsatt begrensninger når det gjelder fullstendig integrering av inspeksjonssystemer med additive tilvirkning som benytter seg av bruken av robotmanipulatorer med høyere frihetsgrader. Det gjenstår mye å utforske både når det gjelder additive tilvirkning som benytter seg av robotmanipulatorer, og de ulike utfordringene knyttet til bruk av strukturert lys på ulike metaller og geometriske former. I denne oppgaven foreslås det et innovativt rammeverk integrert med i et system for Directed Energy Deposition, som muliggjør automatisert inspeksjon av produksjonsprosessen i sanntid. Dette rammeverket benytter 3D-rekonstruksjon for å undersøke høydeforskjeller, forbedre overvåkingen av prosessen, og identifisere potensielle muligheter for optimalisering av parametere i produksjonsprosessen. Videre har det blitt benyttet en metode som muliggjør 3D-rekonstruksjon ved å kombinere en laserlinjeskanner og en robotmanipulator med flere frihetsgrader. Til slutt ble høydeavvikene målt i prosessen, og det ble utført eksperimentelle korreksjoner for å utforske muligheten for å oppnå ønsket produksjonshøyde på testobjekter. Disse resultatene har betydning innen fagfeltet og presenterer en metode for automatisert inspeksjon i additive tilvirkningsprosesser.

Preface

The following pages constitute my master thesis on using computer vision for automatic inspection in Additive Manufacturing. This thesis is the final part of a 2-year master's degree in Computer Science at Norwegian University of Science and Technology (NTNU). My supervisors have been Frank Lindseth from the Department of Computer Science and Mathias Hauan Arbo and Eirik Njåstad from the department of Manufacturing Technology at SINTEF Manufacturing.

I consider myself immensely fortunate to have spent the past year engaged in such an intriguing field of study. My gratitude extends to Mathias Hauan Arbo and Eirik Njåstad, who generously provided me with an opportunity to delve deep into this captivating subject and challenge myself. This experience broadened my awareness of a range of engineering topics and provided me with the opportunity to meet a lot of amazing people.

I would like to thank my supervisors Frank Lindseth, Mathias Hauan Arbo and Eirik Njåstad for their help and guidance during the writing of this thesis. They have provided me with the guidance and help with experimental setup for the conducted experiments of this thesis. I would also like to thank my family and friends for their support and motivating words during this semester.

Salar Adel

Trondheim. 22nd June 2023

Contents

Abstract **iii**
Sammendrag **v**
Preface **vii**
Figures **xiii**
Tables **xvii**
Acronyms **xx**
Glossary **xxi**
1 Introduction **1**
1.1 Motivation . . . 2
1.2 Goal and Research Question . . . 4
1.3 Research Method . . . 5
1.4 Contributions . . . 6
1.5 Thesis Outline . . . 7
2 Background and Related Work **9**
2.1 Additive Manufacturing . . . 10
2.1.1 Additive Manufacturing Process . . . 11
2.2 Robot Manipulator . . . 15
2.2.1 Types of Robot Manipulators . . . 15
2.2.2 Articulated Robot Kinematics . . . 16
2.3 Directed Energy Deposition with an Articulated Robot Manipulator 18
2.4 Computer Vision . . . 20
2.4.1 Capturing and Representing Visual Data . . . 20
2.4.2 Camera Calibration . . . 24
2.5 Point Clouds Registration . . . 27
2.5.1 Iterative Closest Point . . . 27
2.5.2 Random Sample Consensus . . . 29
2.6 3D Reconstruction using Laser Scanner . . . 31

2.7 Related Work . . . 33
2.7.1 Error Detection for Cartesian 3D Printer . . . 34
2.7.2 Height Correction through Layer Addition or Removal . . . 35
2.7.3 Error Correction based on Working Distance . . . 36
2.7.4 Conclusion on Related Work . . . 37
3 Method **39**
3.1 Overview of Prior Studies . . . 39
3.1.1 Exploration of Previous Framework . . . 40
3.1.2 Insights and Key Findings . . . 42
3.2 Selecting Deviation Properties to Inspect . . . 43
3.3 Choosing the Hardware . . . 43
3.4 VC Nano 3D-Z . . . 44
3.4.1 Pipeline for Creating VC Nano 3D-Z Profiles . . . 45
3.5 Exploring Impact of Metal types and Geometry on Reflectivity . . . 46
3.5.1 Optimization based on Error Metrics . . . 47
3.6 Vision-Based Inspection Framework Design . . . 48
3.6.1 Data Acquisition and 3D Reconstruction . . . 49
3.6.2 Pre-processing and Fine-tuning RANSAC Parameters . . . 51
3.6.3 Plane Estimation and Alignment . . . 52
4 Experiments and Result **55**
4.1 Experimental Plan . . . 55
4.2 Experiment 1: Optimizing VC Nano 3D-Z for different Metals . . . 57
4.2.1 Setup . . . 57
4.2.2 Results . . . 59
4.2.3 Discussion . . . 67
4.3 Experiment 2: Top Layer Inspection with VC Nano 3D -Z . . . 70
4.3.1 Setup . . . 70
4.3.2 Results . . . 71
4.3.3 Discussion . . . 75
4.4 Experiment 3: Layer-wise Height Deviation in a Manufacturing Process . . . 77
4.4.1 Setup . . . 77
4.4.2 Results . . . 77
4.4.3 Discussion . . . 81
4.5 Experiment 4: Height Optimization in a Manufacturing Process . . . 82

4.5.1 Setup . . . 82
4.5.2 Results . . . 82
4.5.3 Discussion . . . 85
5 Discussion **87**
5.1 Evaluation on Measuring Method . . . 87
5.2 Experimentation Failures and Improvements . . . 88
5.3 Research Questions . . . 89
6 Conclusion and Future Work **93**
6.1 Conclusion . . . 93
6.2 Future Work . . . 94
6.2.1 Improved 3D Reconstruction . . . 94
6.2.2 Impacts of Varied Shapes on Scanning Quality . . . 95
6.2.3 Investigating the Correlation between Layer Height and Expected Height . . . 96
6.2.4 Enhancing Automation in Detection and Calibration . . . 97
Bibliography **99**
A Supplementary Visual Representations for Experiment 1 **105**
A.0.1 Heatmap for Double Shutter 1 and 2 . . . 105
A.0.2 Visualization for each Exposure Mode . . . 110
B Registration with ArUco Markers **115**
C Sub-experiment: Assessing the Maximum Build Height **117**
C.1 Results . . . 117
D Prior Study of Specialization Project **123**
E RANSAC Plane Alignment **125**
F Draft of Conference Paper **127**

List of Figures

2.1 General Additive Manufacturing Pipeline 12
2.2 Difference between CAD and STL format 13
2.3 Slicing a Solid Geometry into layers with Varying Thicknesses . . 14
2.4 Workspace of a Cartesian and Articulated robot 16
2.5 Relationship between Forward and Inverse Kinematics 17
2.6 Workspace of Cartesian and Articulated robot manipulator 19
2.7 Directed Energy Deposition system at SINTEF Manufacturing . . 20
2.8 A simple illustration of a Pinhole Model. 21
2.9 Conversion of World Frame to Image Plane 23
2.10 The effect of Radial Distortion 24
2.11 The effect of Tangential Distortion. 24
2.12 An example of Eye-to-Hand and Eye-in-Hand Calibration 26
2.13 Examples of ArUco marker with IDs 0,1,2,3. 26
2.14 Simple example of ICP algorithm of two Line sets 28
2.15 Plane fitting for RANSAC algorithm 31
2.16 Illustration of a Laser Line Scanner's output. 32
2.17 Path Optimization of Laser Line Scanner on Aluminium 32
2.18 Outliers generated from Specular Reflection 33
2.19 Point Cloud Registration between two Point Clouds 34
2.20 Example of comparing of the Theoretical and Expected height . . 36
2.21 Example of a Height Controller 37

3.1 Prior Framework from the Specialization Project 40
3.2 Comparison of Laser Line Scans and Sampling Distribution 42
3.3 Choice of Hardware 44
3.4 Example of the output of a Laser Line Scanner 45
3.5 Illustration of the 3D reconstruction 50

3.6 Illustration of Plane Estimation and Alignment 52

4.1 Experiment 1 and 2 Setup 58
4.2 Scanned Plates for Experiment 1 59
4.3 Example of determining the best Shutter Time for Plate B 66
4.4 Illustration of Exposure Mode 0, 1 and 2 of Plate A 69
4.5 Cubes Manufactured for Experiment 2 71
4.6 Illustration of the 3,5 and 7-layered cube's Height deviation 72
4.7 Frequency plots of 3, 5, and 7-layered cubes 73
4.8 Frequency distances between the Cube 74
4.9 Toolpath generated from Slic3r 75
4.10 Illustration of the correlation of Cube Height and Layer Height . . 76
4.11 Experiment 3 result of Manufactured Cube 78
4.12 Visualization of Top Layer deviation relative to the Base 78
4.13 Results of height deviation relative to Base 79
4.14 Height differences between Consecutive Layer Pairs 80
4.15 Video Result: QR Code for Experiment 3 Result 81
4.16 Manufactured Cubes for Experiment 4 83
4.17 Base Plate Tilt Correction from Experiment 4 85
4.18 Illustration of rounding effect on the Top Layer 86

A.1 Heatmap for Plate A 106
A.2 Heatmap for Plate B 107
A.3 Heatmap for Plate C 108
A.4 Heatmap for Plate D 109
A.5 Capture with Exposure mode 0 and 1 for Plate A 110
A.6 Different configurations with Exposure mode 2 for Plate A 110
A.7 Capture with Exposure mode 0 and 1 for Plate B 111
A.8 Different configurations with Exposure mode 2 for Plate B 111
A.9 Capture with Exposure mode 0 and 1 for Plate C 112
A.10 Different configurations with Exposure mode 2 for Plate C 112
A.11 Exposure mode 0 and 1 for Plate D 113
A.12 Different Configurations with Exposure mode 2 for Plate D 113

B.1 Illustration of Utilizing Rotation Table and ArUco Markers 116

C.1 Illustration of the manufactured cube and 3D reconstruciton. . . . 118
C.2 For every 5th layer, measured the error relative to the Base 119
C.3 Visualizing falling pixels from the Projection of XZ plane 120
C.4 Visualizing falling pixels from the Projection of YZ plane 121

D.1 Testing Setup using Rotation Table and VC Nano 3D-Z 124

List of Tables

2.1 Taxonomy for the DED system at SINTEF Manufacturing 11

3.1 Experimental Configurations of VC Nano 3D-Z 47
3.2 RANSAC Parameters 51

4.1 Overview of the Experiments 56
4.2 Metal Types for Experiment 1 58
4.3 Best Shutter Times for each Plate 60
4.4 Best RLC Threshold for each Plate 62
4.5 Best Exposure Modes for each Plate 64
4.6 Comparison of each Cube and Mesh Height 72
4.7 Measured cubes for Experiment 4 84

Acronyms

AM Additive Manufacturing. iii, vii, xx, xxi, 1–4, 7, 9–15, 18, 33–35, 37, 89, 90

CAD Computer-Aided Design. xx, xxi, 1, 11–13, 34, 35

DED Directed Energy Deposition. iii, v, xx, 1–6, 9, 11, 16, 18–20, 33–40, 43, 52, 55–57, 70, 75, 77, 80, 82, 85, 87, 89, 90, 93–95, 97, 115, 117, 123

DH Denavit-Hartenberg. xx, 17

DOF Degrees of Freedom. iii, xx, 2, 14–16, 18, 19, 38, 42, 49, 56, 89, 93

ICP Iterative Closest Point. xx, 27, 28, 34, 40–42, 53, 89

ISO International Organization for Standardization. xx, 12, 14

MAE Mean Absolute Error. xx, 34

MSE Mean Squared Error. xx, 27, 28, 120, 121

NURBS Non-Unfirorm Rational Basis Spline. xx, 12

PID Proportional-Integrative-Derivative. xx

PLA Polylactic Acid. xx, 70

RANSAC Random Sample Consensus. xvii, xx, 27, 29–31, 40–42, 49, 51, 52, 75, 77–79, 81, 82, 84, 85, 88, 89, 91, 120, 121, 125

RMSE Root Mean Square Error. xx, 34

STEP Standard for the Exchange of Prdouct Data. xx, 12

STL Standard Tessellation Language. xx, 11, 13, 14, 40–42, 48, 49, 52, 56, 70–72, 75–77, 81, 88, 89, 91

Glossary

Additive Manufacturing	An Additive Manufacturing is described as a construction of a 3D object by incrementally adding material.
CAD	Stands for Computer-Aided Design. It refers to the 3D digial model created from a computer software.
Degrees of Freedom	Number of independent variables that describe a mechanical system's possible locations in space.
Directed Energy Deposition	An Additive Manufacturing process, also reffered to as metal printing which focuses thermal energy to melt and fuse deposited metal.
ICP	An algorithm typically used for aligning two 3D point clouds to minimize the Euclidean distance between them.
RANSAC	A mathematical model-based approach for aligning and recognizing objects within a set of observed data. It is especially effective when the data contains outliers.
STL	It describes the surface geometry of a 3D object using a mesh of triangles.

Chapter 1

Introduction

Additive Manufacturing (AM) also known as 3D printing, is the process that incrementally constructs an object from a Computer-Aided Design (CAD) model by adding material layer by layer. The system uses these digital models to direct the print head or other mechanisms to incrementally layer the material to the object. A range of materials can be processed in these type of systems, including various plastics and metals. Compared to other conventional manufacturing techniques, AM offers a number of benefits, including design freedom to create more complex geometry and reduced material waste. AM is a rapidly developing field that is gaining ground in industry and is anticipated to play a significant role in the future. Most industrial parts are manufactured using a range of different type of metals. Consequently, industries have displayed considerable interest in recent advancements in metal printing using Directed Energy Deposition (DED) technology. One of the reasons for this interest is that it can address a common industrial challenge, concerning defective spare parts. Usually, requesting new spare parts needs to be ordered from a distant manufacturer. However, this process can be time-consuming, and particularly if the part is not directly available from the specific manufacturer. In contrast, a DED system can produce these components within hours in a wide range of metals. For example, Equinor is one of the companies actively investigating the use of AM to face this challenge [1]. Nevertheless, the industry has not fully adopted AM technology due to a variety of difficulties

with quality control to satisfy production standards. This is especially true for DED processes, which is a highly complicated system with numerous parameters that are easily influenced and may result in unforeseen issues with the created object's interior structure. Therefore, integrating inspection capabilities into the process would be beneficial to enhance and expand the use of AM technology. There is currently no off-the-shelf technology for automatic inspection for quality control that is integrated in the feedback control in AM to increase the quality of the manufactured object. Therefore, this thesis will explore the opportunities of adapting computer vision into a DED process for inspecting the manufacturing process, and to explore future possibilities to use computer vision as sensor feedback for optimizing build parameters to detect deviation and to increase the quality.

1.1 Motivation

To improve the quality of manufactured parts, SINTEF Manufacturing has investigated the use of closed-loop methodologies within metal printing processes utilizing DED technology from MELTIO. They have been combining a MELTIO system on a KUKA Industrial robot arm to create this setup in order to do research on manufacturing repairs, feature addition, and printing of more complicated structures than available with conventional techniques. Using a MELTIO system, metal products are produced by focusing many lasers on a single focal point to form a melt pool into which additional material is injected. Unlike most conventional 3D printers, which only have 3 Degrees of Freedom (DOF), the industrial KUKA robot is equipped with a 6 DOF robot arm and an additional 2 DOF rotation table. By using a KUKA Industrial robot into the DED process will increase Degrees of Freedom to provide toolpaths more design flexibility. However, this enhancement introduces intricacies that can escalate the likelihood of inaccuracies, a tendency particularly noticeable in emerging technologies such as DED systems. It is therefore highly desirable to have a way for inspecting the manufactured part. These potential flaws highlight the critical need for a comprehensive inspection mechanism to assure the quality and precision of manufactured parts.

Recent research has offered various methods for reducing these variances, including parameter optimization, product design changes, and online monitoring.

Regardless, in order to use any of these tactics, the evaluation of part accuracy between the manufactured object and the desired object is a must for determining each strategy's effectiveness [2]. There are numerous approaches and techniques for determining how accurate a manufactured part is. By investigating technologies for surface reconstruction, photogrammetry, and structured light methods, it is now possible to create precise 3D reconstructions of manufactured parts using the most recent developments in 3D scan technology for producing digital point clouds. The research goal is to create a vision-based framework for SINTEF Manufacturing's DED system that will enable automatic inspection of manufactured parts using computer vision methods to further improve quality control output and also advancing the research into vision-based automatic inspection in AM.

SFI Manufacturing is a centre for research-based innovation for competitive high-value manufacturing [3]. SFI Manufacturing seeks to show that innovative and environmentally friendly manufacturing is possible in high-cost countries. The study that was done for this thesis, together with the findings, is a part of a wider AM research project for SFI Manufacturing. Previously in SFI Manufacturing, research has focused on the use of wire-arc Directed Energy Deposition in an open-loop system [4], but the literature review and simulation study conducted by Moltumyr et al. [5] highlight the potential of a vision-based closed-loop system for applications in metal-based Additive Manufacturing.

During a summer internship in 2022, an exploration was initiated to assess the possibility of incorporating automatic inspection into the DED system at SINTEF Manufacturing. There were two complementary research topics. The first topic, which is the basis of this thesis, explores the potential of automatic inspection, while the second topic delves into the development of toolpath planning that fully utilizes the multi-axis robot manipulator in a DED process. The summer was spent better understanding and laying the framework for the research, as well as becoming acquainted with the multi-axis robot manipulator. The research was continued as a specialization project in Fall 2022 to create an outline of the components required to build an automatic inspection framework utilizing computer vision. This thesis will further investigate the issues associated with previous experiences with building a vision-based framework for DED systems utilizing a robot manipulator, as well as lay the groundwork for future work. The long-term goal is to merge the two research aspects of automatic inspection and trajectory planning to have a closed-

loop system which can manufacture higher quality objects than currently available with DED systems.

1.2 Goal and Research Question

The overall goal and the research questions are based on what was learned from the prior specialization project [6]. The overall goal of the thesis is the following:

- **Goal:** *Develop a vision-based framework for fully automated inspection within a DED system for enhancing the quality of fabricated objects.*

Despite the goal being fairly broad and intricate, the main objective should at least briefly describe some of the difficulties involved in constructing a vision-based framework for automatic inspection in AM. Our objective is to build upon existing knowledge in order to develop a framework infrastructure that lays the groundwork for potential future integration of a closed-loop system within a DED system. Our proposed framework should consist of multiple stages, such as 3D reconstruction, point cloud generation, camera calibration, and identify height deviations. The end result should be utilized to provide a qualitative and quantitative assessment of height deviations, ultimately aiming to minimize geometric discrepancies. To develop a robust vision-based framework, we will explore the following research questions (RQ):

- **RQ1:** *What are the main challenges of constructing an automatic vision-based framework for a DED system?*

The development of a vison-based framework for automatic inspection remains a relatively uncharted territory, necessitating extensive experimentation. Addressing these challenges and highlighting results from the experiments will help to bring the field forward.

- **RQ2:** *To what extent do variation in geometric complexity and metal types influence structured light-based 3D reconstruction?*

A significant challenge in utilizing structured light for DED processes, is the diverse range of metal types and various geometrical shapes. These properties affect how light interacts with the manufactured object and can lead to inaccurate 3D reconstruction. Investigating the effect of various metal types and geometric shapes can help to develop new strategies to reduce the generated outliers. Due to the fact that 3D reconstruction is based on structured light might disclose issues while limiting the effect in the process. This study may also aid in the design and development of improved methods for using structured light based 3D scanning methods on metal.

- **RQ3:** *How can height deviation data optimize parameters to reduce defects and enhance product quality?*

The height deviation data compares the scanned top surface of an object and compares it with the design part. This data can be used to improve object design and lower internal and external error. The measurement and correction of manufacturing process defects can also reduce flaws and variations in the final manufactured part, which could also serve as a feedback loop for future research.

1.3 Research Method

The thesis goal will be achieved by examining the available literature and conducting experiments. The results from the experiments will be used to examine findings qualitatively and quantitatively through generated data resources gained from each experiment. The experiments conducted are each carefully designed to explore the different aspects of investigating manufactured objects in a DED process. Each experiment throughout this thesis will contribute valuable insights towards enhancing the final framework and thereby address the provided research questions.

1.4 Contributions

We propose a vision-based framework for automatic inspection in a DED processes. This framework will use a robot manipulator and a cost-effective laser line scanner to inspect any height deviation during the manufacturing process. Utilizing both the existing axes in the robot manipulator and structured light-based methods. Our suggested approach would deal with the issues related to inspection of geometric deviation by incorporating a framework for examining the height using 3D reconstruction, then analysing these to examine the manufactured object's quality for future process parameter optimization. Our contributions are summarized as followed:

1. A framework for performing in-process inspections within DED processes, highlight some of the inherent challenges to overcome.

2. Discuss the limitations of using structured light methods within DED processes.

3. Highlight challenges of the framework and chosen methods in order to set a path for future research and development for improving inspection possibilities in DED processes.

4. The writing of a conference paper based on the experiments and findings during this master thesis work (work in progress, early stage)

Most of the code in this thesis is included. The code follows a single module for repetitive algorithms for simplicity, testing, and visualization. Furthermore, each experiment is organized into separate folders with the data generated, accompanied by a designated run script that produces the corresponding results. Additionally, a video file is included to showcase the final result of the framework incorporated into the DED system. The video can also be accessed through the following link: `https://youtu.be/FafU_0GgmvA`. However, it is important to note that the code for the hardware and robot functions is excluded as it belongs to SINTEF Manufacturing.

1.5 Thesis Outline

The thesis is structured into six chapter, and are organized in the following order:

- **Chapter 1: Introduction**, will introduce the topic, motivation, and research area.
- **Chapter 2: Background and Related Work**, provides an introduction to the key topics in this thesis. It introduces the concepts of Additive Manufacturing processes, robot manipulators, and computer vision, along with an introduction to point cloud algorithms and 3D reconstruction. Additionally, it also offers a review of previous works and studies that align closely with the topics of this thesis.
- **Chapter 3: Method**, delves into an exploration of the methodology employed for conducting the experiments. This chapter contains a full analysis of the methods employed, as well as the experimental design ideas and hardware utilized throughout the experimentation in Chapter 4.
- **Chapter 4: Experiments and Result**, will present setup, results and the discussions for each individual experiment.
- **Chapter 5: Discussion**, will discuss the overall framework and findings from Chapter 4.
- **Chapter 6: Conclusion and Future Work**, concludes the thesis and suggests various possible directions for future research.
- **Appendix F: Draft of Conference Paper**, an initial draft of the conference paper.

Chapter 2

Background and Related Work

The following thesis will explore multiple research topics related to construction of a vision-based framework for automatic inspection in an Additive Manufacturing process. This chapter will firstly introduce the AM process, and then give a basic foundation of types of robot manipulators related to AM. Then, we will introduce the technology employed in these areas to develop the system we are working with at SINTEF Manufacturing, starting with a fundamental foundation in robotics and the AM process. Later on, the topic of computer vision will be explained together with point cloud registration and 3D reconstruction. Lastly, we will discuss the related research on using vision-based methods for automatic inspection in a DED process to give the reader a better understanding of the research area in this thesis.

This chapter is a continuation of a specialization project [6]. Also, parts of this chapter assume prior familiarity with basic robotic kinematics and computer vision. Therefore, we refer the reader to the following books for a more comprehensive understanding of the topics in this thesis, "Modern Robotics: Mechanics, Planning, and Control" [7] and "Computer Vision Algorithms and Applications" [8].

2.1 Additive Manufacturing

The use of Additive Manufacturing, colloquially known as 3D printing, has completely changed how products are created, from conception to final product. Using digital design files, Additive Manufacturing creates objects by gradually building them, often layer by layer, as opposed to traditional subtractive manufacturing techniques, which involve removing material from a solid block to produce a final product. According to ISO/ASTM 52900 [9], AM is defined scientifically as:

> *"A process of joining materials to make objects from 3D model data, usually layer upon layer, as opposed to subtractive manufacturing methodologies"*

The rapid advancement of Additive Manufacturing technology has resulted in a wider selection of methods, process, and materials options for manufacturing. The term "Additive Manufacturing" is often used interchangeably with "3D printing", which related to the typical consumer 3D printers. While both methods involve the creation of three-dimensional items, the term Additive Manufacturing is broader and covers a variety of methods, including ones that employ equipment that are more advanced than regular consumer 3D printers. For the context of this thesis, these terms need to be clearly defined to ensure our scientific area of exploration. To distinguish these terminologies, we will employ Klas Boivie's [10] description of a taxonomy for more precise identification of AM processes in ISO/ASTM 52900 [9], which is separated into three categories: *Process Category*, *Distinctive process characteristics*, and *Materials processed*. From this terminology, we can define an exact taxonomy for the AM system we are researching, as summarized in Table 2.1.

Table 2.1: Taxonomy for the DED system at SINTEF Manufacturing, which encompasses the materials being currently studied and tested in this thesis.

Method Code	**Process Category**	**Distinctive Process Characteristics**	**Materials Processed**
DED-LB/LCSS, DSS	Directed Energy Deposition (DED)	Laser-based (LB) melting of metal powder or wire to deposit material layer by layer	Low Carbon Stainless Steel (LCSS), Duplex Stainless Steel (DSS)

The process category explored in this thesis is Directed Energy Deposition processes, and the term 3D printing and Additive Manufacturing will be used to describe this process. For a more comprehensive understanding of the differences between Directed Energy Deposition and other Additive Manufacturing processes, Bikas et al. [11] provides a summary and comparison of different manufacturing processes.

2.1.1 Additive Manufacturing Process

A broad range of AM processes employs the same general pipeline, and consists of several steps. The first step is to create a 3D digital model of the object using Computer-Aided Design software or other 3D modelling tools. Once the 3D digital model is complete, it must be converted into a format that can be read by a 3D printer or accompanying software for defining the toolpaths. The most commonly used format for 3D printing is the Standard Tessellation Language (STL) format, which represents the model as a triangulated mesh of connected points and surfaces. The STL format, established by 3D Systems Inc. [12] in 1987, has become an industry standard for AM operations despite the fact that there are other representation formats for CAD models and specifically for AM operations such as 3mf [13].

The final step is to prepare the model for printing by slicing it into planar surfaces or layers. This is done using software called a slicer, which converts the model into a set of machine instructions called G-code. The G-code tells the robot manipulator how to move the tool, what temperature to use, or other settings, so

that the object is manufactured correctly [14]. Figure 2.1, illustrates all of these steps, providing an overview of the 3D printing process from start to finish.

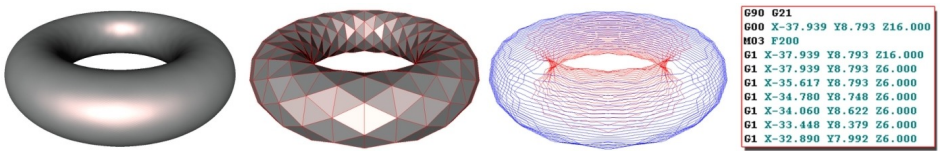

Figure 2.1: Example of a general AM pipeline. **Left**: A CAD model. **Center-left**: Converted CAD model into STL. **Center-right**: Sliced model that illustrates the toolpath. **Right**: G-code for the toolpath. **Image Source:** [14]

Modelling

The initial step in the AM pipeline involves creating a digital model with a CAD software. This advanced modelling software allows users to design complex geometries by representing curves and surfaces with base splines. The software also makes use of the Non-Unfirorm Rational Basis Spline (NURBS) concept, which gives a versatile and precise way of constructing complex shapes. With the emergence of numerous CAD programs and file formats, a new standardized format was introduced to enable the exchange of CAD models across different software systems. This format was developed by the International Organization for Standardization (ISO) in 1994 and is a part of the standard ISO 10303 [15]. The format, commonly referred to as Standard for the Exchange of Prdouct Data (STEP) [16], specified in ISO 10303-21 [17] was specifically designed for storing CAD models defined by ISO 10303. STEP provides a universal language for storing and sharing CAD models, allowing multiple users to easily exchange files across different enterprise software platforms. By standardizing the format of CAD models, STEP has significantly streamlined the process of sharing and collaborating on designs in the engineering and manufacturing industries.

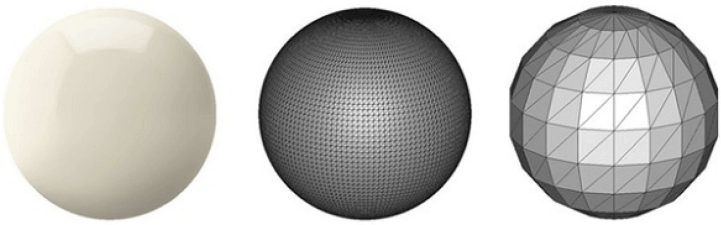

Figure 2.2: The difference between the quality of a CAD and STL model. **Left:** CAD model. **Center:** High Resolution STL model. **Right:** Low Resolution STL model. **Image Source:** [18]

When creating a 3D model for manufacturing in Additive Manufacturing, it must be converted into a slicing-compatible format. STL is a popular format that uses triangle facets to describe the model's surface geometry. The STL format was created primarily for 3D printing and is available as both ASCII and binary code. When converting a 3D model to an STL file, the surface geometry of the model is triangulated, which might result in a loss of information when compared to the original model, as seen in Figure 2.2. In contrast, OBJ files store 3D models as a set of vertices, edges, and faces [19], without a specific requirement for the surface geometry to be represented as triangular facets. This means that OBJ files can store more complex geometries, such as curved surfaces, without requiring them to be simplified into triangles. However, when converting an OBJ file to an STL file, the geometry must be triangulated to fit the requirements of the STL format, which can result in a loss of detail.

Slicing

The STL files are being used to build contour data. The slicing procedure is carried out in accordance with the desired layer thickness, with the layer being typically planar surfaces. A wide variety of AM processes utlize machine instructions or commonly known as G-code to execute the tool motion and control steps. When compared to alternative representation formats, this format does present some difficulties that could result in lower quality output for produced parts. The thickness between the slices can be varied depending on the capabilities of the type of manipulator and the shape being generated. Surface finishing degrades as layer thickness increases. Figure 2.3 illustrates the variations in slicing thickness

and detail. Given the versatility of material extrusion, which allows for alterations in layer height and thickness, it is likely that slicing parameters would need to be adjusted depending on the specifics of the AM process.

Figure 2.3: An example of slicing a solid geometry into horizontal layers with varying thicknesses. Thinner layers produce higher resolution objects but take longer to manufacture, whereas larger layers produce lower resolution objects but take less time to manufacture. **Image Source:** [20]

Machine Instruction

The final step of the AM pipeline involves generating G-code or machine instructions that will be used by the AM system. This process converts the STL to G-code to create a set of instructions that can be executed by the machine. The G-code format offers information for positioning, line motion, and contouring control systems, according to ISO 6983 [21]. In the instruction set, each command starting with G represents the geometry or M for an instruction in the machine. Machine-specific functions are handled by machine instructions, and material extrusion and positioning are handled by geometry commands. Under certain conditions, the toolpath might be determined by the unique kinematics of the robot, defining it independently of the standard G-code instruction set. This often comes into play when dealing with robot programming languages such as the KUKA Robot Language or other proprietary languages specific to different manufacturers. These custom languages offer the capacity to implement machine instructions that can effectively control and access systems with higher Degrees of Freedom, thus broadening the potential for more complex and dynamic robotic operations.

2.2 Robot Manipulator

A robotic manipulator is made up of a set of joints that are connected together by a rigid structure designed to interact with their environment. The term manipulation refers to operations performed by the robot such as picking and positioning an object, gripping, releasing, interacting with the applicable environment, and carrying objects within its working region [22]. A robot manipulator's kinematics include the use of sensors and actuators, which provide real-time feedback on the manipulator's location, velocity, and force. For the robot manipulator to work ideally, the interaction between the sensors and actuators determines the precision and accuracy. The actuators are driven using control systems that utilize advanced control strategies and algorithms to achieve the desired motion. There are a lot of different robot manipulator, but this thesis will mainly focus on *articulated* and *cartesian robot manipulators*.

2.2.1 Types of Robot Manipulators

With industrial robots becoming more widespread in manufacturing environments, there has been an increased demand for numerous different types of industrial robots to accommodate specific applications and industries. To distinguish the various robot manipulator systems, we will primarily focus on Cartesian robots, which are utilized in commercial 3D printing, and articulated robots, commonly referred to as robot arms. Each method operates differently and has its own distinct work envelope, as shown in Figure 2.4.

The Cartesian robots, shown in Figure 2.4a, work exclusively in XYZ coordinates. These type of robots are frequently utilized in standard AM operations. Due to their high accuracy and precision, these robots are often used in AM techniques such as 3D printing. 3 linear DOF of the x, y, and z axes of a Cartesian coordinate system, are present in Cartesian robots. This suggests that they lack rotational DOF and can only move linearly in three directions. Due to their lack rotational Degrees of Freedom they can only follow toolpaths that can be accessed from a fixed orientation along the whole path. Limiting their ability to print highly complex shapes.

The Articulated robots, shown in Figure 2.4b, are made up of a series of revolute joints that allow them to move in a variety of directions. These robots are well-known for their flexibility, and dexterity, which make them suitable for a variety of applications such as welding, painting, and assembling [7]. Researchers have recently begun investigating the use of Articulated robots in DED systems, where they can be combined with laser or plasma sources to deposit material onto a substrate [23]. In terms of movement, articulated robots are more adaptable than Cartesian robots, since they have several joints that position a tool in any 6 DOF pose.

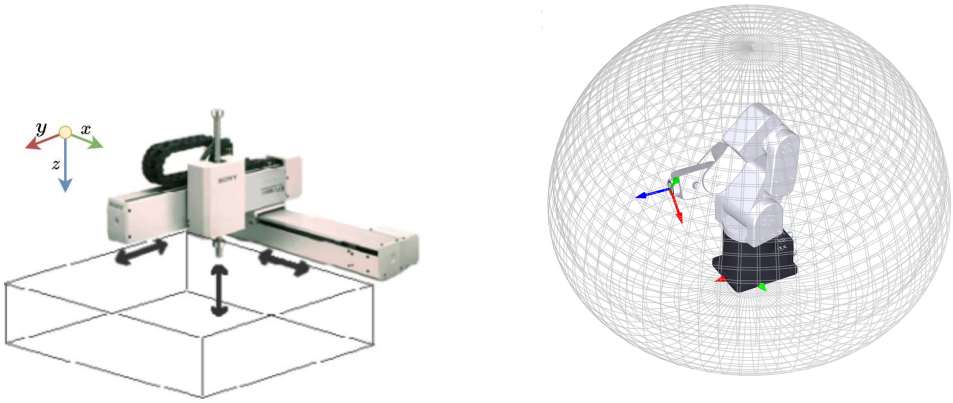

(a) 3 DOF Cartesian Robot (b) 6 DOF Articulated Robot

Figure 2.4: Workspace of a Cartesian and Articulated Robot. **Image Source:** [24] [25]

2.2.2 Articulated Robot Kinematics

The study of the motion of a robot mechanism in terms of positions is known as robotic kinematics. It relates the position and orientation of the robot manipulator's end-effector relative to the manipulator's base to the joint variables. A mathematical description of the robot's motion is provided by the kinematic analysis of robots, which is important since it is necessary for directing the robot's movement [7]. The robot's control system utilizes this mathematical description, and can also work out the path for the robot to take between two points. Robot kinematics primarily comprises two main problems: *forward* and *inverse kinematics*.

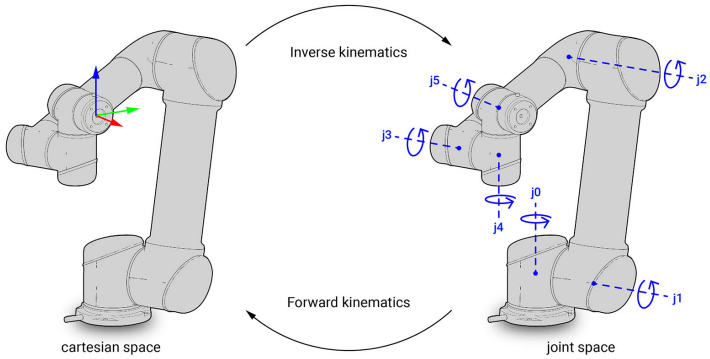

Figure 2.5: The relationship between Forward and Inverse Kinematics. **Image Source:** [26]

Forward Kinematics

The position and orientation of a robot's end-effector frame can be calculated using the joint coordinates thanks to the fundamental concept of forward kinematics. The ability to plan and carry out exact motions of the robot's end-effector in three dimensions makes this a crucial step in robotic control and manipulation. Calculating how to transform the robot's joint angles into the location and orientation of the end-effector in the task space is the challenge of forward kinematics [7]. Basic trigonometry can be used to accomplish this in simple robotic systems, but a more systematic method is needed for more sophisticated systems. This is where methods such as Denavit-Hartenberg (DH) [27] convention comes into play. By providing a systematic method for defining reference frames and calculating the resulting forward kinematics [28], the DH convention can simplify the process of determining the forward kinematics of complex robot manipulators.

Inverse Kinematics

Inverse kinematics is the problem of determining the joint angles required to generate a desired end-effector pose. In other words, inverse kinematics solves for the joint angles required to produce a desired position and orientation of the end-effector given a desired position and orientation in Cartesian space [7]. The inverse kinematics problem frequently presents greater complexity than the forward kinematics problem, as it could potentially yield multiple solutions or, in

some cases, no viable solution at all. The inverse kinematics can be mathematically characterized as the search for solutions that fulfill $T(\theta) = X$, where T is the forward kinematics function that translates joint angles to end-effector pose, X is the desired end-effector pose, and θ is the vector of joint angles [7]. The inverse kinematics can be solved analytically for most 6 DOF industrial robots, and as an iterative algorithm in the general case, such as Newton-Raphson [29], Jacobian transpose [30], or various weighted pseudoinverses [30].

2.3 Directed Energy Deposition with an Articulated Robot Manipulator

Directed Energy Deposition is a branch of AM, which uses a wide variety of metal as feedstock. The wire is fed to a substrate simultaneously as a laser beam is focused to create a melt pool while slowly depositing the material layer-wise. The recent advancement of AM technologies, has made metal manufacturing an interesting topic for research, and potential future for industrial applications for repairing and manufacturing of parts. A conventional 3D printer is limited to accessing only 3 linear DOF, resulting in lower resolution for the manufactured parts, ultimately affecting their quality. Using an articulated robot manipulator enables access to both linear and rotational DOF. This will enable a larger workspace to be utilized compared to other 3D metal printers, as illustrated in Figure 2.6. This highlights the large differences in terms of working space area relative to the robot's footprint between the two types of metal printing.

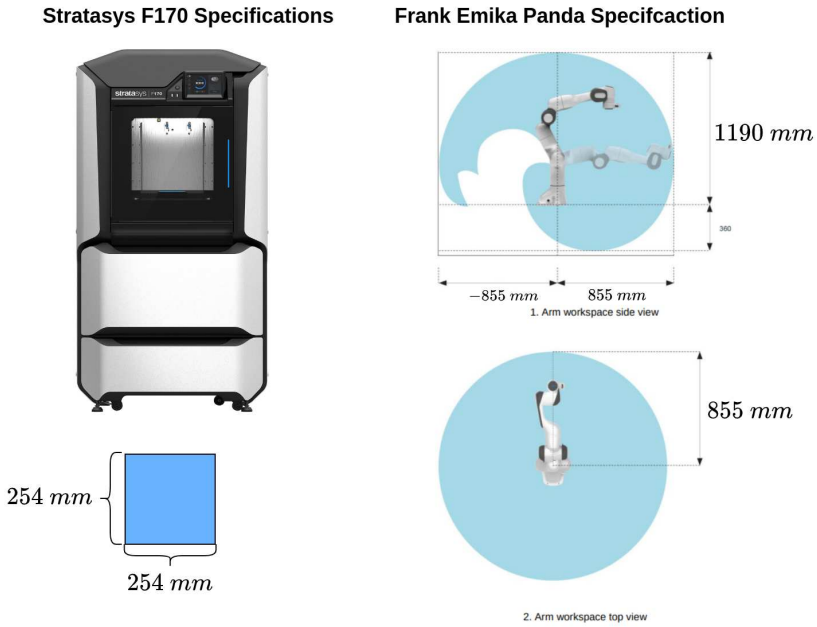

Figure 2.6: Comparison of a Stratasys F170 Cartesian robot manipulator working space and an articulated robot manipulator reachable space.

The DED system at SINTEF Manufacturing uses a MELTIO system and a KUKA Industrial Robot. The MELTIO system has the ability to process both wire and powder feedstock material. It is powered by 6 direct diode lasers with a total power of 1200 Watt and a wavelength of 976 nm, utilizes a wire feedstock of 0.8-1.2 mm in diameter, which is compatible with a wide range of welding wires and powder feedstock [31]. The KUKA Industrial robot has a 6 DOF articulated manipulator and a 2 DOF rotatable table, providing versatile movement capabilities. Figure 2.7 depicts the integrated MELTIO system on a KUKA Industrial robot at SINTEF Manufacturing.

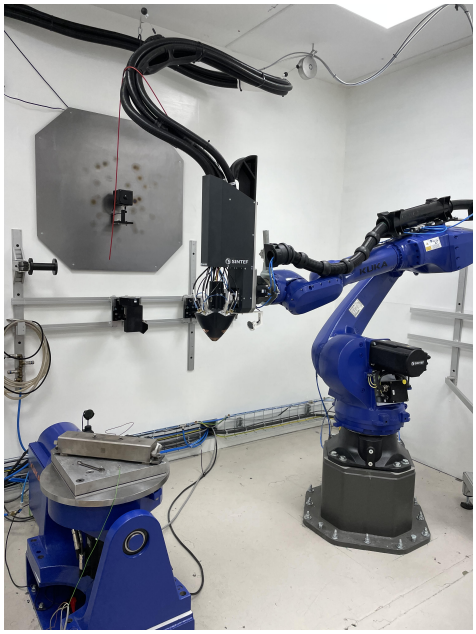

Figure 2.7: The MELTIO system integrated with a KUKA Industrial robot for DED processes at the SINTEF Manufacturing.

2.4 Computer Vision

The science of computer vision is developing quickly and has completely changed a variety of sectors. Most decisions on quality evaluation are made with the aid of the human visual sense. As a result of technological improvements, robots now use cameras as their "eyes," enabling automation and inspection control in a variety of industrial operations. Computer vision technology boasts a wide range of applications, including not only defect detection and motion tracking, but also encompassing sophisticated tasks such as 3D reconstruction of environments and point cloud processing for detailed spatial analysis. In this section, we will explore the fundamental principles of computer vision related to inspection.

2.4.1 Capturing and Representing Visual Data

The advancement of technology has made it possible to capture and represent visual data in various formats, encompassing images, videos, 3D models, and point clouds. The definition of the camera model and calibration, which allows us to

capture real-world data accurately, form the foundation of this capability. In this section, we will look at the fundamental concepts of camera models and calibration methods, as well as how they help us capture and represent visual data in a variety of ways.

Pinhole Camera Model

The pinhole camera model is the basic foundation and simplified camera model for projecting 3D points onto a 2D image plane. This model suggests that rays that are reflected from an object into a plane, which will create a 2D representation of the object, as seen in Figure 2.8. According to Sturm et al. [32], the Pinhole model is an effective way of capturing how humans perceive the world. Even from basic 2D images, it is possible to determine various attributes, such as the actual position of objects in the real world. This process is known as perspective projection and involves the conversion of 3D points within the world into a 2D plane. Additionally, this enables the establishment of a mathematical framework that simplifies the image capture process, enabling the representation of the relationship between world to 2D image coordinates. However, the representation of an object in 2D space is constrained since all points along a given ray are projected into the same point in the image plane. Due to the loss of depth information brought on by convergence of the multiple rays, the resulting 2D image might not be a genuine representation of the object's actual dimensions. As a result, while the pinhole model is helpful for many computer vision applications, more complicated camera models are often used to produce higher quality representations.

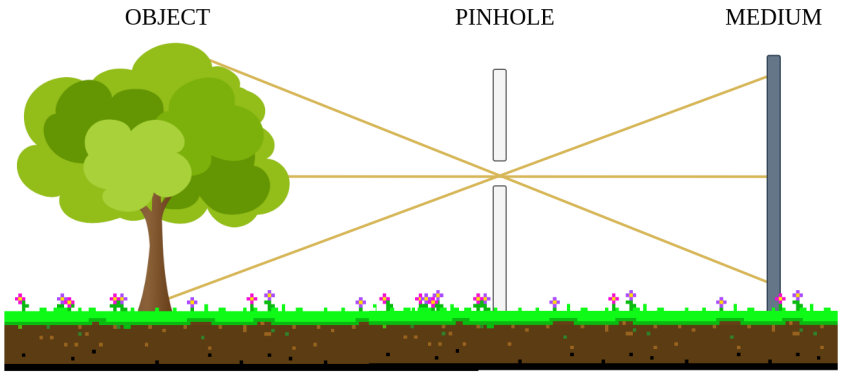

Figure 2.8: A simple illustration of a Pinhole Model.

Camera Model

The camera model plays a critical role in estimating the most precise projection matrix to describe the transformation from real-world coordinates to the image plane. This relation is established using the concept of the Pinhole model, which forms the basis for constructing the camera model. The camera model can be represented using the equation:

$$P = K * [R|t] = \begin{bmatrix} f_x & 0 & c_x \\ 0 & f_y & c_y \\ 0 & 0 & 1 \end{bmatrix} * \begin{bmatrix} R & | & t \end{bmatrix} \tag{2.1}$$

where (f_x, f_y) denote the focal length and (c_x, c_y) refer to the optical center. The term R represents a 3×3 rotation matrix, while t represents a 3×1 translation vector.

The camera model comprises two matrices, namely the extrinsic and intrinsic matrices. These matrices help to determine the accurate relationship between world coordinates and image coordinates. The intrinsic parameters (K) encompass the focal length and the optical center, which facilitate the transformation from camera coordinates to image coordinates. The extrinsic parameters include a rotation matrix R and a translation vector t, which are critical for transforming world coordinates to camera coordinates. However, the camera model's geometric precision is limited because cameras use lenses instead of a pinhole, and light passing through the lens is prone to distortion. Therefore, camera models may not provide a highly accurate representation of the real-world.

To obtain a more accurate correspondence between world coordinates and image coordinates, it is essential to perform a calibration procedure to determine the unknown parameters in the camera model. Typically, camera calibration involves estimating the intrinsic parameters for K and the distortion parameters of the lens, for converting camera coordinates into a 2D image plane. To achieve this correspondence, it is necessary to incorporate the extrinsic matrix (R and t) into the camera model. This inclusion facilitates the description of the world coordinate frame reference into the camera coordinates, resulting in a more precise

and reliable representation, the effect of these matrices is illustrated in Figure 2.9. To calculate these unknown parameters effectively, a camera calibration method is required.

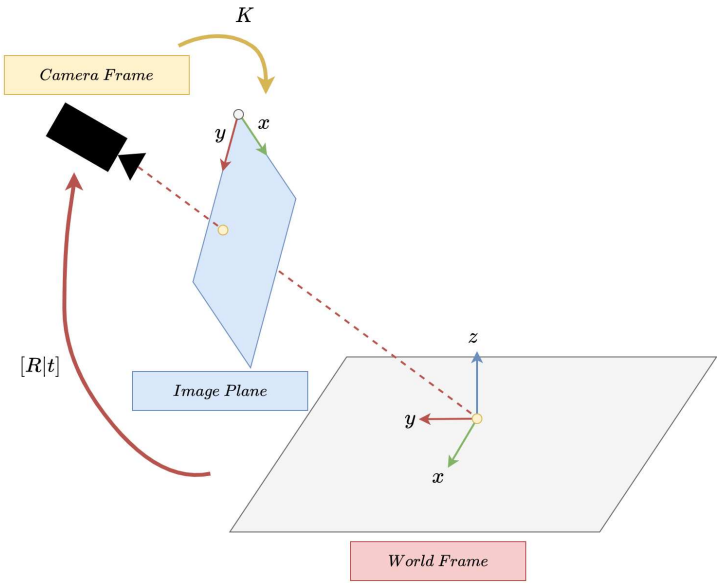

Figure 2.9: A Camera Model's Extrinsic and Intrinsic Conversion from world frame to image plane.

Distortion in Cameras

The process of capturing an image with a camera involves light passing through a lens and being projected onto a sensor. However, due to imperfections in the lens and variations in the alignment between the sensor and the lens, distortions can arise that impact the quality of the resulting image. Typically, two types of distortion are observed: *radial* and *tangential distortion*.

Radial distortion occurs when the lens bends light unevenly, resulting in the displacement of light rays away from their original positions, as seen in Figure 2.10. Light that enters the lens at the edges will bend more than light entering through the optical center, leading to a characteristic pattern of image distortion that can be corrected with algorithms such as Brown's Distortion Model [33] and Division Model [34].

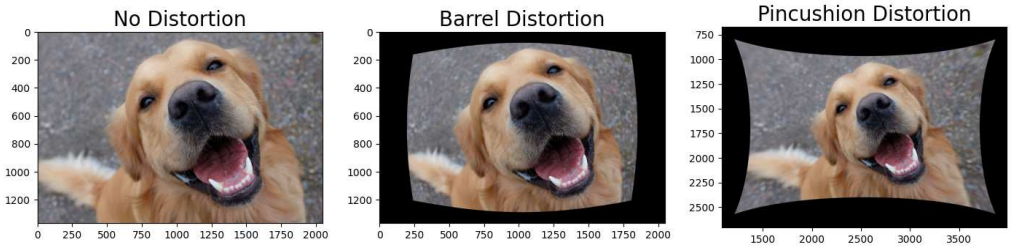

Figure 2.10: The effect of Radial Distortion.

Tangential distortion, arises from misalignment between the camera sensor and the lens. This can result in a stretching or slanting of the image, as seen in Figure 2.11, which can likewise be corrected with a suitable calibration method. It should be highlighted that these distortions might differ between different types of cameras and lenses, requiring distortion calibration for each individual camera. The problem can also be corrected by shifting the image parallel to the image plane, this can be solved also by using an algorithm such as Brown's Distortion Model [33].

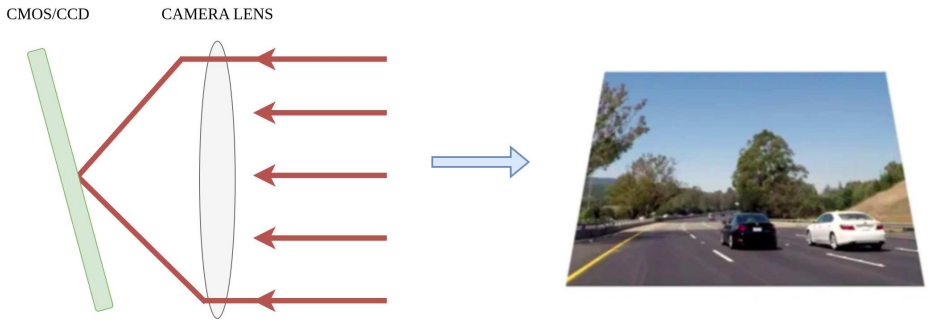

Figure 2.11: The effect of Tangential Distortion.

2.4.2 Camera Calibration

Camera calibration plays a fundamental role in the field of computer vision, and mostly adopts the mathematical model of pinhole model. In essence, calibration involves the estimation of unknown parameters that relate to the camera model. This includes determining a camera's intrinsic parameters, such as focal length, optical center, and lens distortion characteristics. Calibration techniques typically involve capturing images of a known calibration object from multiple viewpoints, and

using these images to solve for the unknown parameters that define the camera's optical properties [35]. To obtain accurate estimation from world to camera frame, a well-defined object of known dimensions is utilized in the scene. Capturing the object from various orientations and positions enables the approximation of the intrinsic and extrinsic parameters. The object size enables us to solve extrinsic parameters for rotation and translation to establish a mapping between image and world coordinates, which is essential for obtaining an accurate estimate of the camera's parameters. A mathematical model is employed to solve a system of equations using a set of images captured from different viewpoints and orientations.

There are a number of camera calibration methods available, and the method selected is determined by the information available about the 3D scene. Some use multiple views of a 3D pattern with a known structure positioned and oriented randomly in space. Other methods require a unique, calibrated 3D setup in which the positions of every 3D point and the camera center are known. While there is currently no definitive state-of-the-art calibration method, Zhang's [36] calibration is the most widely used calibration method. It is a well-known approach for camera calibration that employs the checkerboard pattern to derive the homography transformation to the image plane. For additional in-depth comparisons of various calibrating methods, Remondino et al. [35] conducted a comprehensive analysis of various camera calibration methods, evaluating their advantages and limitations.

Hand-Eye Calibration

Hand-eye calibration is one of the known methods to determine the relative transformation between an end-effector and the camera frame [37]. Initially, camera calibration is undertaken to ascertain the camera's internal and external parameters, a critical step for accurate vision representation [36]. This is followed by robotic calibration, which is aimed at pinpointing an accurate stance for the mechanical gripper [38]. Furthermore, a hand-eye calibration is used to identify the camera's and end-effector homogenous transformation matrix, and at last the relative inaccuracy is used to evaluate the results of hand-eye calibration. In order to identify a transformation from the camera coordinate system to the robot coordinate system, it is common to classify hand-eye calibration into two categories: *eye-to-hand* and *eye-to-robot calibration.* A mounted camera is used in the second technique,

called eye-in-hand calibration, which seeks to identify a transformation from the end-effector to the camera coordinates. Both methods are shown in Figure 2.12, demonstrating how the robot's movements can be guided based on the visual data from the camera.

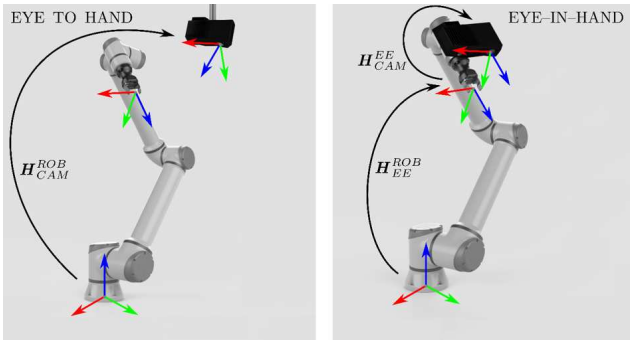

Figure 2.12: An example of Eye-to-Hand and Eye-in-Hand calibration. **Image Source:** [39]

ArUco Markers

ArUco markers are often used for camera pose estimation, which involves determining the position and orientation of a camera relative to a known reference point or object [40]. These markers are predefined two-dimensional black and white square patterns that can be visually identified and tracked, as seen in Figure 2.13. These markers provide a convenient and efficient way to identify camera position relative to these known markers. ArUco markers are appropriate for real-time applications since they are made to be simple to detect and have a low computational cost. They function by locating the corners of a square marker and using that knowledge to determine the marker's attitude relative to the camera position. In contrast, Zhang's approach necessitates the use of singular value decomposition to solve a linear equation, which can be computationally expensive [36].

Figure 2.13: Examples of ArUco marker with IDs 0,1,2,3. **Image Source:** [41]

2.5 Point Clouds Registration

Point cloud registration is a fundamental problem in robotics and computer vision that aims to align multiple point clouds by finding the best rotation and translation transformation. Several algorithms have been developed to address this issue, using different techniques to determine the ideal registration. In most cases, known correspondences are used to estimate a more ideal registration. However, in real-world scenarios, these correspondences may be unknown or contain a significant number of outliers. There are a lot of different point cloud registration algorithms, but this thesis will mainly focus on Iterative Closest Point (ICP) and Random Sample Consensus (RANSAC). These algorithms are frequently used nowadays, but operates under different assumptions. The ICP algorithm is a well known approach for aligning two point clouds, but requires both a good initial transformation and no presence of outliers. In contrast, the RANSAC algorithm works well with the presence of outliers, but requires the data to be described by fitting a mathematical model.

2.5.1 Iterative Closest Point

The Iterative Closest Point algorithm is a registration method that finds the transformation between two point clouds for a variety of data types. The algorithm determines the rotation and translation necessary to align the two point clouds, with the first step being to calculate the nearest point to a given point. The initial paper for ICP by Besl et al. [42] solved finding the transformation by computing the Euclidean distance between a point and a point set in order to determine the closest distance, but this process is computationally complex and can be slow. After determining the closest points between two point clouds, a rigid transformation will be used to align the source point cloud with the reference point cloud. The Mean Squared Error (MSE) is then computed to measure the discrepancy between the transformed source point cloud and the reference. If the MSE falls below a predefined convergence threshold, the registration process is terminated. The pseudocode for the ICP registration process is summarized in Algorithm 1 with an overall time complexity of $O(n^3)$.

Algorithm 1 Iterative Closest Point Algorithm [42]

Require: Point cloud $P = \{p_1, \ldots, p_n\}$, Target point cloud $X = \{x_1, \ldots, x_n\}$, Convergence threshold τ
Ensure: Optimal rigid transformation T

$T \leftarrow$ initial transformation
while not converged **do**
  $Y \leftarrow$ for each point in p in P get the closest point in X
  Compute the rigid transformation T that minimize the Mean Squared Error between the points in P and the closest point in Y
  Apply the transformation T to P
  Get MSE of current iteration $MSE_{\text{curr}} \leftarrow : \frac{1}{n} \sum_{i=1}^{n} |y_i - p_i|^2$
  Compute change in between in $\Delta MSE \leftarrow MSE_{\text{curr}} - MSE_{\text{prev}}$
  Set $MSE_{\text{prev}} \leftarrow MSE_{\text{curr}}$
  if $\Delta MSE < \tau$ **then**
    break
  end if
end while
return T

An example of the alignment process can be seen in Figure 2.14, which demonstrates the application of ICP for aligning two line sets. It should be highlighted, nonetheless, that the reliability of the findings significantly depends on a good initial estimation of the relation between the two sets. In most situations, the ICP algorithm is prone to converge to local minima. Outliers are practically always present in real-world situations, which can have a substantial impact on how well the algorithm finds correspondences and the overall runtime of the algorithm.

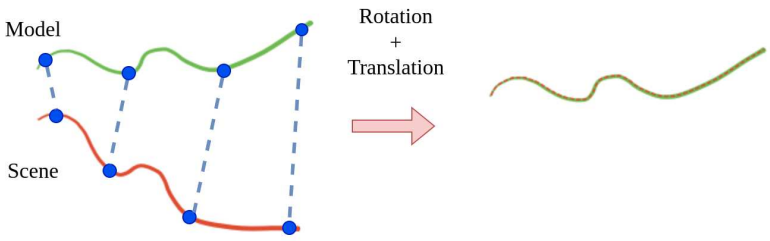

Figure 2.14: Simple example of ICP algorithm of two line sets.

2.5.2 Random Sample Consensus

The Random Sample Consensus algorithm was introduced by Fischler et al. [43], which is a parameter estimation approach for handling data with a high proportion of outliers. The algorithm utilizes a resampling method by expressing models with parameters that are defined as geometric shapes [44]. Additionally, the algorithm demonstrates proficiency in discerning distinct shapes present in extensive point clouds, such as the detection of planar structures. The procedure begins by picking the smallest number of random points needed for the model to compute the model parameters using only the selected data to estimate a fit for the model. After constructing this model, distances will be computed, and any measurement less than a certain threshold will be marked as an inlier. The more iterations the algorithm runs, the more likely it is to develop a model that fits the data better and eliminates outliers. The RANSAC algorithm has several variations and can be applied in a variety of ways, such as fitting a model to a single point cloud or aligning two point clouds based on the given mode. The RANSAC algorithm presented in this thesis of is designed specifically for detecting planar surfaces within a point cloud, as illustrated in the pseudocode presented in Algorithm 2.

Algorithm 2 Random Sample Consensus Algorithm for Fitting Plane [43]

Require: Point cloud $P = \{p_1, \ldots, p_n\}$, Convergence threshold ϵ , Maximum iterations N
Ensure: Optimal rigid transformation T

```
bestInliers ← 0
T ← Identity transformation
numberRandomPoints ← Number of points needed by the model (e.g 3 for plane)
for i = 1 to N do
    randomPoints ← Select numberRandomPoints points randomly from the P.
    bestModel ← Fit the model to selected points at randomPoints
    numberOfInliers ← 0
    for each point in P do
        distance ← Calculate distance from point to plane using bestModel
        if distance ≤ ε then
            numberOfInliers ← numberOfInliers + 1
        end if
    end for
    if numberOfInliers > bestInliers then
        bestInliers ← numberOfInliers
        T ← bestModel
    end if
end for
return T, bestInliers
```

The time complexity of the RANSAC varies depending on the desired model to be fitted. In 3D space, planes serve as relatively simple geometric models that can be utilized for efficiently computing distances. A plane model can be fitted by solving for the parameters a, b, c, and d using three random non-collinear points, as seen in Figure 2.15. The overall time complexity would be $O(Nk^2)$, where $O(k^2)$ comes from computing the distance from a point to the plane required for solving a set of linear equations.

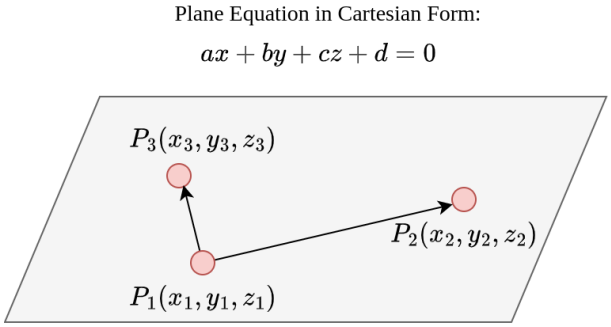

Figure 2.15: Illustration of the process of random plane sampling in the RANSAC algorithm based on fitting a plane model.

2.6 3D Reconstruction using Laser Scanner

3D reconstruction, creates digital models of real-world objects. A variety of techniques exist for this purpose. In this thesis, methods which involve projecting a laser line onto an object and capturing the reflected light using a camera are investigated, as seen in Figure 2.16. These types of scanners offer a high resolution and accuracy, but can be limited by optical material properties. The scanner operates by detecting the diffused reflection, and when specifically interacting with metals, one can anticipate a higher degree of specular reflection which will result more outliers to be produced. To mitigate some of the potential challenges this may introduce, laser line scanners employ a bandpass filter. However, this also makes it difficult to extract points from bright and dark surfaces. In contrast to conventional structured light methods, which use a projector to cast predetermined patterns of light onto a scene, the geometry of the scene distorts these patterns, and a camera then records and processes these distortions to create a single point cloud that represents the 3D reconstruction of the entire scene. Normally, these traditional methods are more expensive and provide less dimensional accuracy in comparison to a simple laser line scanner. These laser line scanners works by capturing a single line in 2D space, where the z value denotes height and the extent of the laser line along the x axis represents length. As a result, multiple captures are required to create a full 3D reconstruction by combining these profiles.

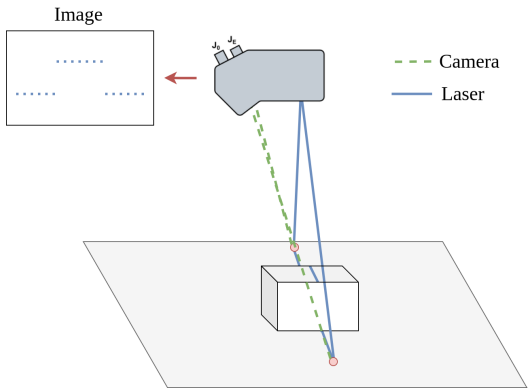

Figure 2.16: Illustration of a Laser Line Scanner's output.

When it comes to materials like metal, which have a higher degree of specular reflection than other materials, there is a larger possibility of generating more outliers. The effect of specular light introduces additional challenges to ensuring the accuracy and reliability of the scanner's output, with the issue being associated by both the shape and metal type. Wang et al. [45] addressed the problem of outliers resulting from specular reflection on edges and smooth surfaces in laser line scanning. They proposed a path optimization approach to mitigate this issue, aiming to identify a more ideal scanning path, as illustrated in Figure 2.17.

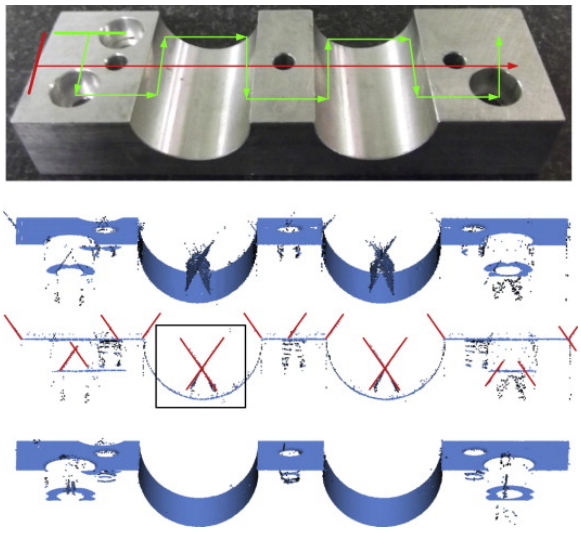

Figure 2.17: A scanning of aluminium using a laser line scanner with two different paths. **Top:** Shows two scanning paths. **Upper-middle:** generated outliers following the red path. **Lower-middle:** the path of specular reflection generating the outliers. **Bottom:** Following the green scanning path. **Image Source:** [45]

To fully comprehend how these outliers are generated by specular reflection, it is important to recognize that a substantial portion of light hitting a surface with continuously varying surface normals gets reflected as specular light [45]. The angle of the specular reflection will regularly change on a surface with shifting normals, which can cause a higher degree of specular light with varying shapes of the geoemetry. Given that the laser line can be represented as a Gaussian distribution, and normally the center of the profile is detected as diffuse reflection. However, specular reflection is influenced by the angle of the surface normal, which certain geometric features, such as edges, may exhibit a higher rate of generating outliers, as shown in Figure 2.18.

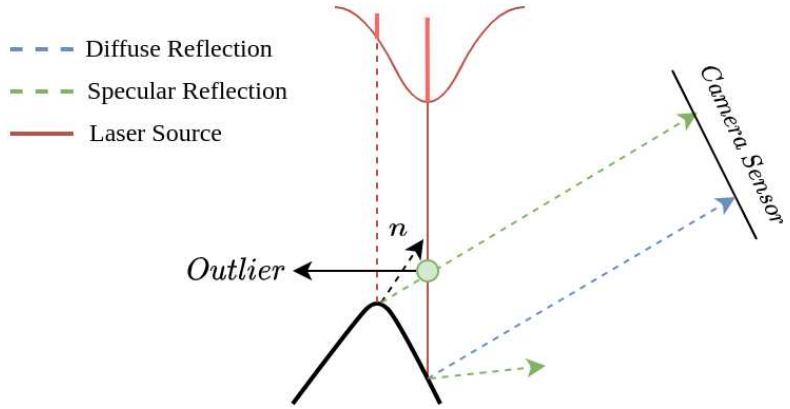

Figure 2.18: Illustration of specular reflection generating outlier from an edge.

2.7 Related Work

The section will concentrate on automatic inspection for various AM systems. While outlining the major obstacles that might come up in our framework, we will correlate our study with recent examples from literature. Studies on vision-based methods in DED processes differ from the objectives and setup for our framework. Therefore, the search will focus on finding comparable alternatives to AM processes that utilize vision-based setups. The section's conclusion will provide a list of some of the key challenges encountered in building the framework's foundation.

2.7.1 Error Detection for Cartesian 3D Printer

Charalampous et al. [46], introduced a real-time vision-based error detection, proposed for a conventional Cartesian 3D printer. The objective of this research was to develop an error detection system in AM processes. Figure 2.19 illustrates the pipeline, beginning with the pre-processing of the manufactured object's G-code generated from a CAD model, to create an equivalent 3D point cloud of the different layers which will serve as the reference model. Portions of reference point cloud will be occasionally be compared with reconstructed point cloud. This comparison is done by using ICP algorithm for alignment and KD Tree [47] for computing the closest distances between the two. Lastly, the 3d printer will stop dependent on a specific threshold based on computing both Mean Absolute Error (MAE) and Root Mean Square Error (RMSE). The printing is automatically stopped, preventing further production of defective components.

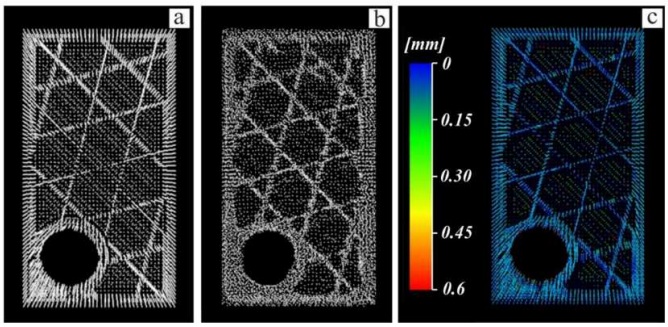

Figure 2.19: Illustration of the point cloud registration between two point clouds. **Left:** Theoretical point cloud. **Center:** 3D Reconstructed point cloud. **Right:** Comparison after ICP algorithm. **Image Source:** [46]

This system highlights both real-time monitoring and error detection in a conventional 3D printer. However, it is not tested with a wider range of AM methods such as DED processes. Since the pipeline makes use of a point cloud generated by a 3D printer simulation, which may result in an inaccurate representation of the printed object. Another issue is the reliance on the ICP algorithm for alignment between the two point clouds. This approach, however, is strongly reliant on a good initial alignment. If the initial alignment is not set correctly, the method may fall into a local minimum, causing the ICP algorithm to potentially fail to converge to the optimal alignment. While the KD Tree is a popular choice for

nearest neighbour searches, it does have some disadvantages. Also, when dealing with huge datasets, it also may struggle with scalability, making the tree-building process computationally expensive and demands a significant amount of memory for larger point clouds. Some of these issues highlight the challenges that can occur from relying too much on multiple point cloud registration algorithms for automatic inspection.

2.7.2 Height Correction through Layer Addition or Removal

DED process has a minor instability with requiring accurate representation of a geometrical object from its design, in comparison to simpler conventional alternative AM processes. Garmendia et al. [48] created a framework that makes use of structured light utilizing a projector at a fixed position to achieve in-process height modification in a laser-based DED process. By placing the scanner at a fixed position, they could capture a point cloud of the height and measure the height relative to the build platform. A pre-set of layers was built before employing a control mechanism that dynamically adds or removes layers according to the build height information from the intended CAD model of the object being manufactured. The height error is the difference between the theoretical layer height produced by the path generator and the measured layer height. Depending on the calculated error, layers are either added or removed, as seen in Figure 2.20.

This framework utilizes a similar setup and method as Garmendia et al. [48]. However, this framework provides an advanced solution for in-process layer height correction, since it alter the design of the geometry. Furthermore, the scope of the experiment was restricted, as it was carried out using a single metal variant. It is also noteworthy to mention that the constraints of this study, specifically the application of structured light, were limited due to the exclusive use of one type of metal.

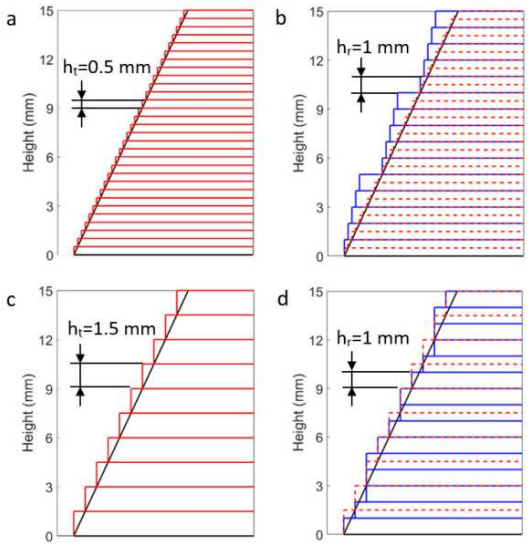

Figure 2.20: The figure displays a comparison of the theoretical height (h_t) represented by **a** and **c**, and the expected layer height (h_r) represented by **b** and **d**, with layer corrections indicated every five layers in the first row and every three layers in the second row. **Image Source:** [48]

2.7.3 Error Correction based on Working Distance

Several process parameters can be adjusted based on the measured height deviation to account for differences. Although adjusting the number of layers by adding or removing them might appear as an efficient way to achieve the desired height of the object. However, this approach can unexpectedly alter the geometric design and produce other geometric deviation, such as sudden overhangs. In contrast, Zhou et al. [49] proposed a framework for in-process clad height control in a DED processes using optical height monitoring to adjust working distance between nozzle and the manufactured object. The conventional methods for regulating the nozzle working distance in a DED process, such as passive controls using convergent nozzles or active measures utilizing dynamic changes to the tool path, laser power, powder flow rate, or feedrate, have inherent drawbacks. The suggested method was presented as having various advantages over previous frameworks, including a simpler design that requires fewer sensors and real-time operation. A heatmap is produced from the camera to monitor the melt pool and estimate the position of the highest pixel in the melt pool, and a known location inside the nozzle is used as a reference to measure the distance between them. The new

working distance is then calculated from the height based on the thermal camera's measurements to ensure the height of the layer matches the height of the tool path. The final results of the height controller can be seen in Figure 2.21.

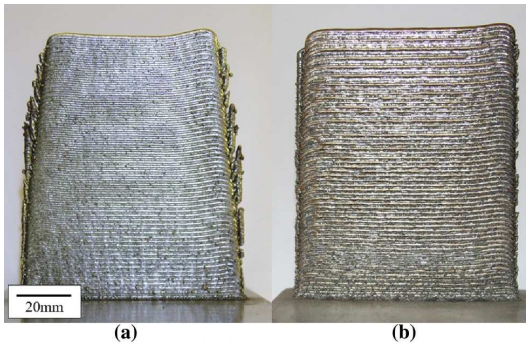

Figure 2.21: Illustration of the results without and with the height controller. **(a)** without controller and **(b)** with controller. **Image Source:** [49]

The findings demonstrated that the height control system was efficient in maintaining the target height while also assuring geometric part accuracy. The updated height is used to adjust the nozzle to the new optimal working distance. This highlights a bigger improvement for adjusting process parameters to improve the geometry. However, the scanning procedure does not allow a thorough inspection of the entire production process, or offer any exhaustive inspection of the height discrepancies.

2.7.4 Conclusion on Related Work

The majority of related studies employ specifically tailored systems to implement error detection and correction methods, demonstrating a strong need for continued research in this area to improve inspection capabilities within AM processes. Extensive research has been dedicated to devising control strategies aimed at enhancing production quality in DED processes. However, the objectives of the framework outlined in this thesis will venture further. It aims to explore the production process to assist in finding a more suitable process parameters for a variety of metal types, but also to explore whether height deviation data based on the insights from these related studies can potentially be used to refine the process parameters in the DED system at SINTEF Manufacturing.

Furthermore, while many existing systems leverage structured light which utilizes a projector, the potential of alternative scanning technologies remains underexplored. Certain studies have explored the application of laser line scanners, recognized for their high dimensional accuracy. However, these systems do not incorporate any method for 3D reconstruction due to limitation of integrating such methods and technologies into their existing systems. Therefore, this thesis seeks to examine alternative technologies in conjunction with the utilization of an Articulated robot manipulator's multiple DOFs. By leveraging the robot's mobility, the objective is to augment the scanning procedure and provide an opportunity for a more in-depth analysis through 3D reconstruction. This research could potentially widen the application across a wider variety of metal types, extending the possibilities for automatic inspection in DED processes.

Chapter 3

Method

This chapter describes the thought process involved in the selection of deviation properties to inspect and hardware used. It will progressively detail the creation and explanation of each element within a vision-based framework, which is designed for the experiments referred to in Chapter 4. We will begin by examining the deviation types we aim to inspect, and then delve into the specifics of the hardware employed and demonstrate how we to incorporate and optimize it for 3D reconstruction with the DED system outlined in Section 2.3. We will then discuss the steps involved in processing and measuring point clouds to compute the deviation, as well as explore potential future applications of the data to improve the DED process. Furthermore, we will discuss the steps involved in processing and measuring point clouds to compute the deviation.

3.1 Overview of Prior Studies

Prior to this thesis, research was conducted to develop a method for a vision-based framework in the specialization project [6]. A summary of previous research on the subject will be provided before delving into the current framework for this thesis. To identify the most appropriate approach, a thorough analysis was conducted, involving the examination, implementation, and rigorous testing of

several alternatives. This section presents a concise review of significant past investigations and methodologies considered during the specialization project, ultimately leading to the selection of the current preferred framework.

3.1.1 Exploration of Previous Framework

The initial study on a vision-based framework, as shown in Figure 3.1, employed a method attempting at utilizing the rotating table with VC Nano 3D-Z at a fixed-position. Although this specific approach was not directly employed in the DED system, a simplified setup was replicated, as seen in Appendix D. By calculating the distance to the rotation table, the scanned profiles could be merged through computing a rotation transformation. However, this method was not ideal, as it relied on the scanner's position relative to the table and also required the rotational speed of the table, which proved difficult to calibrate and control.

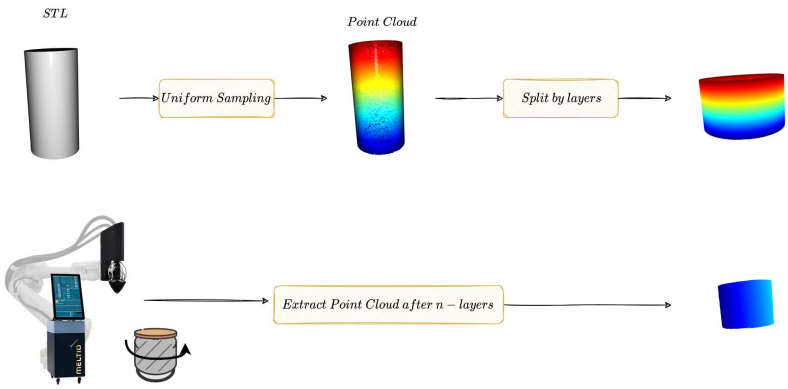

(a) Pre-processing for 3D reconstruction and STL.

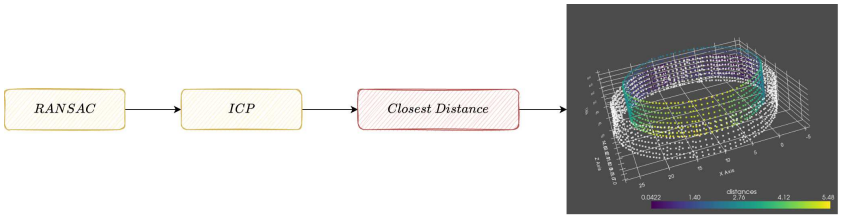

(b) Alignment using Point Cloud registration algorithms (RANSAC and ICP) with error computed as the closest distance using KD Tree.

Figure 3.1: Visual representation of the methodology employed in the specialization project: Key stages include 3D reconstruction, preprocessing and point cloud registration algorithms for alignment. **Image Source:** [6]

The prior objective of the framework was to examine the total geometric deviance, necessitating a dense point cloud to capture the complete object for inspection. This approach was found to be time-consuming and required numerous scanning positions to capture the majority of the object. The scanning process had to be further adapted based on the manufactured object's shape to retrieve a dense point cloud. Furthermore, to enable efficient comparison between 3D reconstructions and STL models, a computationally efficient approach was adopted. Instead of directly comparing a mesh to a point cloud, which can be highly computationally intensive. To address this issue, a selective sampling method was applied to the STL model. By only comparing the distances between the closest points, this approach significantly reduces computing expense. It systematically selected the data points from the STL model at random intervals, thus ensuring comprehensive coverage while limiting the number of points. To accurately compute the closest distances for alignment and deviation analysis, both RANSAC and ICP algorithms were utilized. These algorithms were employed to align the data and calculate the closest distance utilizing KD Tree [47] to optimize the computation. This approach closely aligns with the methods outlined in Subsection 2.7.1. Comparing the sampled STL model and the entire scan accurately is challenging due to the variations in sampling methods employed by different algorithms. As shown in Figure 3.2, the visual differences between the distributed points and the laser scan are apparent. The presence of vertical lines in the laser scan results requires a more suitable sampling algorithm adapted to the number of profile scans. As a result, using the closest distances as a deviation metric becomes unsuitable for evaluating the comparison between an STL model and a 3D reconstruction.

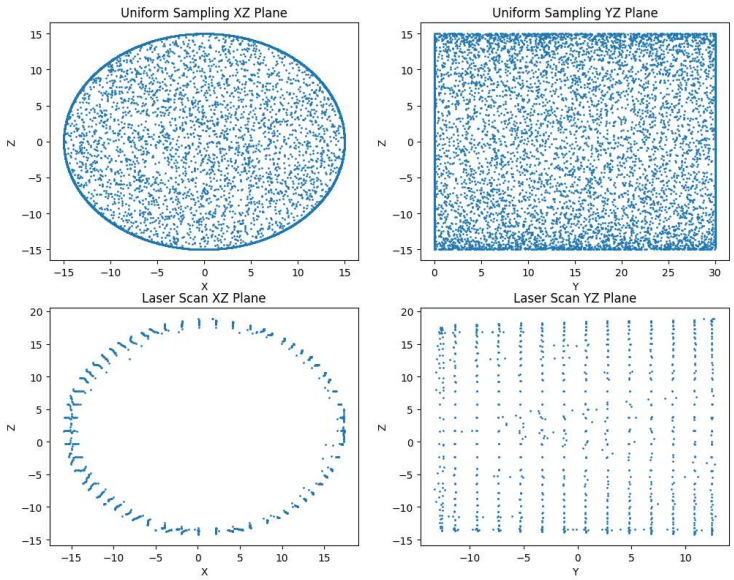

Figure 3.2: Comparison of Profile Scans with the VC Nano 3D-Z and a rotation table, and Uniform Sampling Distribution. **Top:** this row demonstrates the uniform sampling method, applied to uniformly sample a STL model. **Bottom:** this row visually represents the profile scanning process, in which each sample is rotated incrementally.

3.1.2 Insights and Key Findings

The overall study exposed the weaknesses and limitations of the previously attempted methods. Based upon these insights, this thesis aims to leverage the findings from the prior study to develop a better vision-based framework. The objective is to minimize the dependency on the scanner's position, decrease computational expenses, and enhance reliability by reducing the need for point cloud registration algorithms such as ICP and RANSAC. Firstly, this thesis will investigate alternative methods for 3D reconstruction that can work with complex shapes utilizing the KUKA Industrial robot multiple DOFs. Furthermore, examining the overall geometric deviation posed significant challenges, and the focus should be pivoted towards inspecting the height deviation similar to the frameworks outlined in Section 2.7.2 and Section 2.7.3. Furthermore, the inspection of height deviation, as highlighted in earlier studies and discussed in Section 2.7, can be effectively utilized within a feedback loop.

3.2 Selecting Deviation Properties to Inspect

The manufacturing process in a DED system is a complex and intricate system that involves numerous steps, each of which can introduce various sources of geometrical deviations. These deviations can arise from a wide range of factors, such as machine tool errors, tool wear, material deformation, and environmental influences. While identifying every instance of deviation may be challenging, the focus has been placed towards inspecting the changes of geometric deviations related to height. Maintaining a constant width and length throughout the process can be challenging, as it depends on the trajectory planning. On the other hand, the layer height is typically kept constant, it yet remains challenging to ensure consistency throughout the process. This is due to various factors such as the deposition rate, melting point, and the speed of the robot arm.

3.3 Choosing the Hardware

The initial study started with exploring two hardware types, Zivid Two and VC Nano 3D-Z, both seen in Figure 3.3, as methods for producing dense point cloud for 3D reconstruction. Both hardware solutions used different methods to generate these point clouds, each with their own advantages and drawbacks. The Zivid Two employs structured light to create a depth map using binary patterns projected onto the object. The Zivid Two is sensitive to ambient light conditions, which may cause interference and affect the accuracy of the generated point cloud. On the other hand, the VC-Nano 3D-Z uses laser triangulation to estimate a profile of points with high precision. It is not affected by ambient light and has a higher precision. The VC Nano 3D-Z was chosen as the preferred hardware solution for this thesis after extensive consideration and testing with both types of hardware during the specialization project. The VC Nano 3D-Z's high dimensional accuracy and minimal susceptibility to ambient light conditions were some of the factors in the selection.

Figure 3.3: **Left:** Zivid Two. **Right:** VC-Nano 3D-Z

3.4 VC Nano 3D-Z

The VC Nano 3D-Z is a compact and highly precise hardware solution that uses laser line triangulation to estimate the profile of points. The scanner utilizes a methodology to capture and compute depth and height dimension of objects in two dimensions. Unlike other traditional laser scanner that capture the whole point cloud in a single capture, the VC Nano 3D-Z uses a blue line laser that scans the object at frequencies of up to 400 Hz, allowing real-time capture of objects with high accuracy. The dimensional accuracy of the VC Nano 3D-Z model large 6/26, that is defined as: the resolution ranges from 140 μm to 600 μm in the X direction, and from 20 μm to 380 μm in the Z direction [50]. This represents the minimum and maximum respective measurements the model can accurately discern within these two dimensions. Additional insights into this scanning technique can be found in Section 2.6.

The VC Nano 3D-Z runs on Linux with all the image processing algorithms built in. It uses a client-server architecture, with the conventional TCP/IP protocol over Ethernet are used to control the scanner. This enables the scanner to function as a server, responding to transmission from client requests, and also support the speed up to 1 Gbit, and lower speeds of 100 Mbit, and 10 Mbit [50]. Furthermore, the scanner can receive output via an Ethernet connection, providing real-time communication speed.

3.4.1 Pipeline for Creating VC Nano 3D-Z Profiles

To ensure accurate and precise reconstruction of the object, a calibration routine is required. This is achieved using Zhang's [36] method of planar checkerboard surfaces, which allows for the retrieval of the camera's intrinsic and extrinsic matrices, as described in Section 2.4.2. These matrices are used to calculate the reconstruction of the object and ensure high accuracy and precision. The VC Nano 3D-Z hardware uses a blue line laser to capture depth and height information in two dimensions. Most of the work of capturing the information is done through the hardware and software in the VC Nano 3D-Z.

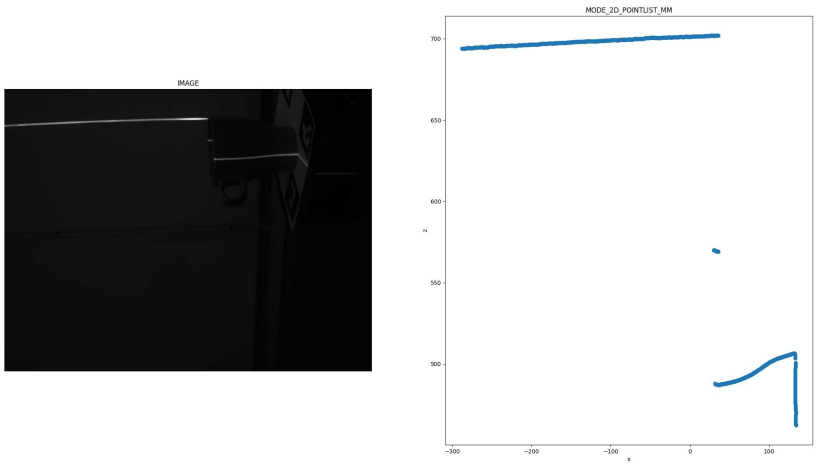

Figure 3.4: An illustration of the output of the scanner. **Left:** intersection of an object and a laser line. **Right:** x-axis denotes height, and y-axis represents distance from the laser. **Image Source:** [6]

Despite the complexity of a laser line scanner, its fundamentals can be understood by studying a simple setup including a regular camera and a laser line. Firstly, the laser line exposure region contrasts sharply with the background, making it simpler to retrieve. Processing the laser line first yields a gray image, which can then be binarized by either using simple thresholding to decide whether a pixel should be 1 or 0, or by using a method like Otsu's Binarization [51] to find the best threshold. This process yields the points in two dimensions from the laser intersection, and Figure 3.4 demonstrates the resulting output. The laser's reflecting properties cause the light from a surface region where a laser line is

emitted to spread out across a wider surface area. To correct for this, the second stage is to reduce the foreground portions of a binary image using skeletonization. White pixels covering bigger regions will be reduced to narrow 1 pixel lines. This process helps to eliminate any irregularities in the laser line that may be caused by variations in the surface or angle of the object being scanned. The final step calculates the profile of the scan in camera coordinates relative to the laser line, using laser triangulation to estimate the depth of each point of the profile.

3.5 Exploring Impact of Metal types and Geometry on Reflectivity

Reflectivity is an important property which is influenced by the material properties but also the geometric shape of the object being scanned. To further understand the challenges posed by reflective surfaces in a variety of metal types, it is essential to find the appropriate parameters for the scanner when performing a 3D reconstruction. Metal types have varying degrees of reflectivity, which can significantly impact the quality of profile scans. For instance, aluminium is known to have high reflectivity, which can pose significant challenges when attempting to obtain accurate scans of aluminium manufactured objects, thus requiring lower shutter time. In contrast, metals such as carbon steel are less reflective, making them more suitable for scanning, thus a higher shutter time yields better results.

To map out these configurations in the experiment, a subset of four plates have been chosen consisting of manufactured objects of different materials across each plate to be scanned to measure the influence of both geometric variations and metal type on the quality of the scan. Each plate is based on two metals with different reflections, which can fluctuate the diffuse and specular light significantly due to variations in metal composition, surface roughness, and other factors. The following parameters selected for the experiment are outlined in Table 3.1. These parameters have been selected due to their significant impact and correlation on the quality of the scan. It is important to note that there are other parameters that could be considered in this experiment, however, for the purposes of this study, the focus will be exclusively on these parameters. In order to effectively assess the

impact of each parameter, a controlled study was performed, where each parameter was varied while keeping the others constant. The results of this experiment are given in Section 4.2.

Table 3.1: Experimental Configurations of VC Nano 3D-Z

Configuration	**Description**
Shutter Time [μs]	The duration of the camera's exposure to capture the image of the laser line.
RLC Threshold	The threshold value set for the RLC algorithm to detect the laser line.
Exposure Mode	The camera's exposure configuration, which includes three options: • **AUTO EXPOSURE**: uses a fixed shutter time, • **FIXED EXPOSURE**: Trying to find an estimate of an optimal shutter time, and • **DOUBLE EXPOSURE**: Uses two extra shutter times.

3.5.1 Optimization based on Error Metrics

To optimize the laser line scanner configuration, a set of error metrics that will be used to evaluate the quality of the generated laser line profile must first be determined. These error metrics are essential in determining the accuracy and reliability of the laser scanner, and can ultimately help improve the quality of the resulting data. Each of these error metrics will provide valuable insights into the accuracy of single line scans taken from various metal plates, allowing for a comprehensive evaluation of the results. The results will be compared across different parameter configurations to identify the configuration that produces the best results for each metal. Each parameter configuration is evaluated based on the following metrics: *average distance*, *standard deviation of distance*, and *maximum Z distance from mean*.

The Average Distance, denoted as E_{avg}, represents the mean Euclidean distance computed over consecutive pairs of points within the 2D coordinate space (x, z) and N is the total number of points. Mathematically, this can be represented as:

$$E_{avg} = \frac{1}{N} \sum_{j=1}^{N-1} \sqrt{(\mathrm{x}_{j+1} - \mathrm{x}_j)^2 + (\mathrm{z}_{j+1} - \mathrm{z}_j)^2} \tag{3.1}$$

The Standard Deviation is calculated using Euclidean distances to calculate the distances individually between each consecutive points. This can be stated as:

$$E_{std} = \mathrm{std}\left(\left\{ \sqrt{(\mathrm{x}_{j+1} - \mathrm{x}_j)^2 + (\mathrm{z}_{j+1} - \mathrm{z}_j)^2} \right\}_{j=1}^{N-1} \right) \tag{3.2}$$

Characterizing Maximum Height Variations Based on Z-coordinates: considering that the z-coordinates represent the height of the object being scanned, any discrepancies or anomalies, such as those caused by reflections, are expected to create significant deviations from the average, since these points will stand out due to their substantial difference from the rest of the data. The maximum absolute value of the difference between each z coordinate value and the mean z coordinate value is an error metric that may also be helpful to identify outliers. Mathematically, this can be represented as:

$$E_{z,max} = \max_{j=1}^{N} \left| \mathrm{z}_j - \frac{1}{N} \sum_{i=1}^{N} \mathrm{z}_i \right| \tag{3.3}$$

3.6 Vision-Based Inspection Framework Design

The vision-based framework aims to achieve its objective by automated steps to conduct regular scans during the building process to generate a 3D reconstruction that can be compared to the height of the STL model. Through comparative analysis of various reconstructions, it is possible to derive insights into the building process, which may subsequently inform adjustments to optimize the MELTIO's parameters or the toolpath of the robot to enhance the overall quality of the final product.

For integrating a vision-based framework, our research explores mainly to utilize the KUKA Industrial robot system, which has a 6 DOF robot arm and 2 DOF rotating table for examining any deviation in an ongoing build. Due to the VC Nano 3D-Z only receives a single profile scan, a comprehensive 3D reconstruction requires several scans across the entire object. From the 3D reconstruction, a comparison is made between the point cloud and corresponding height of the STL model. By applying the RANSAC algorithm to fit a plane to the point clouds of the base and scanned top layers, the height can be estimated between the base plate and the current layer. This step is crucial for accurate height deviation estimation. The need for such precision arises from experiences of earlier experiments, where minor camera inaccuracies due to potential tilt, along with potential warping of the bottom plate caused by heat, led to issues with the experiment. By employing robust methods for plane fitting and rotation matrix determination, it can effectively handle noisy data and account for outliers and other errors, ensuring a reliable alignment of the layers and a better precision of height deviations. Identifying these errors, it enables thorough quality control, and corrective measures can be taken in the subsequent system to rectify or investigate the error.

3.6.1 Data Acquisition and 3D Reconstruction

The prior studies in the specialization project explored the use of ArUco markers and a rotational table as a potential method for 3D reconstruction, as seen in Appendix B. It was observed that the deployment of markers was constrained and inadequate in certain scenarios, and susceptible to distortion due to various environmental factors, such as occlusion and lighting conditions. ArUco markers were chosen at the beginning, as images taken from different angles can be registered to the same reference frame. This allows for the construction of dense point clouds from multiple viewpoints. This implies that geometric deviation can be computed of the entire object, and not only at one height. However, the experiments for this process involves using a 2 DOF rotation table to rotate the object while the scanner remains in a fixed position. This method requires knowledge of the axis of rotation relative to the scanner, and measurement of the angle of rotation for each captured scan. While this approach effectively captures the geometry, it does have certain limitations. These include the requirement for additional hand-eye

calibration, as described in Section 2.4.2. However, incorporating this type of calibration routine will additionally introduce uncertainties and inaccuracies [52]. Furthermore, this method demands considerable setup time and needs further refinements to automate the process. In contrast, the second method involves using a robot arm to move the scanner in a single axis, as seen in Figure 3.5. This approach do not require any calibration and setup time compared to the first method since it only requires a constant step relative to the building coordinates of the robot. The use of a robot arm introduces other complexities, such as ensuring accurate positioning and alignment of the robot and maintaining its stability during the scanning process.

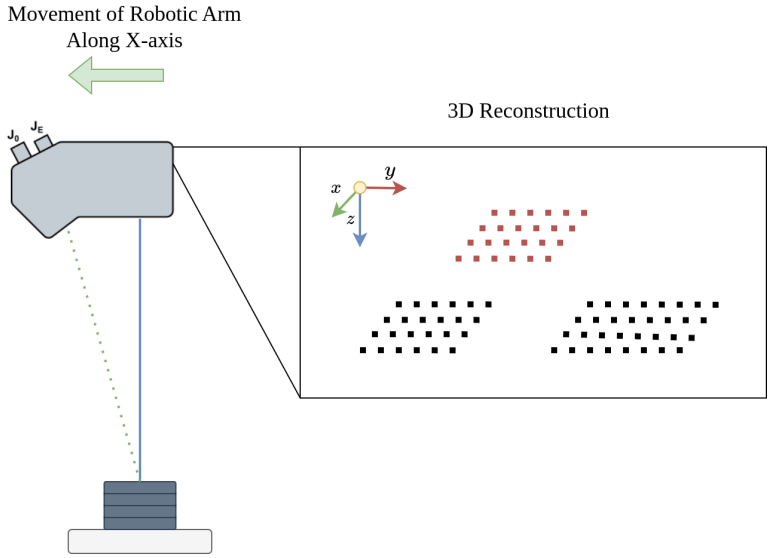

Figure 3.5: Illustration of the 3D reconstruction process of the top layer utilizing the VC Nano 3D-Z integrated with KUKA Industrial robot moving in the direction of the green arrow.

Both methods have their advantages and disadvantages, and the selection of a method would depend on factors such as the size and complexity of the object being scanned and the overall desired level of accuracy. Upon analysing the advantages and disadvantages of the two methods for performing 3D reconstruction, the second method utilizing a robot arm seems to be a more reliable option. One key advantage of this method is the ability to capture height deviation with higher accuracy. This is due to the fact that the robot arm can be programmed to move in a single axis, resulting in a more precise and controlled movement. The main challenge encountered with the rotation table method was in estimating the axis of

symmetry accurately, which was compounded by issues with wobbling instability on the initial test setup.

3.6.2 Pre-processing and Fine-tuning RANSAC Parameters

All the scans requires a pre-processing procedure to eliminate points that are not relevant, as most point cloud algorithms have difficulty distinguishing whether a point is a noisy point or critical part of the scanned geometry. During the experimentation process, most of the 3D reconstructions were adjusted by removing portions from both sides, and the top and bottom layers. This was necessary because the RANSAC algorithm, which was used to identify these planar surfaces, struggled to do so as a result of substantial differences in their appearance or properties. While the RANSAC algorithm is primary utilized to align two point clouds, it also possesses the capability to fit a mathematical model, such as planes, within a point cloud. For a more ideal performance of the RANSAC algorithm with the dataset, fine-tuning of the specific parameters is necessary. Since the experimentation primarily involves planes, there are no need to incorporate other mathematical models to fit in the point cloud in the current experiments. Each of these parameters can be adjusted accordingly to Table 3.2.

Table 3.2: RANSAC Parameters

Parameter	Description
`distance_threshold`	Represents the maximum distance from the plane at which a point can be considered to fit the model and thus be labelled an inlier. If this value is set too high, it might lead to the inclusion of noise or an outlier.
`ransac_n`	Defines the minimum number of points that must be considered inliers for the model to be deemed a good fit. If this value is set too high, it will demand more points to ascertain a good fit.
`num_iterations`	Refers to the number of iterations the algorithm should perform. An increased number of iterations enhances the probability of finding the optimal model. This value should be set high if the point cloud has a lot of noise.

3.6.3 Plane Estimation and Alignment

After the pre-processing, the remaining result should consist of an initial scan of the base and each top layer segmented into its own point cloud. The base serves as a reference point for measuring height deviations. Typically, when slicing a STL model, it is divided into layers of equal height. However, due to the deposition process leaving strands of material along the toolpaths rather than perfectly flat layers, the top layer's height may exhibit significant fluctuations. This is affected by the choice of infill pattern and structure when making the toolpaths. Infill structures, which are generated by these toolpaths, determine the internal structural integrity of the model. In this thesis, most experimental samples were produced using a zigzag pattern [53], which offers internal contour filling during the manufacturing of multi-layered cubes.

Several improvements were implemented throughout the experimentation process to address various errors. Initially, there was the issue of achieving accurate height measurements due to the fluctuations in each manufactured layer and the lower resolution of the zigzag pattern. In addition, the high temperatures produced during a DED process can introduce bending of the base plate. This highlights the necessity of having an alignment strategy to minimize the propagation of error through the subsequent layer. This challenge was addressed by applying the RANSAC algorithm for plane segmentation, thereby finding the best-fitting plane for each layer. By segmenting the best fitting plane of the base plate, an ideal alignment can be achieved. This alignment is based on the rotation matrix derived from the base plate, which can be used to align all subsequent layers during the construction process, as illustrated in Figure 3.6. Furthermore, the pseudocode for this algorithm can be found in Appendix E.

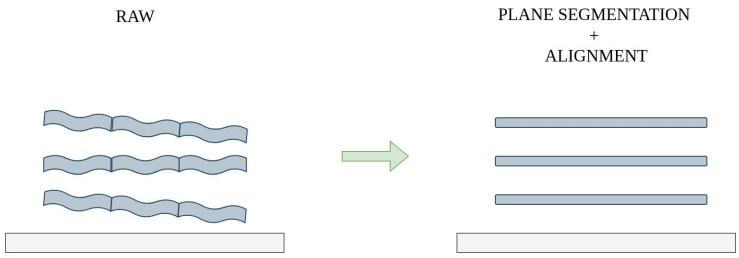

Figure 3.6: Illustration of the Plane Segmentation and Alignment process of each top layer point cloud.

Once all the layers are properly aligned, the mean value along the height dimension is calculated to estimate the height between the base and each scanned layer. This reduces the need of employing additional point cloud registration methods, such as ICP. However, due to incomplete capture of the entire object during the manufacturing process, applying ICP would become insufficient. Despite the reliability of achieving optimal alignment being highlighted in Section 3.1, the inadequate number of points would still result in an inaccurate alignment and assessment of the object's geometry.

Chapter 4

Experiments and Result

The experiments and findings from the study are presented in this chapter. Before discussing how each experiment was conducted, we will first state our experimental plan. Then, each experiment will be presented with an explanation of the setup used, along with the qualitative and quantitative results. Each experiment's findings will then be discussed in order to assess the outcomes and potential future improvements. Firstly, the experiments will investigate the quality of the VC Nano 3D-Z in a replicated environment to get results and insights for utilizing the multiple DOF of the KUKA Industrial robot. Then, the result regarding integrating a method for 3D reconstruction for the DED system outlined in Section 2.3 is presented together with a video illustrating the results and process. Finally, an empirical investigation is conducted to explore the potential for error correction, focusing on achieving the expected height by addressing deviations in measured height.

4.1 Experimental Plan

The experiments aim to gain insights to develop an automated inspection framework. This will enable monitoring of height deviations throughout the manufacturing processes in the DED system. Four experiments were developed that each

focus on a different aspect to develop the framework. Each experiment is given a brief overview in Table 4.1.

Table 4.1: Overview of the experiments

Experiment	Objective	Method
1	Optimize scanner configuration parameters.	Examine a set of four plates with diverse metal types and evaluate a range of parameters that significantly influence the results, such as shutter speed, line detection, and exposure modes.
2	Verify scanner accuracy and method for 3D reconstruction utilizing the multiple Degrees of Freedom offered by the DED system.	We compared the final 3D reconstruction of a plate, to their corresponding height based layer height of the STL model.
3	Apply the methods for detecting height error in the DED system.	Conduct 3D reconstructions after every manufactured layer, and compare each measured layer height from the 3D reconstruction to the estimated height in the STL model.
4	Examine the relationship between height deviation and layer height by measuring these deviations in order to generate a more accurate approximation of the expected height.	Utilize insights from Experiment 3 to minimize height deviation by taking the measured error into account and estimating a new layer height for improving the accuracy of the expected height.

The Franka Emika robot was initially used to refine the scanner's configuration parameters for a subset of different metal types, assuring accurate scanning in Experiment 1. Upon determining the appropriate configurations, then moved on to Experiment 2 to verify the scanner's accuracy and method for 3D reconstruction. In this experiment, Franka Emika robot was employed to verify a method for accomplishing a 3D reconstruction. Subsequently, the accuracy of manufactured objects was then determined with corresponding height in the STL model. Experiment

3 and 4 were carried out using DED system. In Experiment 3, the height errors were identified by actively scanning after each manufactured layer. Based on these findings, a method was developed to retrieve the error after every scanned layer. This method was applied to Experiment 4 to see if the measured deviation could be used to create a better estimate of the expected height.

4.2 Experiment 1: Optimizing VC Nano 3D-Z for different Metals

The fundamental issue in the a 3D reconstruction is the significant diversity in the diffuse and specular reflected light properties of metals. When utilizing laser triangulation, DED systems can create a wide range of metals onto diverse metal substrates, resulting in significant variation in diffuse and specular reflections between the metals. The purpose of this study is to evaluate various line scanner parameters with regards to the different metals used to find a set of optimal configurations for each material situation.

4.2.1 Setup

The use of a Franka Emika robot with a VC Nano 3D-Z attachment offers a regulated and dependable setup for evaluating the different combination of configurations. The scanner will be used in the subsequent experiment to scan four metal plates manufactured by the DED system. Data collection is accurate and reproducible because the robot arm keeps the laser line in the same location throughout each scan. The VC Nano 3D-Z is placed at an optimal distance of 20 cm away from the table relative to the end-effector of the robot arm, as seen in Figure 4.1. This guarantees that the data is reliable and free from outside distortions.

Figure 4.1: Illustration of the setup using Franka Emika robot arm and VC Nano 3D-Z.

One of the aspects we must consider when interpreting the results is that every metal plate consist of various patterns and shapes across the plate, as seen in Figure 4.2. Also, every plate also consists mostly of two materials: the substrate, and the top layer which is the manufactured object. We will scan a total of four metal plates with a single laser line to examine the different configurations outlined in Section 3.5.1, and each plate consists of two metal types as showcased in Table 4.2.

Table 4.2: Metal Types and their corresponding base metals for every plate sampled for the experiment.

Plate	Top	Substrate
A	Carbon Steel	Carbon Steel
B	Aluminum	Aluminum (Grit blasted)
C	Bronze	Carbon Steel
D	Stainless Steel	Carbon Steel (Grit blasted)

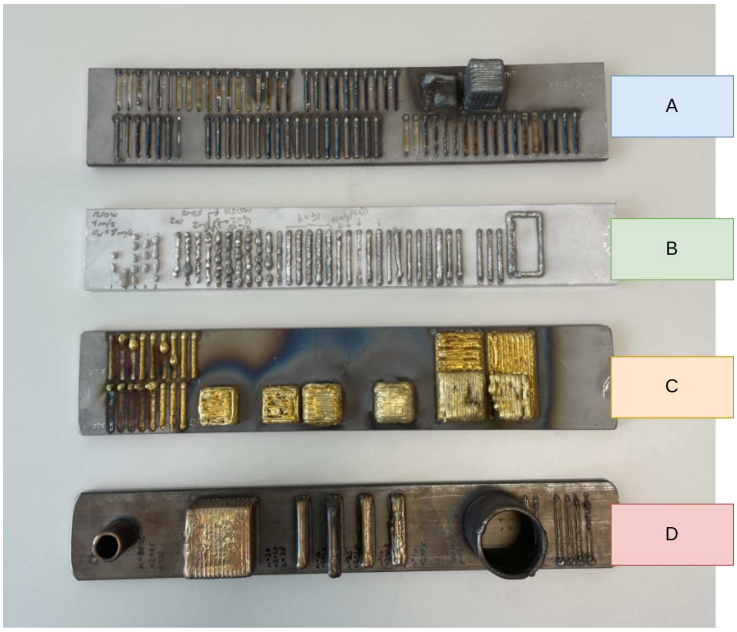

Figure 4.2: Visual illustration of all the plates utilized for this experiment.

4.2.2 Results

The results and findings of the experiment will be presented in the section that follows. Further visual representations and findings can be found in the Appendix A.

Comparison of Shutter Times of each Plate

The shutter time analysis was carried out by gathering data from 64 different shutter times, ranging from 500 μs to 10,000 μs on each plate. Table 4.3 shows the five best shutter times for each plate based on the error metrics, described in Section 3.5.1. A comparison of Plate A and C reveals that the plate samples had substantial differences. Even though the shutter times on the two plates are equal, Plate C shows higher errors for all metrics. Plate D has a higher degree of variation in terms of values, despite Plates B and D having relatively low shutter periods. This is because the objects created on Plate D have significant height discrepancies.

Table 4.3: Best Shutter Times for each Plate

Plate	Shutter Time [μs]	Avg. dist. [mm]	Standard Deviation [mm]	Variance [mm]	Max Error [mm]
A	**9950**	**0.325152**	**0.612833**	**0.375564**	**13.3113**
	9500	0.325417	0.613697	0.376624	13.3072
	8750	0.32556	0.61455	0.377672	13.3084
	9800	0.325746	0.614687	0.377841	13.3196
	9650	0.326159	0.616378	0.379922	13.308
B	**3800**	**0.315711**	**0.581551**	**0.338201**	**17.7838**
	3950	0.315927	0.580892	0.337436	17.7809
	3350	0.316282	0.582754	0.339602	17.7899
	3650	0.31642	0.57983	0.336203	17.7909
	3050	0.31657	0.581484	0.338123	17.788
C	**9950**	**0.357283**	**0.932996**	**0.870482**	**15.8173**
	8750	0.358721	0.933767	0.87192	15.8202
	9500	0.358853	0.935753	0.875634	15.8044
	9800	0.358982	0.934683	0.873632	15.8067
	9350	0.359225	0.934093	0.872529	15.7959
D	**2600**	**0.508492**	**2.03241**	**4.13069**	**13.5345**
	2450	0.509201	2.0249	4.10024	13.6221
	1550	0.510621	2.05992	4.24328	13.5512
	1700	0.510743	2.04409	4.1783	13.5542
	1850	0.511085	2.03189	4.12859	13.5033

Comparison of RLC Threshold

The optimal RLC threshold values were discovered by iterating all values from 20 to 40. Table 4.4 shows the five best RLC Threshold value for every plate and the corresponding best shutter time for each plate found in Table 4.3. Plates A and C had values that were comparable, but Plate D had the lowest value. This result implies that when higher shutter times and RLC threshold values are employed to Plate D, scattering may have an effect on the intensity of the light emitted from the laser line scanner and the RLC threshold value. This suggests that when the shutter periods and RLC threshold values increase, the light emitted by the laser line scanner gets diffused, resulting in a drop in the intensity of the light collected by the sensor and, consequently, lower values as seen in Plate D.

Table 4.4: Best RLC Threshold for each plate

Plate	RLC Threshold	Shutter Time [μs]	Avg. dist. [mm]	Standard Deviation [mm]	Variance [mm]	Max Error [mm]
A	**30**	**9950**	**0.324948**	**0.612689**	**0.375388**	**13.3013**
	29	9950	0.329797	0.650902	0.423673	13.3233
	31	9950	0.330628	0.628991	0.39563	13.291
	32	9950	0.33621	0.645828	0.417094	13.2592
	33	9950	0.341164	0.65815	0.433161	13.2536
B	**28**	**3800**	**0.310809**	**0.563714**	**0.317774**	**17.78**
	30	3800	0.31579	0.579743	0.336103	17.7965
	29	3800	0.316025	0.578341	0.334478	17.7818
	32	3800	0.316243	0.584489	0.341628	17.7886
	31	3800	0.3165	0.583951	0.340998	17.7978
C	**29**	**9950**	**0.348094**	**0.893221**	**0.797844**	**15.8777**
	30	9950	0.35659	0.929644	0.864238	15.8336
	31	9950	0.363956	0.953084	0.908369	15.7938
	32	9950	0.372201	0.98969	0.979487	15.7839
	33	9950	0.375627	1.09427	1.19744	15.7738
D	**20**	**2600**	**0.432143**	**1.84543**	**3.4056**	**25.8308**
	21	2600	0.44286	1.87953	3.53264	26.0387
	22	2600	0.459577	1.9298	3.72412	26.2464
	25	2600	0.460927	1.92575	3.70851	26.5727
	23	2600	0.466992	1.94918	3.79931	26.3704

Comparison of Exposure Modes

The three distinct exposure modes were triggered in order to obtain the results. In exposure mode 0, the user had the option to choose a fixed shutter time, where the best shutter time was utilized for every plate. Exposure Mode 1, enabled the scanner to automatically adjust the shutter time and gain value based on available light in our scene. The shutter time and gain value were each set within a specified range, with distinct minimum and maximum values established for both parameters, dependent on the lighting conditions. This setting is typically utilized in unpredictable lighting situations. The last exposure mode 2, enables two shutter times (Double Shutter 1 and Double Shutter 2) for capturing each plate, which will help to remove underexposure of the darker areas or overexposure of the brighter areas on the surface we are scanning. To determine the most optimal shutter time, heatmaps were generated to evaluate the correlation between shutter times and error metrics, as seen in Appendix A. The results showed that the distribution of the heatmap was even across the error metrics, indicating that there was no significant correlation between the two variables and that the chosen shutter times were not highly influential in determining the error values. Table 4.5, showed the results that Plate A, Plate C, and Plate D had the lowest overall error rate when using exposure mode 1. On the other hand, Plate B demonstrated a lower error rate when using exposure mode 0. These findings suggest that for Plate B, maintaining a fixed exposure time was more effective in producing accurate results, while for Plates A, C, and D, using the automatic exposure adjustment provided by mode 1 resulted in the lowest error rate.

Table 4.5: Best Exposure Modes for each Plate

Plate	Exposure Mode	Shutter Time	Double Shutter 1	Double Shutter 2	RLC Threshold	Avg. dist. [mm]	Standard Deviation [mm]	Variance [mm]	Max Height Error [mm]
A	0	9950	-	-	30	0.325425	0.613128	0.375925	13.3076
	1	**-**	**-**	**-**	**30**	**0.269357**	**0.440213**	**0.193787**	**13.9923**
	2	-	425	600	30	0.284135	0.492843	0.242894	13.317
B	**0**	**3800**	**-**	**-**	**28**	**0.310748**	**0.559681**	**0.313243**	**17.7722**
	1	-	-	-	28	0.327161	0.667277	0.445259	17.8487
	2	-	325	300	28	0.325196	0.651993	0.425095	18.0311
C	0	9950	-	-	29	0.34851	0.883223	0.780083	15.885
	1	**-**	**-**	**-**	**29**	**0.29718**	**0.611672**	**0.374143**	**16.965**
	2	-	125	450	29	0.315439	0.717745	0.515158	17.6413
D	0	2600	-	-	20	0.433359	1.84566	3.40646	25.7589
	1	**-**	**-**	**-**	**20**	**0.387327**	**1.56973**	**2.46406**	**23.8635**
	2	-	185	850	20	0.426653	1.81839	3.30654	25.9622

Visual Comparison of Finding the Ideal Shutter Time

The provided results visually compare iterations through a small portion of shutter time configurations tested for Plate B, where the ideal shutter time was determined to be 3800 μs. Figure 4.3 displays the progression of thee shutter times, leading to identification of the ideal shutter time based on the error metrics. Each of the results for all the configurations tested are available in an easily accessible HTML format in the code repository. Figure 4.3a illustrates the loss of points in the center, potentially due to inappropriate parameter settings. In contrast, Figure 4.3b reveals the generation of numerous outliers due to an excessively high shutter time configuration. Ultimately, Figure 4.3c displays the final results obtained, providing evidence that the selected error metrics functioned effectively to find the parameter configurations for the scanner.

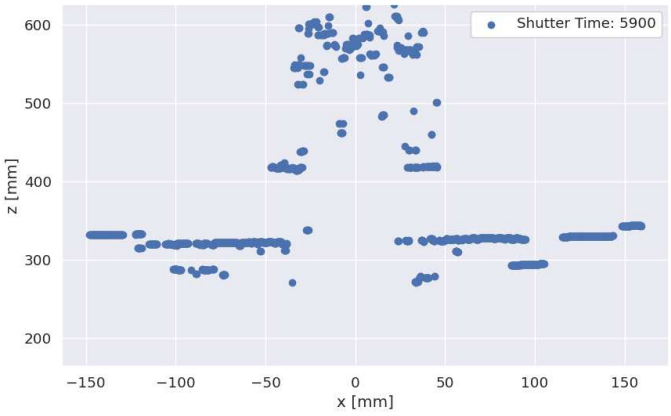

(a) Shutter time of 5900 μs.

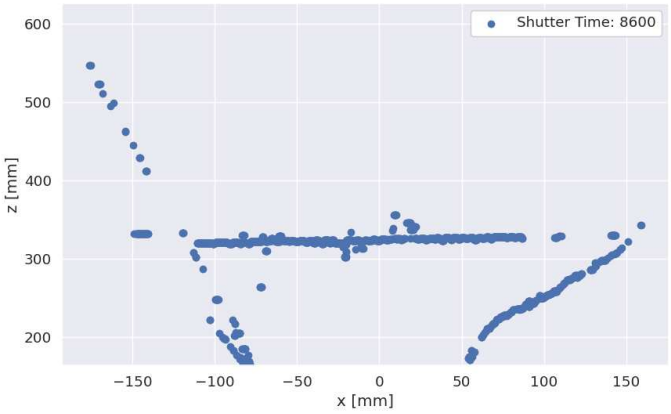

(b) Shutter time of 8600 μs.

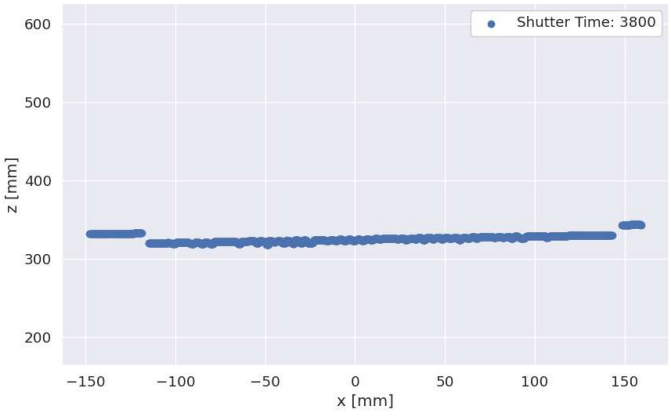

(c) The ideal Shutter Time discovered was 3800 μs.

Figure 4.3: An example of the process of determining the best shutter time based on the error metric, using Plate B as an example.

4.2.3 Discussion

Surface Roughness and Scanning Path

The chosen parameters for the experiment were carefully selected to be a representative subset of possible configurations and were heavily influenced by the shutter time parameter. Each plate presented unique geometrical variations, which impacted the results and challenged the efforts to identify optimal configurations. The roughness of each plate varied a lot because a portion of the base plate were grid blasted, which introduces random deviations in surface texture and increases the complexity of the reflection patterns for the laser. Normally, the laser line scanner would only pick up diffusely reflected light in a perfect scanning scenario, and not any specular reflection. However, when scanning over highly textured surfaces and edges, the sensor may also pick up specular reflected light, resulting in outliers. To reduce the occurrence of outliers, it may be beneficial to plan a scanning path, as earlier described in Section 2.6.

High variation in Reflection

According to the findings, which are presented in Table 4.3, Plate A and C had the lowest overall reflectivity among the plates examined. Due to the decreased reflectance in these plates, a longer optimal shutter time of 9950 μs to capture sufficient light was tested. Upon examining the data, we found that only the base of Plate A was captured. In standard operating conditions, the scanner is calibrated to only capture diffusely reflected light, effectively nullifying specular reflection. However, during the process of scanning edge features, there may be instances where the sensor inadvertently intercepts specular reflected light. This can happen due to the angle of incidence coinciding with the angle of reflection on the edges. Such incidents can lead to data outliers. This highlights the inherent difficulties in capturing the entirety of the plate when faced with low object diffuse reflection, issues which were present in both Plate B and D. Additionally, it was discovered that high reflecting objects produced more outliers depending on the intensity of the specular reflective light. We have observed a high correlation between the shutter time and geometric variations, particularly at edges of the scanned object,

as expected by the theory in Section 2.6. The findings show that both the material reflection and the geometric structure affect the number of outliers generated.

Low Reflectivity with Exposure Mode 0

The results of our experiment indicate that exposure mode 0, was not effective when dealing with the low reflection of Plate A. The issue lies with exposure mode 0, which employs a fixed shutter time that has proven to be insufficient for capturing the details of the metal type of the base. In our experiment, we found that even after testing a range of shutter times, a higher shutter time was necessary to adequately capture these details. However, our results also point out the benefits of utilizing exposure mode 1. Exposure mode 1 is better suited for capturing images with low reflectivity, as it incorporates an iterative process between the shutter time and gain to achieve ideal results.

Figure 4.4 demonstrate the clear differences between exposure mode 0, 1 and 2. It is important to keep in mind that the best exposure mode will differ depending on the reflectivity of the object being captured, the lighting, and the desired result. However, our work emphasizes the need of taking into account the interaction between shutter duration and gain when selecting an exposure mode. Additionally, our findings imply that exposure mode 1 would be a superior option in the future for similar metal characteristics, particularly when working with low reflectivity metals. While exposure mode 2 effectively accommodates highly differing reflectivity between the base and manufactured object.

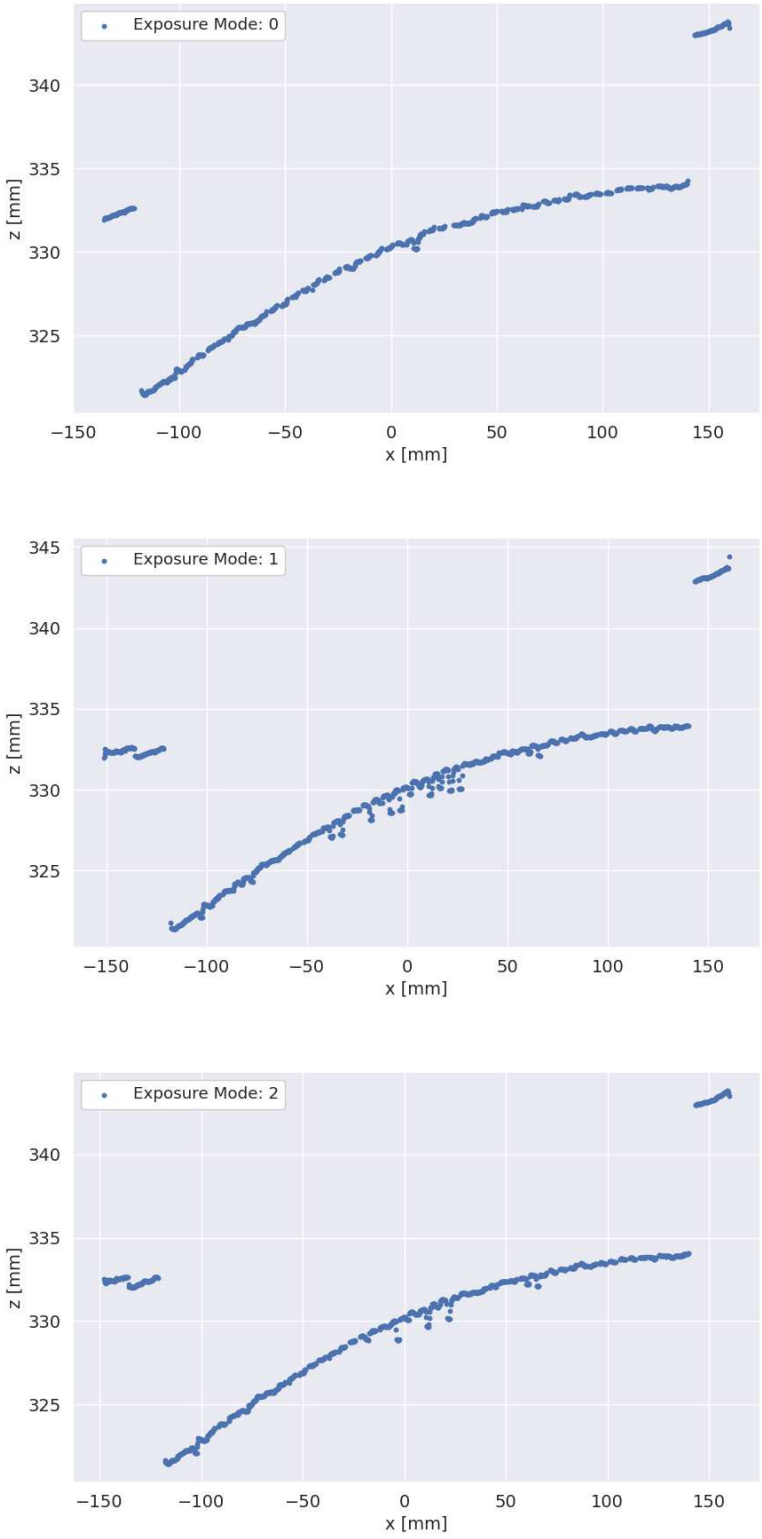

Figure 4.4: Illustration of exposure mode 0, 1 and 2 of Plate A. Exposure mode 1 is a closer resemblance to Plate A.

4.3 Experiment 2: Top Layer Inspection with VC Nano 3D -Z

An accurate and valid 3D reconstruction is essential for ensuring the framework will work as desired. However, prior testing and experimentation in the specialization project [6] has only been conducted on Polylactic Acid (PLA) manufactured objects, which is not an accurate representation of objects being manufactured by a DED process. In this experiment, different layered cubes manufactured with DED are inspected and the measured heights of the top layer are compared to the expected height from their corresponding STL model.

4.3.1 Setup

This experiment uses the same setup as Experiment 1, with a Franka Emika Robot and a VC Nano 3D-Z attached to the end-effector. The robotic arm will travel in linear steps of 0.1 mm, performing a scan after each stop, to create a 3D reconstruction of the entire plate. The scanner configuration parameters that performed best for all plates in Experiment 1 is chosen for the reconstruction.

For this experiment, three different cubes are being scanned, as seen in Figure 4.5. These cubes have been purposely built with a variety of layers throughout the plate. Also, each cube has been designed so that it is easy to compare it to the relevant STL model. It is anticipated that each layer will have a uniform height of 0.98 mm, and length and width of 14 mm. The following cubes in the associated STL file should therefore have heights of 2.94, 4.90, and 6.86 mm. This experiment examines the gap between each cube's height and the predicted height provided by the STL model, ultimately examining the height deviation by simply computing the distances between the points to the desired height.

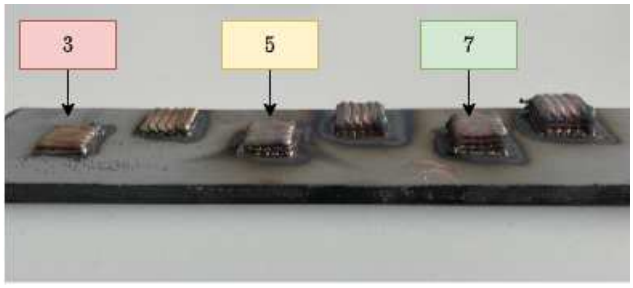

Figure 4.5: The final outcome of various layered cubes produced by the MELTIO system, annotated with the number of layers in the cubes. The cubes behind represent a separate experiment.

4.3.2 Results

The results and findings for this experiment will be presented in the section that follows.

Comparisons of Measured Error of the Heights

In examining the height discrepancies between each top layer and mesh, the accuracy and comparisons of measured heights of the 3D reconstruction were also assessed. To achieve this, a generated planar mesh of the top layer derived from the 3D reconstruction served as the reference for guiding the manual alignment for each of the three cubes. Figure 4.6 illustrates how each cube's STL model was aligned with the scanned top layers. Additionally, height deviation from the scanned top layers is then presented in Table 4.6 as a mean value. Furthermore, it is noteworthy that the cube, whose height was accurately measured at 7.22 mm, demonstrated an anomalously increased layer height. This irregularity was traced back to an error that occurred during the manufacturing process. By analysing the overall data, we were able to observe the increase of fluctuations in the measured height discrepancies between each of the layered cubes, and this divergence increased as the number of layers was increased.

To transform the measured distances into frequency data, we categorized the distances into interval of 0.1. The distance intervals were based on their proximity to the intended height of the STL model, as shown in Figure 4.7. Additionally, the

results demonstrated correlation between the number of layers and the magnitude of error. Lastly, Figure 4.8 combines all the frequency plots into one for a direct comparison.

Table 4.6: Comparison of Manufactured Cube Height and corresponding Mesh Heights

Layers	Measured Cube Height [mm]	Mesh Height [mm]	Height Error [mm]
3	3.0	2.94	0.06
5	4.99	4.90	0.09
7	7.22	6.86	0.36

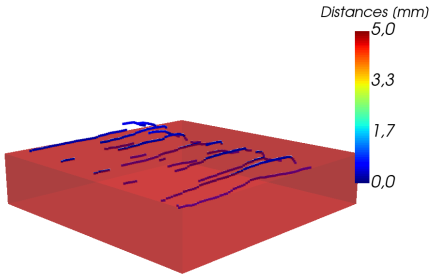

(a) 3-layered Cube

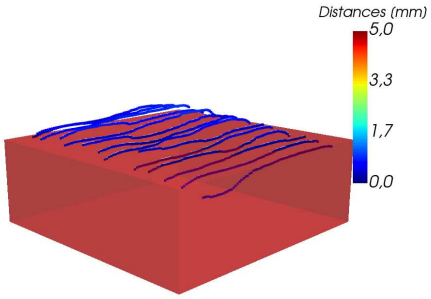

(b) 5-layered Cube

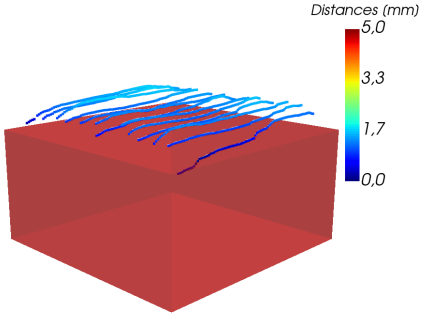

(c) 7-layered Cube

Figure 4.6: Illustration of each top layer and their corresponding STL model to compare the height deviation for 3-layered, 5-layered, and 7-layered cubes.

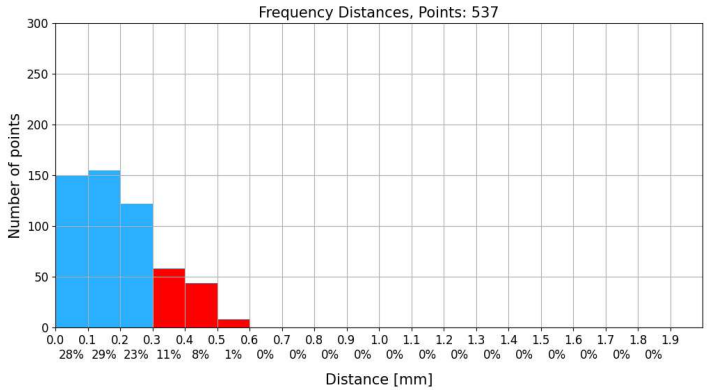

(a) 3-layered cube

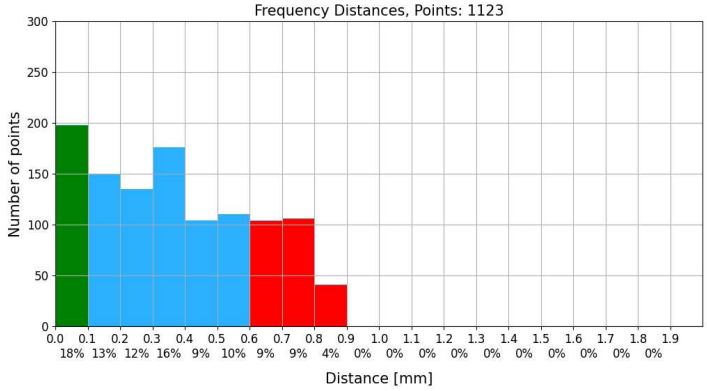

(b) 5-layered cube

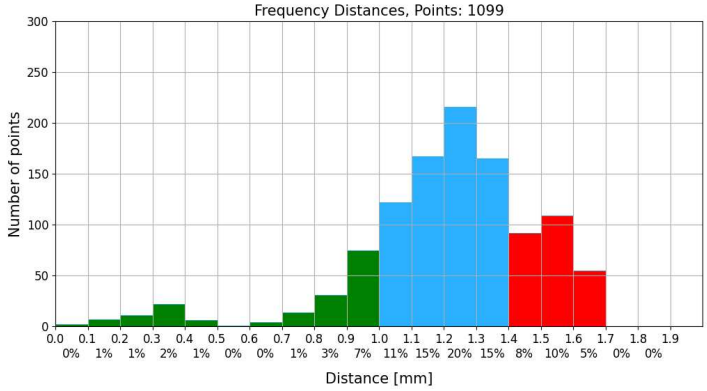

(c) 7-layered cube

Figure 4.7: Comparison of frequency distances for 3-layered, 5-layered, and 7-layered cubes.

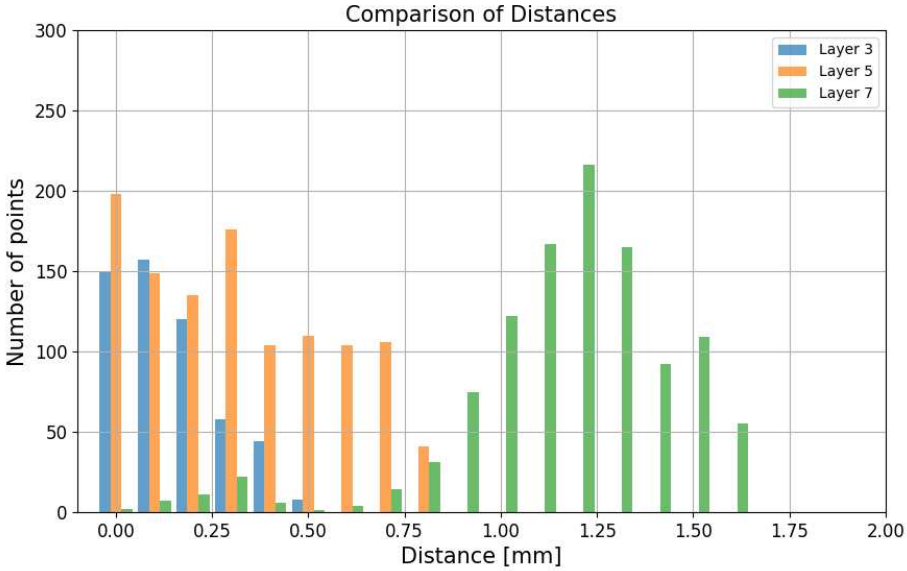

Figure 4.8: All the frequency of the distances visualized together for comparing each cube to each other.

4.3.3 Discussion

Discrepancy between Expected and Manufactured Heights

The rising inaccuracy with the number of layers being made was one of our most significant findings. In addition, the surface on top of each cube is not perfectly flat and is made up of eight curvature strings stacked one on top of the other. This implies that the surfaces are not flat in relation to the STL model, as seen in Figure 4.9, and that the curvature surfaces add some extra reflectiveness, causing a small amount of fluctuation in the measurement of the error. This source of error led to the development of a plane segmentation using RANSAC to extract the height of each layer, as described in Section 3.6.3. This method was subsequently applied for future experiments.

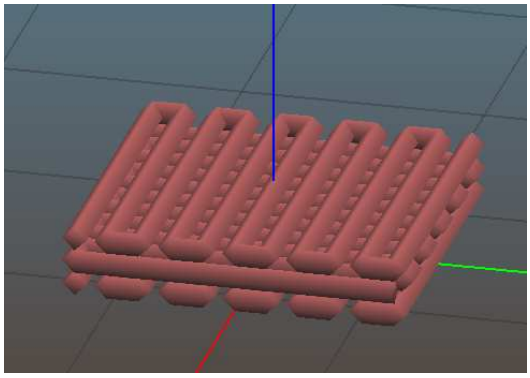

Figure 4.9: Preview of toolpath generated from the STL model of the 3 layered cube in the software named Slic3r.

Increased Height Error with Number of Layers

The manufactured cubes were manually constructed using toolpaths, which, due to their small size, resulted in lower resolution cubes. There are significant differences between expected and desired height. It is important to highlight that wire-based DED techniques have a lower resolution than some alternatives, but a higher deposition rate and the ability to manufacture larger objects. The DED technique has limits, despite its benefits. Recreating small features or sharp corners is particularly challenging with this process, as the resolution may be insufficient

to accurately capture the geometrical complexities of the STL model. In addition, the deposition process can be affected by thermal effects such as residual stress and distortion, which can result in variations in the material properties of the deposited material and the corresponding STL model. The measured height of the cubes gradually increases with the number of layer manufactured. The final cube's anticipated height was 6.86 mm, but it was actually constructed with a height of 7.22 mm, indicating that the inaccuracy has been gradually getting worse with each layer. This cube saw substantial temperature rises during the manufacturing process, which increased height deviation. This behaviour of changes in process parameters will highly affect the final object, including the process's sensitivity to parameter changes and the accumulation of errors over successive layers of deposition. The cubes were constructed using a string-based approach for the toolpath. It was discovered that the length of the string can be adjusted to achieve a more accurate representation of the cube, depending on the working distance between the nozzle and the plate, as illustrated in Figure 4.10. By optimizing the working distance based on the measured error of each cube, it is possible to create more accurate cubes. This was also described in Subsection 2.7.3 of the related studies.

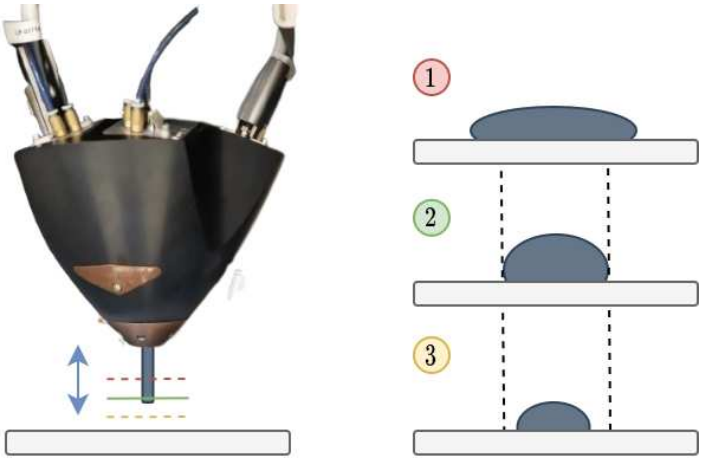

Figure 4.10: In the MELTIO system, the height and width of the string depends on the distance between the nozzle and the printing bed (also the focal point). As the printing head moves up or down, the height and width of the string changes accordingly. This height control allows for precise layering and shaping of the manufactured object, while the nozzle diameter affects the resolution and speed of the printing process.

4.4 Experiment 3: Layer-wise Height Deviation in a Manufacturing Process

The experiments conducted so far have not been tested in an active DED process. The Franka Emika Robot and the KUKA Industrial Robot are sourced from different suppliers, resulting in two completely distinct systems. As such, the primary objective is to integrate the scanning setup with the DED system in order to achieve inspection during the manufacturing process. In this study, we examine the same method that was previously used for 3D reconstruction, but this time for each layer in the active manufacturing process for analysing height variation through the entire process.

4.4.1 Setup

For this experiment, the VC Nano 3D-Z will be integrated into KUKA Indsutrial Robot system outlined in Section 2.3. Whenever a layer is finished, a new scan will be performed by incrementally translating along the x-axis in linear steps of 0.5 mm. The KUKA Industrial Robot initiates its operation from a pre-defined starting position, then progresses linearly along the x-axis before reverting to the prior pose in order to continue to the next layer. This experiment utilizes a cube with dimensions of $24 \times 24 \times 10$ mm. Each layer is designated to have a thickness of 1.0 mm, and carbon steel serves as the primary metal type employed in the experiment.

4.4.2 Results

The following section will present the experiment's findings and results. As discovered in Experiment 2, the utilization of the RANSAC plane segmentation method for each consecutive top layer offers a more accurate representation to the STL model. These results are presented using both mean calculations and plane comparisons. The final result of the cube manufactured can be seen in Figure 4.11.

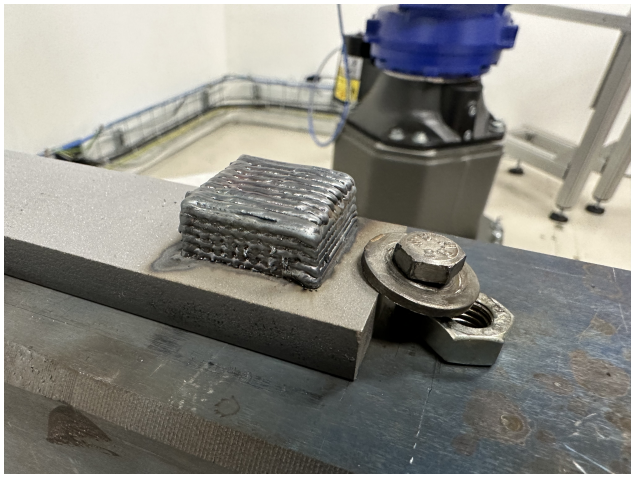

Figure 4.11: Final result of 10 layered cube with 1.0 mm layer height.

Discrepancy between each layer relative to base

Figure 4.12 and Figure 4.13 presents the final comparison of each consecutive layer with respect to the base, illustrating the representation of each layer in the point cloud after the pre-processing of the point cloud data. Figure 4.13 shows the final results, comparing each consecutive layer to the base and calculating the variance of the height deviations. The final layer exhibited a distance of 10.09 mm in the raw point cloud and 10.08 mm when derived from the segmented RANSAC planes.

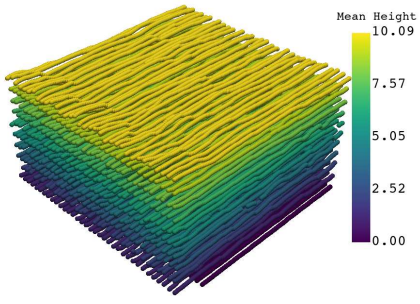

(a) Height Layer Comparisons using mean

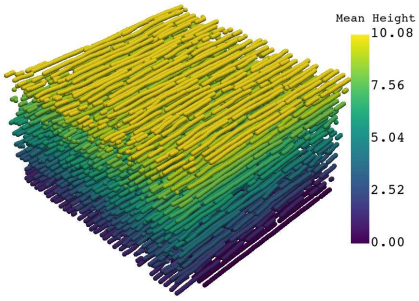

(b) Height Layer Comparions using RANSAC Plane Segmentation

Figure 4.12: Final results after cropping, aligning and comparing each layer: two methods were utilized to highlight the differences, order plane comparison using raw and RANSAC for a direct visual comparison.

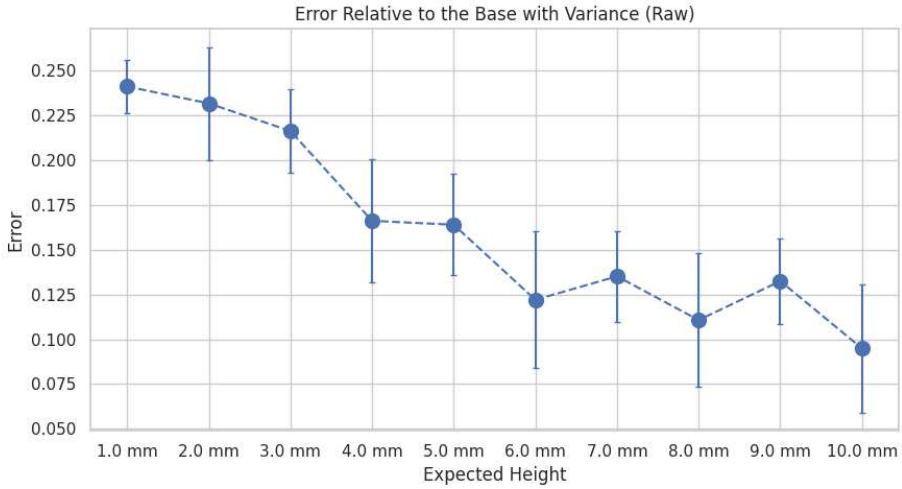

(a) Height Layer Comparisons using mean

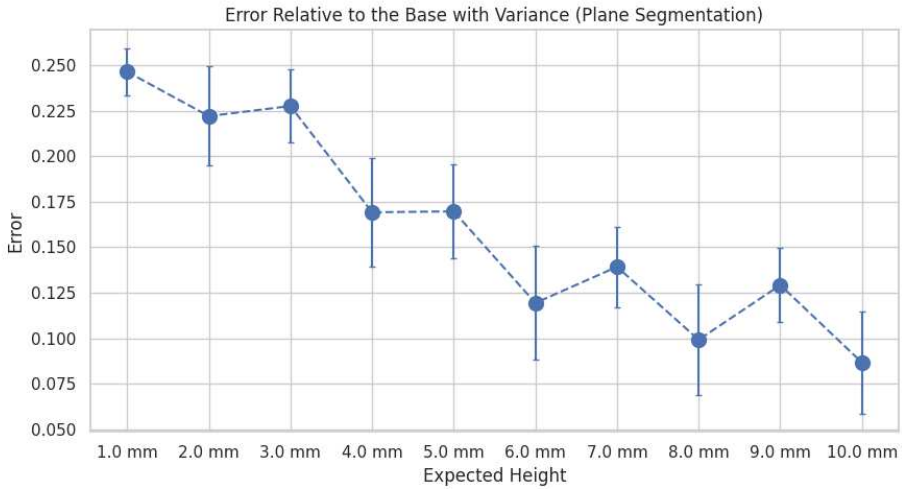

(b) Height Layer Comparisons using RANSAC Plane Segmentation

Figure 4.13: Error calculated for each layer relative to the base, using two methods: raw point cloud and RANSAC plane. Variance is determined for each point to assess uncertainties in height deviation.

Discrepancy between each consecutive layers pairs

Figure 4.14 illustrates the height deviations based on the relative differences between each layer. Ideally, the height differences between these pairs should be 1.0 mm. The first pair $(0, 1)$ has the greatest height deviation, which is most likely due to the bonding of the building plate and manufactured metal. Additionally, to uncertainties associated with using carbon steel that is still in an experimental phase in terms of determine more ideal process parameters. A small pattern can be observed, which oscillates around 0.

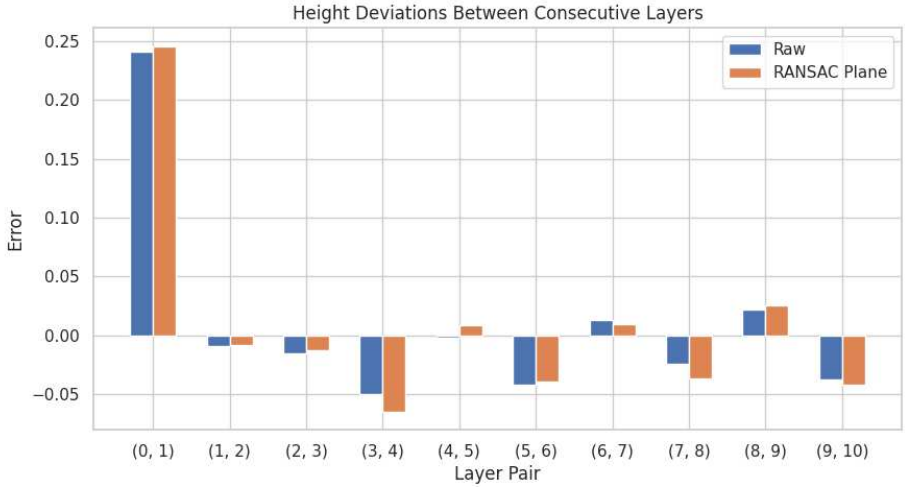

Figure 4.14: The height differences between each layer pair, where the expected layer height is 1.0 mm.

Video Results

In order to provide a deeper understanding of how the integrated hardware works with DED system, the results will show how the 3D reconstruction is integrated together with DED system, as depicted in an illustrative video presented in Figure 4.15. A compressed video, shortened from 50 minutes to 2 minutes and 30 seconds, effectively showcasing the scanning procedure between each layer. The alteration between operating in scanning and manufacturing is highlighted in the upper-left corner for reference.

Figure 4.15: QR code showcasing the Final Result. If this is being viewed on a digital device, a link is included: youtu.be/FafU_0GgmvA

.

4.4.3 Discussion

Enhancing Height Discrepancy Calculation

As previously mentioned, generating the toolpath from a STL model can lead to increasing inaccuracies. To address this issue, we implemented mean value calculations and RANSAC plane segmentation to provide a more accurate representation of the height when calculating the height deviation. Our experiment demonstrated minimal errors across each layer, resulting in a final height that closely aligned with expectations. The first built layer typically exhibits a higher error due to the bonding process, which refers to how each layer bind to the one below it. However, as subsequent layers are added, the error slowly decreases. The variance shown in Figure 4.13, which shows a large spread across the height deviation, which is probably correlated to the toolpaths.

For each layer, only a small deviation was anticipated, and our results confirmed this hypothesis. The final height of the object ranged somewhere between 10.08 and 10.09 mm, showcasing using mean value calculations and RANSAC plane segmentation for a more precise height estimation in point clouds. Due to the fluctuations in the height of the generated toolpaths, this method is a closer estimation of height instead of using the closest distance approach, as previously employed in Experiment 2.

4.5 Experiment 4: Height Optimization in a Manufacturing Process

In order to achieve the most precise geometric properties in the DED system, each metal requires their own set of parameters, which have been discovered by doing empirical research. In this experiment, we will focus examining a single parameter: layer height. The main objective is to determine how modifications to the layer height based on height measurements can bring the achieved layer height closer to the designed layer height. Throughout this study, we will explore the impact of height alternation on the desired height by investigating strategies for layer height adjustments.

4.5.1 Setup

In this experiment, a KUKA Industrial robot is employed with a VC Nano 3D-Z for scanning and a MELTIO Engine Robot for the DED process, as in prior experiment. The metal types chosen for this experiment will be carbon steel for both build plate and manufactured metal will be carbon steel. The height measurements will similarly be calculated with the same methodology used in Experiment 3 to access the height errors. Initially, three cubes will be created with a layer height of 1.075 mm, which has proven to be a good initial guess in previous experiments. The expected building height for this should be 10.75 mm at the 10th layer and 21.5 mm at the 20th layer. Accordingly, two scans will be conducted, and RANSAC plane comparisons will be used to obtain an average height across the three cubes to estimate the height and distributed layer error. Finally, a distributed error will be calculated to determine a new layer height that can be explored and empirically studied with further.

4.5.2 Results

A total of six cubes were produced, as illustrated in Figure 4.16. Which can be categorized as follows: Cube A represents the first three cubes, that were used to

estimate an average height. Subsequently, Cube B signifies the recalculated height based on the error from Cube A. Cube C represents the derived height from Cube B, but were halved due to significant error generated. Lastly, Cube D, on the other hand, is an extended version with 20 layers instead of the 10 layers used in Cube B and C to see if it is possible to produce a closer estimate of expected height at the 20th layer of 21.5 mm.

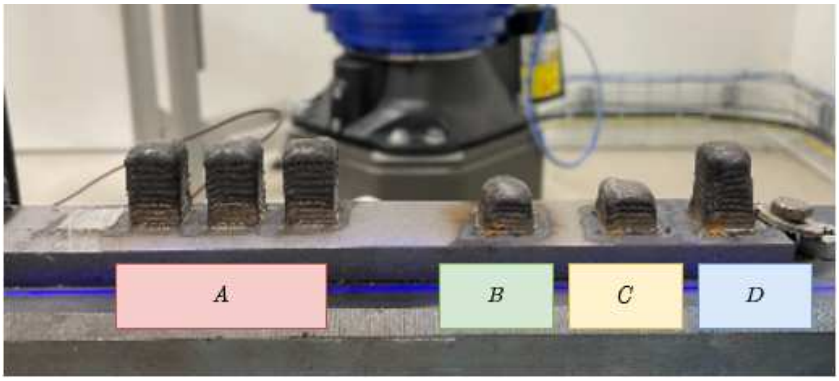

Figure 4.16: Final results of the manufactured cubes.

Table 4.7 shows the measurements taken for each cube as well as the manufacturing order. Cube A consists of a batch of three cubes, each intended to be identical in dimension, and represents the first produced cubes. Measuring the height of all three cubes, the average height computed was 10.10 mm from the scan. Subsequently, we compute the distributed error between each layer and estimate a new layer height of 1.139. This is calculated by dividing expected height by achieved height and adjusting the tool path height by that ratio: $10.75/10.10 = 1.06435$. Then, incorporating the error or ratio into Cube A's layer height (1.075 mm) an update layer height of $1.075 + 0.06435 \approx 1.139$ mm to Cube B. As a result of the updated layer height of Cube B, the error increased. This led us to estimate a new layer height by halving the error to produce Cube C, which yielded results closest to the expected height. Comparing this to Cube A and B, the results showed improvements and the height deviation was reduced significantly.

Table 4.7: Measured and expected heights of Cube A (M1, M2 M3), Cube B, Cube C, and Cube D with deviation and layer height.

Cube	**Measured Height [mm]**	**Expected Height [mm]**	**Height Deviation [mm]**	**Layer Height [mm]**
Cube A (M1)	10.1527	10.750	-0.5972	1.075
Cube A (M1)	23.1549	21.5	1.6549	1.075
Cube A (M2)	10.1086	10.750	-0.6413	1.075
Cube A (M2)	23.1719	21.5	1.6719	1.075
Cube A (M3)	10.0799	10.750	-0.6700	1.075
Cube A (M3)	23.0554	21.5	1.5554	1.075
Cube B	11.9755	10.75	1.2255	1.139
Cube C	**10.9529**	**10.75**	**0.2029**	**1.107**
Cube D	23.1068	21.5	1.6068	1.107

The objective of the layer height adjustments was to determining if it was possible to get a more closely measured cube height to the expected height. As observed in Cube C, the height was getting closer to the expected height, prompting the creation of Cube D to see if we can generate a closer approximate of 21.5 mm in measured height compared to Cube A. However, the cubes generated in this experiment exhibited very small dimensions in terms of length and width, resulting specially for Cube D of a smoother top surface and a larger height deviation.

Detecting small inaccuracy in the scanner

After the experiments, we noted slight inaccuracies in the placement of the scanner, which led to a tilted z-axis and consequently, imprecise height deviation measurements. This problem was addressed by again utilizing the RANSAC plane fitting algorithm to find a corrected rotation matrix relative to the initial scan of the base, as outlined in Section 3.6.3. The results can be corrected by utilizing RANSAC to fit a plane to the point cloud data, pinpointing the rotation to align the scanned layers with the base, thereby minimizing error.

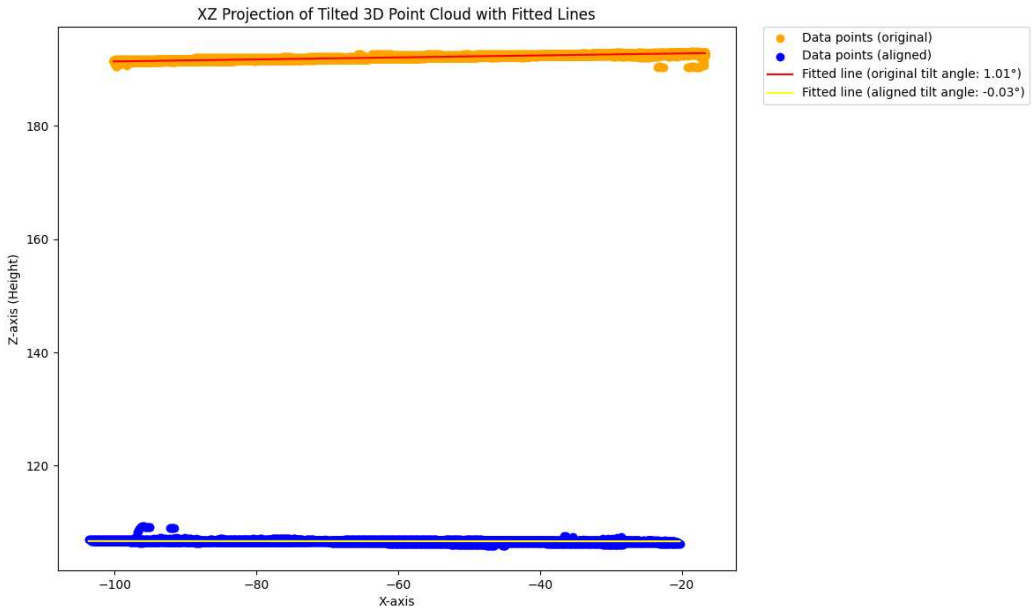

Figure 4.17: Comparison of the base plate tilt correction from Experiment 4 using RANSAC to find a more ideal rotation and correct the tilt error.

4.5.3 Discussion

Addressing Low Scan Quality and Limited Surface Area

Due to the small size of the generated cubes for this experiment, the 3D reconstruction data was limited when measuring the height. The small size also affected build because of the heat distribution issues across the surface area occurred, causing many of the cubes to become smoother at the final layers and resulted in difficulty measuring the height. This issue is closely linked to the size of the surface area and the generated cubes were the smallest currently feasible for production in DED system. The behaviour is illustrated in Figure 4.18. For example, Cube C produced a more precise height estimate of 10.9529 mm with a 0.209 mm variance. Furthermore, Cube D was created to make an attempt of expected height in Cube C at the 20th layer. However, the smaller surface area of Cube D resulted in a larger error due to the smooth surface it developed when built above the 10th layer.

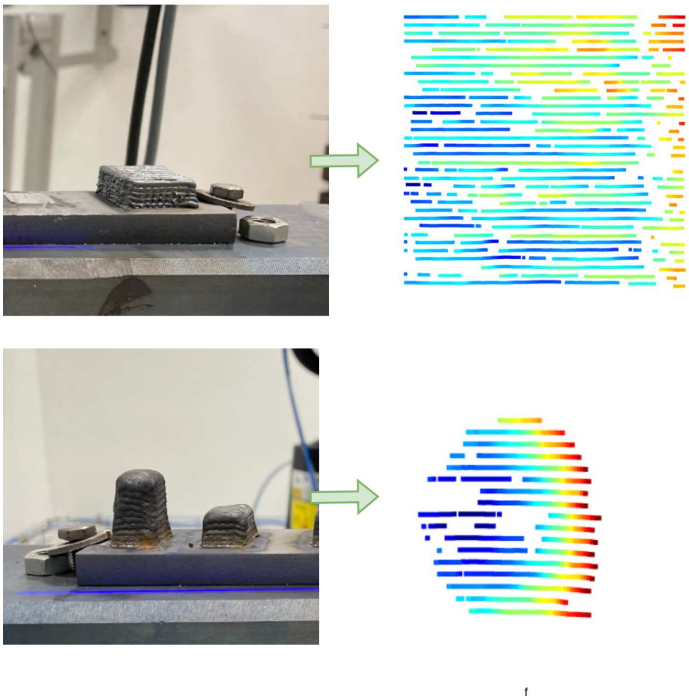

Figure 4.18: Illustrates the rounding effect on the top layer due to insufficient surface area. **Top:** scan of cube produced with width and length of 24 mm. **Bottom:** leftmost scan of Cube produced with width and length of 14.2 mm.

Correlation Related to Height Deviation

Throughout the experiment, discerning any trends or patterns related to height deviation proved challenging. As this study primarily focused on empirical research, it is plausible that some correlation exists between layer height adjustments and the final expected height. However, various factors influence the geometry, making determining an object's height difficult. Despite the challenges, measuring the deviation in the height might help to improve the final height. The findings from this experiment may not provide sufficient insights to establish a direct correlation between layer height adjustments and achieving the expected height, they do indicate that height adjustments can be modified to a certain degree during the process to reach the expected height and geometrical requirements. Further research of this link may lead to a better knowledge of what factors are impacting height accuracy, ultimately improving the representation of the 3D reconstructions.

Chapter 5

Discussion

The outcomes presented in Chapter 4 have been examined primarily on an individual basis, focusing on key highlights. These discussions also exposes several challenges related to optimizing the scanner, the 3D reconstruction process, evaluating the measuring method, height measurement, and the error metric for height deviation. This chapter generally summarizes the results and discussions to address the research questions outlined in Section 1.2. Additionally, it emphasizes any shortcomings identified throughout the experimentation, and also evaluate this type of measurement method contributing to a more comprehensive understanding of the research findings.

5.1 Evaluation on Measuring Method

A supplementary failed experiment, detailed in Appendix C, was conducted as a minor test of Experiment 4. The primary objective of this supplementary investigation was to explore the limits of attainable building height and to assess larger errors, as the height deviations observed in the previous Experiment 3 were relatively low. This further analysis aimed to enhance our understanding of the factors influencing the building process and potential challenges associated with small increase of layer heights in the DED process. Additionally, the scanning

procedure is a time-consuming, as the robot arm incrementally moves across the surface. In this experiment each scan was performed every 5th layer. However, most of the data were collected up to 35th layer, as the scanner's optimal working distance is 20 cm and the points between 35th and 45th layer were not captured. This limitation highlights one of the challenges associated with this measurement method: building large objects requires the scanner to be repositioned at a higher level between scans. Another issue discovered can be seen in the last layers seen in Figure C.3 and Figure C.4, where falling pixels are observed. This is a result of the top layer becoming more rounded rather than flat. The impact of this issue can also be easily visualized in the 3D reconstruction shown in Figure 4.18.

In conclusion, the measurement method exhibits limitations when rounded surfaces are present, as their top layer curvature could potentially influence the results and generate outliers. Furthermore, for larger objects, it is essential to adjust the scanner's height in accordance with the layers built to ensure data accuracy and prevent loss during future scans.

5.2 Experimentation Failures and Improvements

The series of experiments outlined in Chapter 4 were conducted to gain insights for improving the final framework detailed in Section 3.6. In particular, Experiment 2 led to the development of an alternative technique for comparing the top layer of the 3D reconstructions with STL model. This approach was necessitated due to the significant fluctuations observed in the toolpaths of the generated cubes. By integrating an estimated plane calculated using the RANSAC algorithm, we were able to mitigate these fluctuations, as described in Subsection 3.6.3. Consequently, this revised method offers a more reliable and accurate means of comparing these two different data types. Furthermore, in Experiment 4 a minor misalignment of the installation of the scanner was observed when measuring the heights of three identical cubes, referred to as Cube A in Table 4.7. By employing the RANSAC algorithm for plane estimation, as described in Section 3.6.3. The refined alignment, once applied to the remaining cubes in this experiment, helped mitigate some inaccuracies present in the experimental data. This process highlighted the inherent complexities for finding an optimal rotation without references within the scene

5.3 Research Questions

Based on a literature study, experimentation, and discussion, we attempt to address the research questions from Section 1.2 in the following section.

RQ1: What are the main challenges of constructing an automatic vision-based framework for a DED system?

In the investigation of various inspection frameworks discussed in Section 2.7, it was found that many are highly customized for specific AM processes. The research objective is to determine whether it is possible to measure geometrical errors using a vision-based framework and subsequently establish a feedback loop for process parameter optimization to potentially enable more complex manufacturing utilizing the multiple DOFs and a more precise geometry tailored to specific requirements. Experiment 4 demonstrates the potential use of measured height deviations, while the STL model proves to be an unsuitable comparison due to its lower resolution toolpath, resulting in significant fluctuations during height measurements, as discussed in Section 4.3.3. This issue highlights the challenge of accurately measuring height, and comparing it to a corresponding height of the STL model, this problem can be highlighted by looking at toolpath for a simple 3-layered cube in Figure 4.9. This highlights the most significant limitation of the previously developed framework, as detailed in Section 3.1. Due to the high substantial discrepancies of the top layers between the desired manufactured object and the reference STL model, which results in challenges of using point cloud registration algorithms such as RANSAC and ICP. These algorithms struggle to ensure optimal alignment due to these inconsistencies, as observed with the previous framework detailed in Section 3.6.

Another highlighted issue related to the optimization of the scanner, Experiment 1 showcased materials with high reflection can interfere with structured light patterns, leading to measurement errors. When using two distinct metals with high and low reflectivity, discrepancies may arise if the base is highly reflective and the manufactured material on top is less reflective. This difference can cause the scanner to only capture the base plate, requiring multiple iterations through

various shutter times and gains to achieve optimal results, as further discussed in Section 4.2.3. Although the DED system can manufacture multiple metals, some of them described in Table 2.1, a more comprehensive investigation into the impact of different metal types is needed to improve the quality of the scan. Potential future research could involve addressing the identified issues within the framework, a topic further discussed in Section Section 6.2.2.

RQ2: To what extent do variation in geometric complexity and metal types influence structured light-based 3D reconstruction?

In Experiment 1, we examined configuration parameters significantly influenced by metal types and geometric complexity of the objects being scanned. By investigating these parameters, we can identify the diversity of metal types. Throughout the course of the thesis, some hardware options have been explored, as detailed in Section 3.3, ultimately leading to the selection of the VC Nano 3D-Z. The VC Nano 3D-Z offers faster sampling speed and greater precision in point cloud generation. The related work on inspection in AM processes has utilized structured light-based methods for 3D reconstruction, enabling comprehensive investigations. However, it has been observed that the optical properties of metals differ considerably, as illustrated in Experiment 1. Moreover, the extensive variety of geometric shapes presents additional challenges. Factors such as sharp edges, reflective surfaces, and intricate curvatures can significantly affect the reconstruction results. To mitigate these issues, an optimized scanning path is necessary for minimizing errors and enhancing the accuracy of the 3D reconstruction, as discussed in Section 4.2.3 and illustrated in Figure 2.17.

In conclusion, structured light-based methods has their challenges when being used in a DED system, because of the inherent diversity in optical properties of metals and the wide range of geometric shapes. This creates challenges that can potentially be addressed by scanning path optimization and other techniques to assure accurate and dependable results. Further work related to this topic is discussed in Subsection 6.2.1.

RQ3: How can height deviation data optimize parameters to reduce defects and enhance product quality?

Throughout the thesis, various methods have been employed to determine height deviation. The specialization project [6] explored the use of point cloud registration algorithms to align the scanned object with the reference STL model. This approach particularly highlighted the issue arising from the non-planar height due to the toolpath, which rendered these algorithms insufficient and unable to guarantee optimal alignment. This approach was not explored until Experiment 3, where RANSAC was utilized to identify a plane for a more accurate height estimation. Figure 4.13 illustrates the layer height deviation relative to the base, but the error was too small to detect any significant differences. Based on further analysis and experimentation of the results in Experiment 3, new findings about adjusting the layer height were uncovered, as illustrated in Figure 4.10.

Therefore, Experiment 4 was conducted to investigate potential methods for adjusting layer height. The default optimal layer height for building with carbon steel was 1.075 mm, resulting in an expected height of 10.75 mm at the 10th layer. Nevertheless, the actual error was much lower, and a more optimal layer height for achieving this target was demonstrated in Table 4.7. While the results from this experiment may not represent the best method due to the issues discussed in Section 4.5.3, they do provide a proof of concept for further optimization of the process parameter, which will enable a more accurate manufacturing to achieve the desired height.

Chapter 6

Conclusion and Future Work

In this final chapter, we will conclude the thesis and discuss the further work regarding vision-based methods for automatic inspection in DED processes.

6.1 Conclusion

Directed Energy Deposition processes, as explored throughout this thesis, are inherently complex and comparatively less stable than other conventional manufacturing techniques. This emergent field of study is abundant for research possibilities and further optimization efforts to identify more ideal process parameters for constructing precise geometries with various metals. The development of a vision-based framework could pave the way for more efficient monitoring of the building process and find more ideal process parameters for the DED system for various metals. Throughout this thesis, we have examined several topics and methods utilizing the framework in the SINTEF Manufacturing's DED system. We have illustrated the impact of 3D reconstruction on different metals and geometric shapes to gain insight on the effect of using structured light-based methods in DED processes. Furthermore, to extend this knowledge, we utilized the DOF of the DED system to develop a method for 3D reconstruction, which have been both integrated and tested. Lastly, we investigated how the calculated height

deviation could be utilized for additional optimization. While most of the process parameters in DED system have been derived from prior empirical research, the data and experiments did not reveal any specific trends correlating layer height parameter with the expected height. However, the height deviation data in the final experiment showed small improvements to achieving the expected height by adjusting the layer height based on the height measurements from the framework. This has a further potential to enhance the precision of the building process, thus aiding to achieve a height closer to expected height and potentially improve the geometry. This thesis has also discussed the challenges involved in building a vision-based framework for a DED process. For instance, structured light-based 3D reconstruction can introduce multiple error sources from varying geometric shapes, include falling pixels and outliers resulting from sharp edges. As well as discrepancies caused by varying reflection from different metal types, which more research would be beneficial to unfold more ideal parameter configurations for the scanner with a wider range of metal types. Although the final framework is not yet fully automated, however, it highlights the potential of incorporating a vision-based framework into a DED process for geometric inspection of the building process and potential future research of using height deviation data as sensor feedback to further improve the geometry.

6.2 Future Work

While significant progress has been achieved in the use of a vision-based framework for DED processes, several challenging remain, including 3D reconstruction, automation, and a wider understanding of the optical characteristics of metals. The subsequent sections will highlight the potential areas for further research.

6.2.1 Improved 3D Reconstruction

A crucial component of the framework for examining the height deviation process is 3D reconstruction. It allows us to continuously monitor the condition of an object as it is manufactured. In order to capture the complete object throughout this process, a point cloud must be created. To do this, the KUKA industrial robot

must move progressively along the x-axis. The scanner's 400 Hz capture speed, which was mentioned in Section 3.4, has the potential to significantly shorten the gap between each layer's capture. However, optimizing the 3D reconstruction by synchronizing the robot's translation along the x-axis with the scanner's capture rate is a critical problem that requires additional work. One possible reason for the complexity of this synchronization is the need to accurately save poses. The scanner must capture the right image every time the robot moves, and in order to do so, it must save the robot's pose to assure the reconstruction. If the 3D reconstruction is not properly synchronized, measurement error could occur, resulting in faults in the created product. As a result, future research could concentrate on developing more effective systems for posture storing and synchronization.

The second issue, identified in Appendix C, pertains to the optimal working distance, which is around 20 cm. If the distance between the manufactured object and the scanner is not adjusted to match the height, there will be a loss of data. This can significantly impact the quality of the 3D reconstruction and, consequently, the accuracy of the manufacturing process. Therefore, future research should aim to devise strategies that can adaptively adjust the working distance to prevent data loss and ensure accurate 3D reconstruction.

In summary, despite the strides made in the application of 3D reconstruction for DED processes, key challenges persist. These include synchronization of robot movements with the scanner's capturing speed, as well as maintaining an optimal working distance to prevent data loss.

6.2.2 Impacts of Varied Shapes on Scanning Quality

As discovered in Experiment 3, the shape of an object can significantly contribute to the emergence of outliers and can potentially reduce the quality of the 3D reconstruction. The majority of the studies have used cubic forms, but it is important to recognize that more sophisticated shapes, particularly curves, edges, and distinctive surface features, may demand optimal scanning paths. Complex forms with varying surfaces and angles can present a significant challenge to the current scanning path. Curved surfaces, for example, may refract or absorb light from the scanner differently than flat surfaces, resulting in the falling pixels seen in

Figure C.1b. Similarly, edges, especially sharp or irregular ones, can cast shadows or reflect light, which might skew the scanner's results, as illustrated in Figure 2.18. This can result in data gaps or inaccuracies, which can compromise the quality of the 3D reconstruction.

Addressing these issues is a complex task. One option would be to define a sequence of scanning pathways based on the shape being created. Instead of using a uniform scanning path for all objects, the scanning process might be tailored to each object's unique characteristics. A spherical object, for example, may require a spiral scanning path, but a cuboid may benefit from a grid-based path. However, to determine the best scanning paths for various shapes is a considerable task. It is expected that algorithms capable of assessing a shape and calculating an optimal scanning path that minimizes data loss and inaccuracy. For example, techniques from several domains, such as computational geometry and machine learning, could be used.

To summarize, the shape and specific surface properties of the scanned object have a significant impact on the quality of the 3D reconstruction. Future study could concentrate on developing algorithms for optimizing the scanning path depending on the individual geoemetric properties of the object, with the ultimate goal of enhancing scanning accuracy and efficiency and overcoming problems like falling pixels.

6.2.3 Investigating the Correlation between Layer Height and Expected Height

The findings from Experiment 4 highlights the importance of adjusting the layer height parameter, a key factor in the manufacturing process. However, the MELTIO system houses a vast array of other process parameters that could be strategically manipulated to potentially improve the quality of the final manufactured object. At this stage, no conclusive correlation between these process parameters and the relationship between layer height and expected height has been established. As a result, there is a lot of room for more research in this field. Discovering a more precise correlation could greatly enhance our understanding of how these variables interplay, which could lead to significant improvements in the manufacturing

process.

In summary, more research for finding a strong correlation with layer height but also potentially other parameters to help to construct a more robust prediction model that allows for proactive changes to process parameters. Consequently, such advancements could offer a greater degree of precision in controlling the outcome of the manufactured object to their corresponding design.

6.2.4 Enhancing Automation in Detection and Calibration

In the current DED system, a calibration step is required every time an object is manufactured. This involves establishing a new coordinate system for the robot to operate within by setting an origin point, a point for the y-axis, and a point for the XY plane. While this process is necessary for accurate manufacturing, it presents challenges for automatic inspection. The profile scans from the scanner complicates the automatic segmentation and extraction of a specific object. This is due to the shifting coordinate system, which makes it challenging to consistently and automatically identify the object of interest within the data collected by the camera.

Various strategies have been proposed to address this complexity. One such method involves the implementation of manual calibration, where a plane is defined to align the coordinate systems of both the robot and scanner. Subsequently, using the origin point as a reference, the object of interest could potentially be located within the point cloud data. However, this solution presents its own unique set of challenges that need to be addressed. Further research is required to refine this method and potentially develop automated solutions that could easily locate the manufactured object in 3D reconstruction.

In summary, the object being manufactured within the point cloud is a complex task that is currently hard to automate. This automation is a critical missing element in the current framework. Typically, this process is performed manually. By identifying the object's positioning in 3D reconstruction using some sort of calibration or reference in the scene would allow for a better continuous, real-time examination of the object when utilizing the framework.

Bibliography

[1] K. S. Grönnestad, *Equinor vil ha 3d-print av reservedeler*, https://www.tu.no/artikler/equinor-vil-ha-3d-print-av-reservedeler/479443, [Accessed: 18-06-2023].

[2] N. Decker, Y. Wang, and Q. Huang, "Efficiently registering scan point clouds of 3d printed parts for shape accuracy assessment and modeling," *ScienceDirect*, vol. 56, 2020.

[3] SFI, *Centre for competitive high value manufacturing in norway*, https://www.sfimanufacturing.no/, [Accessed: 28-02-2023].

[4] L. D. Evjemo, G. Langelandsvik, and J. T. Gravdahl, "Wire arc additive manufacturing by robot manipulator: Towards creating complex geometries," *IFAC-PapersOnLine*, vol. 52, no. 11, pp. 103–109, 2019.

[5] A. H. Moltumyr, M. H. Arbo, and J. T. Gravdahl, "Towards vision-based closed-loop additive manufacturing: A review," *IEEE*, 2020.

[6] S. Adel, "Automatic inspection in additive manufacturing using computer vision," 2022.

[7] K. M. Lynch and F. C. Park, *Modern robotics*. Cambridge University Press, 2017.

[8] R. Szeliski, *Computer vision: algorithms and applications*. Springer Nature, 2022.

[9] "ISO/ASTM 52900," International Organization for Standardization, Standard ISO/ASTM 52900, [Accessed: 10-03-2023].

[10] K. Boivie, "Additive manufacturing: Background, fundamentals and standardization," *ASTME International*, 2022.

[11] H. Bikas, P. Stavropoulos, and G. Chryssolouris, "Additive manufacturing methods and modelling approaches: A critical review," *The International Journal of Advanced Manufacturing Technology*, vol. 83, pp. 389–405, 2016.

[12] *What is a stl file?* `https://www.3dsystems.com/quickparts/learning-center/what-is-stl-file`, [Accessed: 28-02-2023].

[13] 3MF Consortium, *3MF - Industry's Choice for 3D Printing*, `https://3mf.io/`, [Accessed: 14-06-2023].

[14] M. Livesu, S. Ellero, J. Martınez, S. Lefebvre, and M. Attene, "From 3d models to 3d prints: An overview of the processing pipeline," in *Computer Graphics Forum*, Wiley Online Library, vol. 36, 2017, pp. 537–564.

[15] "ISO 10303-1:2021," International Organization for Standardization, Standard ISO 10303-1:2021, [Accessed: 15-03-2023].

[16] W. Gielingh, "Requirements for the development of layered information models," in *Proceedings of the First International Conference on Enterprise Integration Modeling*, MIT Press Cambridge, Massachusetts, 1992, pp. 269–277.

[17] "ISO 10303-21:2016," International Organization for Standardization, Standard ISO 10303-21:2016, [Accessed: 15-03-2023].

[18] K. Walia, A. Khan, and P. Breedon, "Polymer-based additive manufacturing: Process optimisation for low-cost industrial robotics manufacture," *Polymers*, vol. 13, no. 16, p. 2809, 2021.

[19] A. Bernard, G. Taillandier, and K. Karunakaran, "Evolutions of rapid product development with rapid manufacturing: Concepts and applications," *International Journal of Rapid Manufacturing*, vol. 1, no. 1, pp. 3–18, 2009.

[20] K. Rajaguru, T. Karthikeyan, and V. Vijayan, "Additive manufacturing–state of art," *Materials today: proceedings*, vol. 21, pp. 628–633, 2020.

[21] "ISO 6983-1:2009," International Organization for Standardization, Standard ISO 6983-1:2009, [Accessed: 14-02-2023].

[22] H. M. Yudha, T. Dewi, P. Risma, and Y. Oktarina, "Arm robot manipulator design and control for trajectory tracking; a review," in *2018 5th International Conference on Electrical Engineering, Computer Science and Informatics (EECSI)*, IEEE, 2018, pp. 304–309.

[23] All3DP, *Directed Energy Deposition (DED): A Comprehensive Guide*, https://all3dp.com/1/directed-energy-deposition-ded-metal-3d-printing-guide/, [Accessed: 25-05-2023].

[24] Linear Motion Tips, *What is a cartesian robot?* https://www.linearmotiontips.com/what-is-a-cartesian-robot/, [Accessed: 21-03-2023].

[25] Mecademic, *What is the workspace of a typical six-axis industrial robot arm?* https://www.mecademic.com/en/what-is-the-workspace-of-a-typical-six-axis-industrial-robot-arm, [Accessed: 21-03-2023].

[26] A. El-Sherbiny, M. A. Elhosseini, and A. Y. Haikal, "A comparative study of soft computing methods to solve inverse kinematics problem," *Ain Shams Engineering Journal*, vol. 9, no. 4, pp. 2535–2548, 2018.

[27] J. Denavit and R. S. Hartenberg, "A kinematic notation for lower-pair mechanisms based on matrices," 1955.

[28] M. W. Spong, S. Hutchinson, M. Vidyasagar, *et al.*, *Robot modeling and control*. Wiley New York, 2006, vol. 3.

[29] A. Ben-Israel, "A newton-raphson method for the solution of systems of equations," *Journal of Mathematical analysis and applications*, vol. 15, no. 2, pp. 243–252, 1966.

[30] S. R. Buss, "Introduction to inverse kinematics with jacobian transpose, pseudoinverse and damped least squares methods," *IEEE Journal of Robotics and Automation*, vol. 17, no. 1-19, p. 16, 2004.

[31] Meltio, *Engine robot integration*, `https://meltio3d.com/wp-content/uploads/2022/10/Brochure_Meltio_Engine-Robot-Integration_August2022_E.pdf`, [Accessed: 25-03-2023].

[32] P. Sturm, "Pinhole camera model," in *Computer Vision: A Reference Guide*, K. Ikeuchi, Ed. Boston, MA: Springer US, 2014, pp. 610–613.

[33] C. B. Duane, "Close-range camera calibration," *Photogramm. Eng*, vol. 37, no. 8, pp. 855–866, 1971.

[34] A. W. Fitzgibbon, "Simultaneous linear estimation of multiple view geometry and lens distortion," in *Proceedings of the 2001 IEEE Computer Society Conference on Computer Vision and Pattern Recognition. CVPR 2001*, IEEE, vol. 1, 2001, pp. I–I.

[35] F. Remondino and C. Fraser, "Digital camera calibration methods: Considerations and comparisons," *International Archives of the Photogrammetry, Remote Sensing and Spatial Information Sciences*, vol. 36, no. 5, pp. 266–272, 2006.

[36] Z. Zhang, "A flexible new technique for camera calibration," *IEEE Transactions on pattern analysis and machine intelligence*, vol. 22, no. 11, pp. 1330–1334, 2000.

[37] J. Jiang, X. Luo, Q. Luo, L. Qiao, and M. Li, "An overview of hand-eye calibration," *The International Journal of Advanced Manufacturing Technology*, vol. 119, no. 1-2, pp. 77–97, 2022.

[38] H. Zhuang and Z. S. Roth, "A linear solution to the kinematic parameter identification of robot manipulators," *IEEE Transactions on Robotics and Automation*, vol. 9, no. 2, pp. 174–185, 1993.

[39] M. Ingvaldsen, *The benefits of 3D hand-eye calibration — blog.zivid.com*, `https://blog.zivid.com/importance-of-3d-hand-eye-calibration`, [Accessed: 22-03-2023].

[40] S. Garrido-Jurado, R. Muñoz-Salinas, F. J. Madrid-Cuevas, and M. J. Marın-Jiménez, "Automatic generation and detection of highly reliable fiducial markers under occlusion," *Pattern Recognition*, vol. 47, no. 6, pp. 2280–2292, 2014.

[41] A. Khazetdinov, A. Zakiev, T. Tsoy, M. Svinin, and E. Magid, "Embedded ArUco: A novel approach for high precision UAV landing," in *2021 International Siberian Conference on Control and Communications (SIBCON)*, IEEE, 2021, pp. 1–6.

[42] P. Besl and N. D. McKay, "A method for registration of 3-d shapes," *IEEE Transactions on Pattern Analysis and Machine Intelligence*, vol. 14, no. 2, pp. 239–256, 1992.

[43] M. A. Fischler and R. C. Bolles, "Random sample consensus: A paradigm for model fitting with applications to image analysis and automated cartography," *Communications of the ACM*, vol. 24, no. 6, pp. 381–395, 1981.

[44] J. M. Martınez-Otzeta, I. Rodrıguez-Moreno, I. Mendialdua, and B. Sierra, "Ransac for robotic applications: A survey," *Sensors*, vol. 23, no. 1, p. 327, 2022.

[45] Y. Wang and H.-Y. Feng, "Modeling outlier formation in scanning reflective surfaces using a laser stripe scanner," *Measurement*, vol. 57, pp. 108–121, 2014.

[46] P. Charalampous, I. Kostavelis, C. Kopsacheilis, and D. Tzovaras, "Vision-based real-time monitoring of extrusion additive manufacturing processes for automatic manufacturing error detection," *The International Journal of Advanced Manufacturing Technology*, vol. 115, pp. 3859–3872, 2021.

[47] J. L. Bentley, "Multidimensional binary search trees used for associative searching," *Communications of the ACM*, vol. 18, no. 9, pp. 509–517, 1975.

[48] I. Garmendia, J. Leunda, J. Pujana, and A. Lamikiz, "In-process height control during laser metal deposition based on structured light 3d scanning," *Procedia Cirp*, vol. 68, pp. 375–380, 2018.

[49] V. Zhou, K. Odum, M. Soshi, and K. Yamazaki, "Development of a height control system using a dynamic powder splitter for directed energy deposition (DED) additive manufacturing," *Progress in Additive Manufacturing*, vol. 7, no. 5, pp. 1085–1092, 2022.

[50] V. Components, *Vc nano 3d-z technical specification*, `https://www.vision-components.com/fileadmin/external/documentation/hardware/VC_nano_3D_Z/index.html`, [Accessed on: 23-05-2023].

[51] N. Otsu, "A threshold selection method from gray-level histograms," *IEEE transactions on systems, man, and cybernetics*, vol. 9, no. 1, pp. 62–66, 1979.

[52] J. Jiang, X. Luo, Q. Luo, L. Qiao, and M. Li, "An overview of hand-eye calibration," *The International Journal of Advanced Manufacturing Technology*, vol. 119, no. 1-2, pp. 77–97, 2022.

[53] X. Xiao and S. Joshi, "Automatic toolpath generation for heterogeneous objects manufactured by directed energy deposition additive manufacturing process," *Journal of Manufacturing Science and Engineering*, vol. 140, no. 7, p. 071 005, 2018.

Appendix A

Supplementary Visual Representations for Experiment 1

This chapter shows the additional plots that contributed to highlight some of the results in Section 4.2, as well as provide a more comprehensive look of the data and support some of the conclusions drawn. There are additional plots supplied in the code in HTML format as well, to explore the various configurations.

A.0.1 Heatmap for Double Shutter 1 and 2

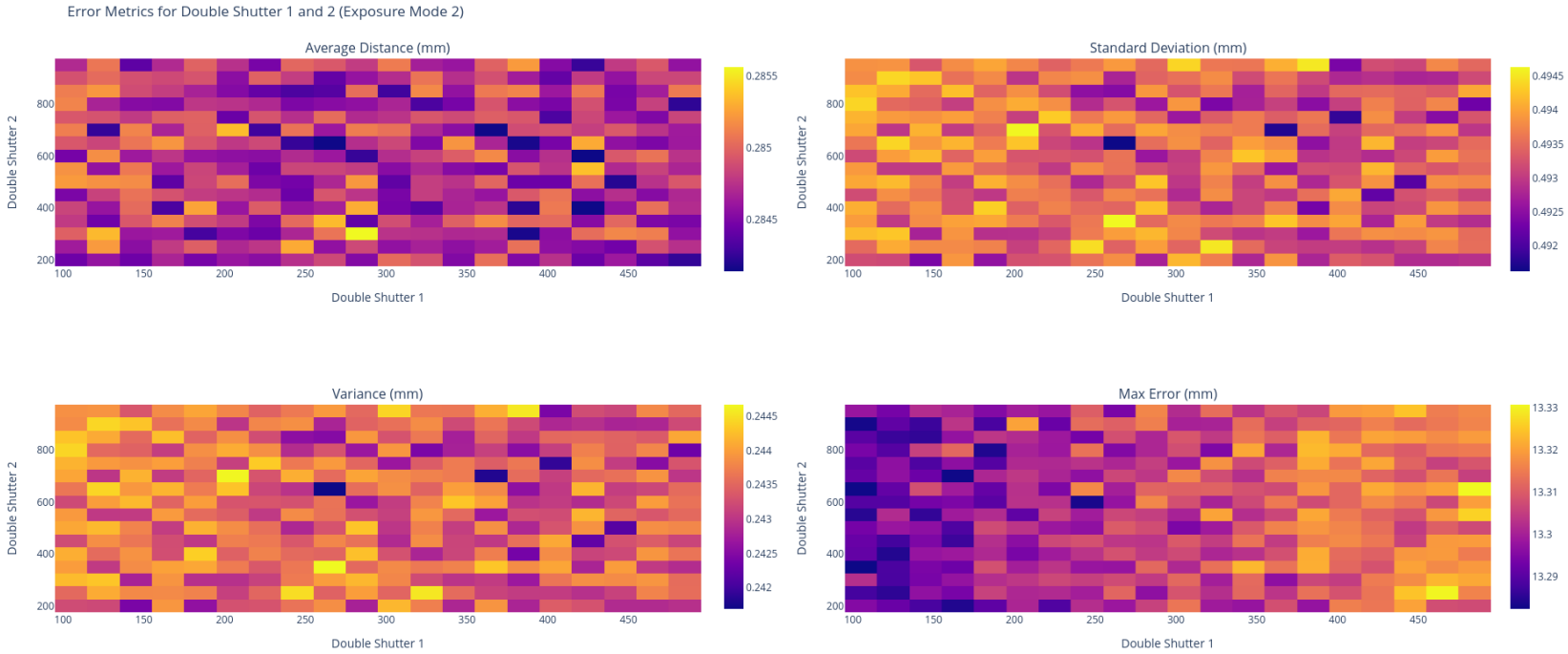

Figure A.1: Heatmap for Plate A

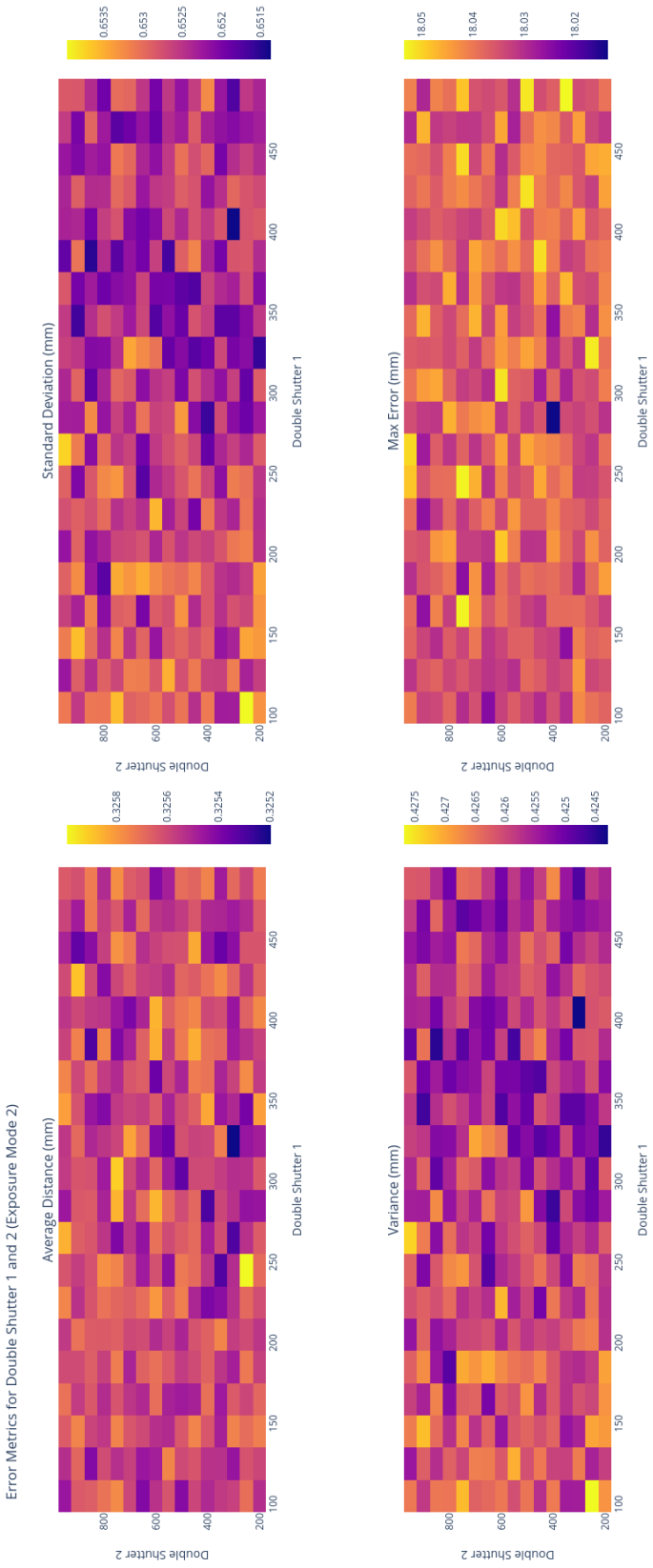

Figure A.2: Heatmap for Plate B

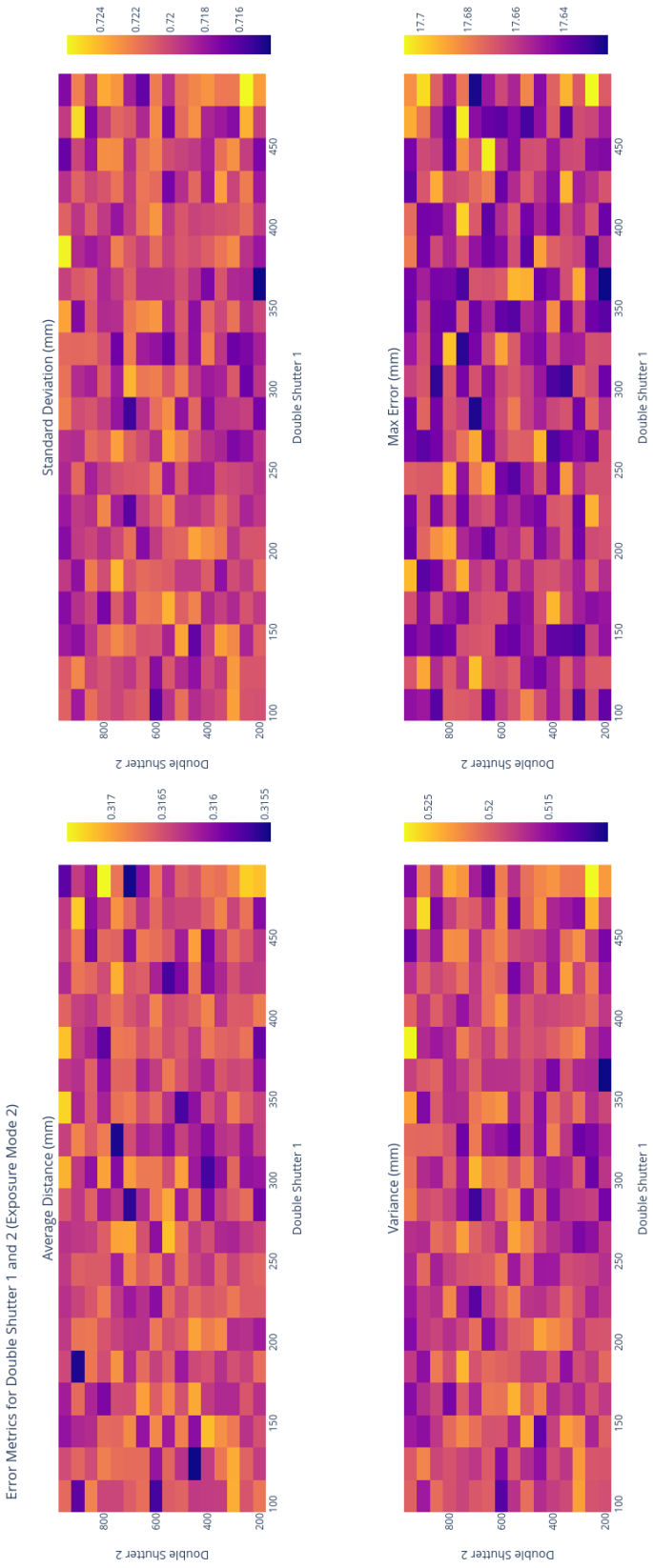

Figure A.3: Heatmap for Plate C

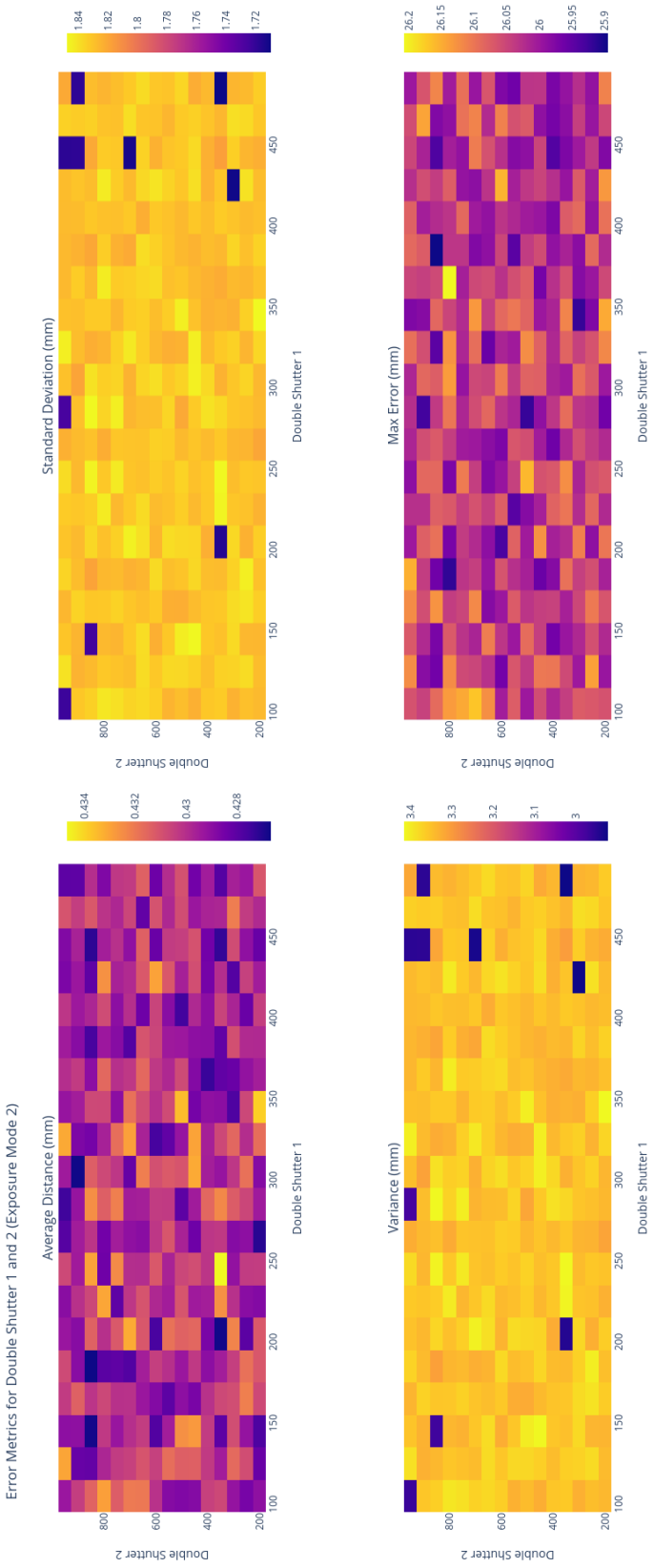

Figure A.4: Heatmap for Plate D

A.0.2 Visualization for each Exposure Mode

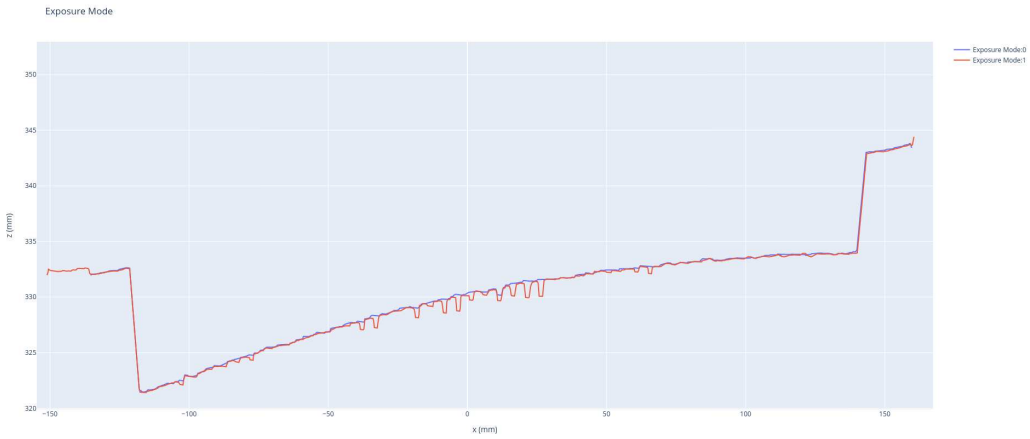

Figure A.5: Capture with Exposure mode 0 and 1 for Plate A

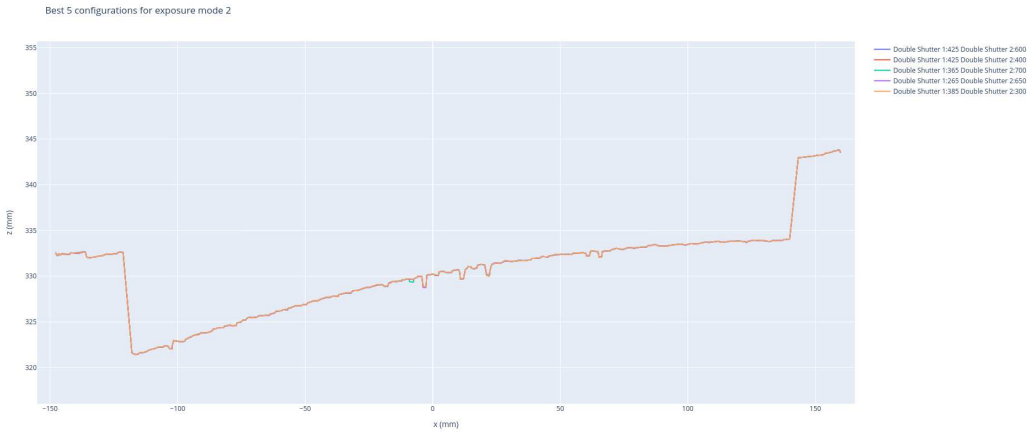

Figure A.6: Capture with different configurations with Exposure mode 2 for Plate A

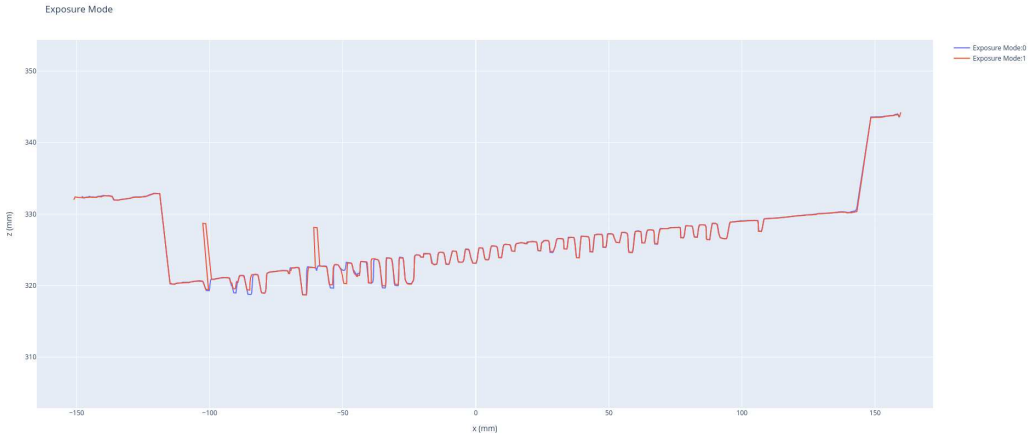

Figure A.7: Capture with Exposure mode 0 and 1 for Plate B

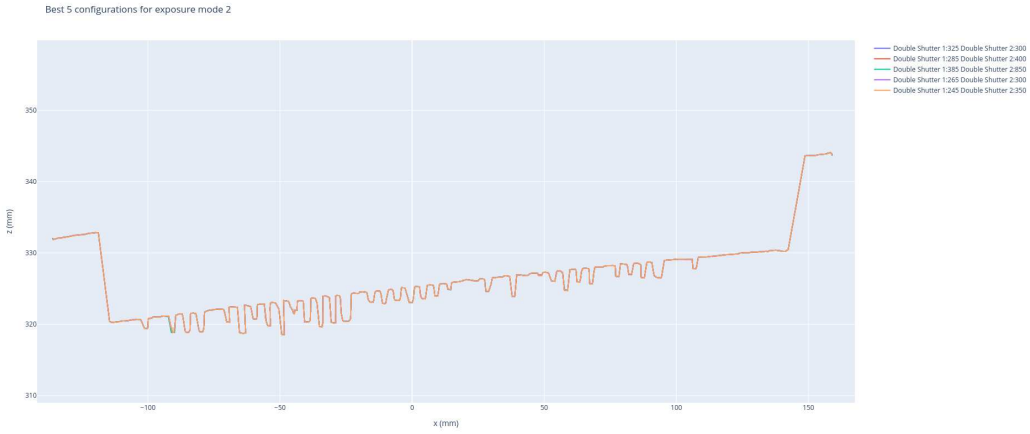

Figure A.8: Capture with different configurations with Exposure mode 2 for Plate B

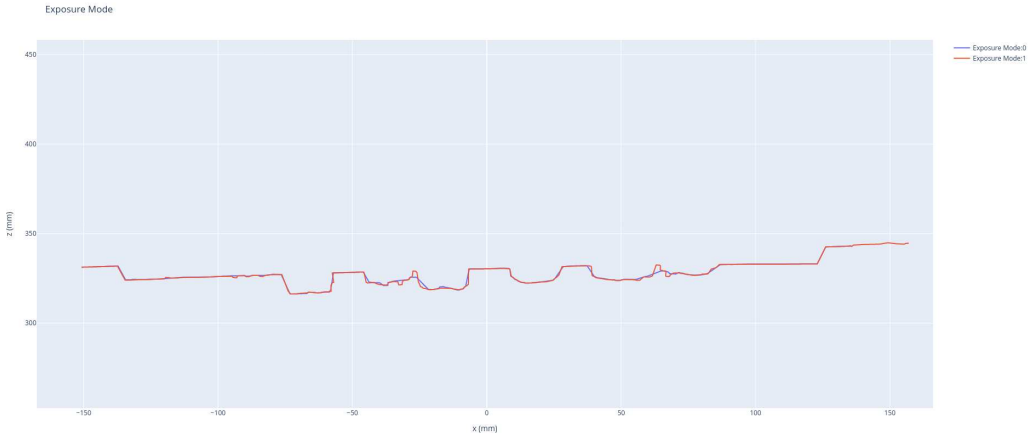

Figure A.9: Capture with Exposure mode 0 and 1 for Plate C

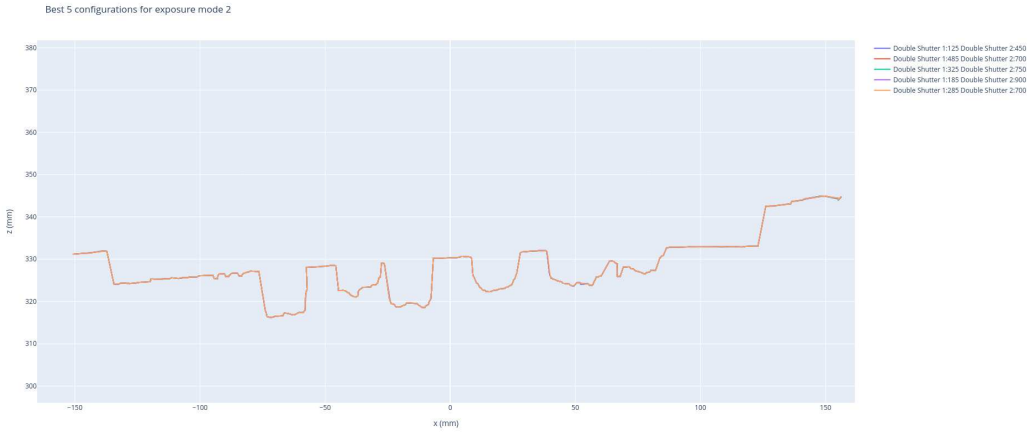

Figure A.10: Capture with different configurations with Exposure mode 2 for Plate C

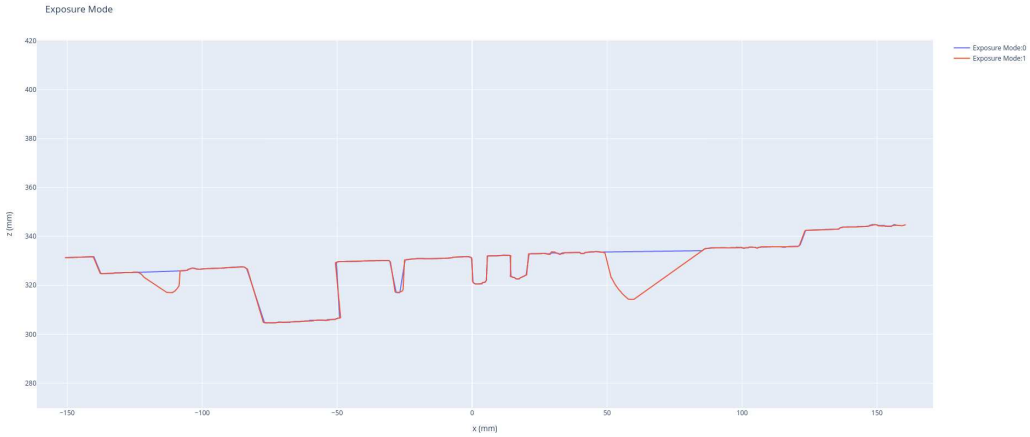

Figure A.11: Capture with Exposure mode 0 and 1 for Plate D

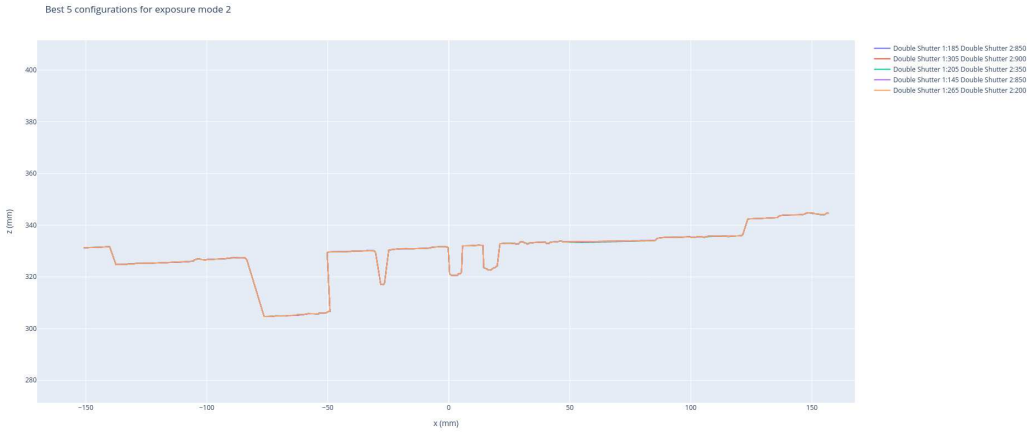

Figure A.12: Capture with different configurations with Exposure mode 2 for Plate D

Appendix B

Registration with ArUco Markers

During a summer internship in 2022, an experiment involving a rotation table in the DED system at SINTEF Manufacturing was conducted. The Zivid Two and ArUco markers were used on the rotation table for this experiment. By estimating the transformation matrix between the respective markers, the ArUco markers allowed the scene to be captured from a variety of orientations.

In order to accurately detect any geometric deviation in the 3D reconstruction of an object, a dense point cloud is needed. However, capturing the object from a single viewpoint may result in missing points on its sides and rear. To address this, three ArUco markers were strategically placed at the rotating table's corners. This experimental setup allowed for the collection of four distinct point clouds from four distinct perspectives, with each capture being a 90-degree rotation of the table, as seen in Figure B.1. This rotation allowed each marker to be identified, and its transformation estimated to perform the alignment, resulting in a dense point cloud.

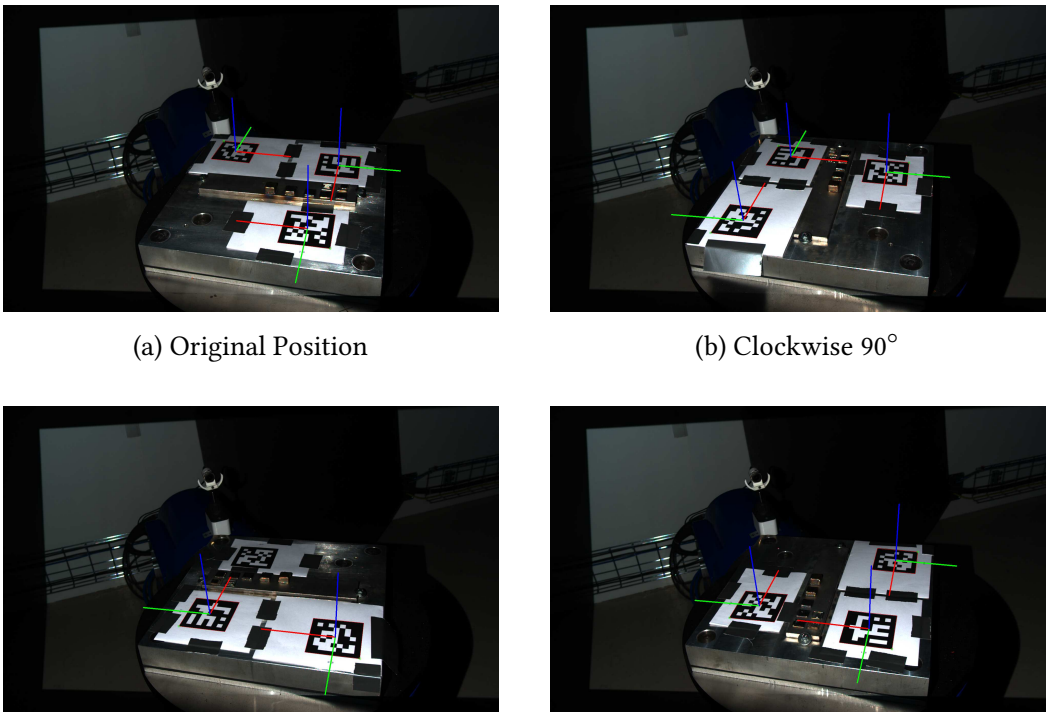

(a) Original Position (b) Clockwise 90°

(c) Clockwise 180° (d) Clockwise 270°

Figure B.1: In each rotation we can the estimate the poses of all the detected markers. Then we can easily perform an alignment without the need to search to find any correspondences. **Image Source:** [6]

Appendix C

Sub-experiment: Assessing the Maximum Build Height

The following experiment is a sub-experiment of Experiment 4, aimed to determine the maximum building height achievable with the DED system. Although a small error is expected in a DED process, the focus of this experiment was to find out the maximum building height and to see a larger height deviation. In Experiment 3, the layer height error was not significantly high, which prompted to a new sub-experiment to investigate a higher height deviation by scanning every 5th layer to detect a larger error when building, while also assessing the maximum building height.

C.1 Results

This section presents the results of the sub-experiment where a total of 50 layers were constructed with a layer height of 1.0 mm each. Considering scanning every layer takes time, it was decided to scan every 5th layer instead. However, the data was lost after the 35th layer due to the VC Nano 3D-Z's optimal working distance of 20 cm. To scan the last layer, the KUKA Industrial Robot was positioned at a

higher elevation.

The final outcomes, including the manufactured cube and 3D reconstruction, are illustrated in Figure C.1. The height deviation for each layer relative to the base is shown in Figure C.2. Only a portion of the top layer is captured at the 35th layer due to the scanner's optimal working distance limitations. This accounts for the observed low error in the height deviation of 35th layer, this fault was corrected in 50th layer. The findings clearly indicate that as the cube's height increases, so does the number of falling pixels, as illustrated in Figure C.1b. To gain deeper insights into this issue, can be further investigated in the additional projection plots from the XZ and YZ planes, which are presented in Figure C.3 and Figure C.4. These plots provide a visual representation of the issue to better understand the underlying factors contributing to the problem. These findings demonstrate that the issue with falling pixels arises due to the small surface area, which results in poor heat distribution. Consequently, the top of the cube becomes rounded. The impact of the falling pixels increases for every scan, as observed in both projection plots.

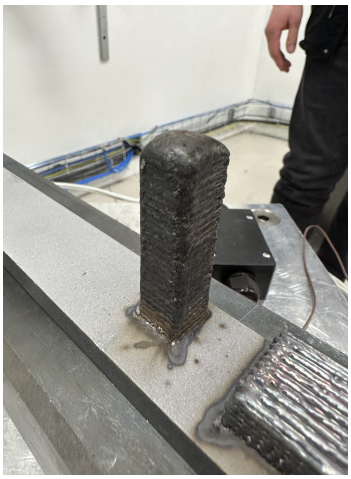

(a) The final result of the cube built with 50 layers.

(b) Scanned layers and the increasing effect of falling pixels as the height of the cube increases.

Figure C.1: Illustration of the manufactured cube and 3D reconstruciton.

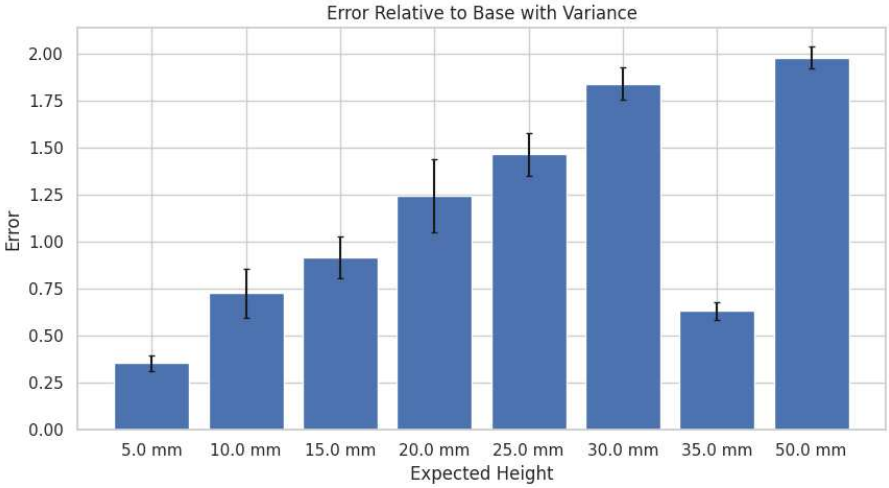

Figure C.2: For every 5th layer, measured the error relative to the base.

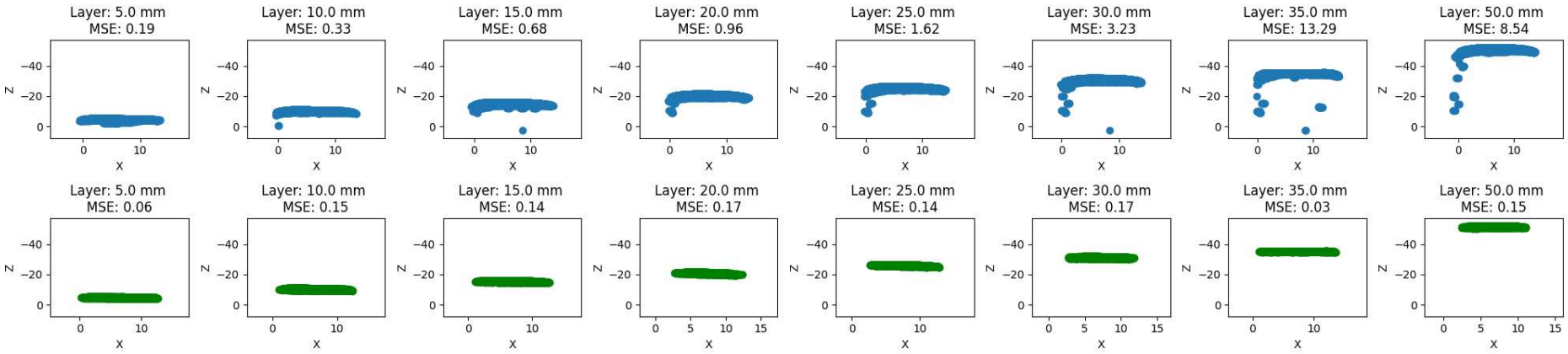

Figure C.3: Projection of XZ plane of the experiment, visualizing falling pixels. Each plot displays the expected layer height and the measured MSE, calculated as the mean of the z-coordinates. **Top:** this row presents the raw point cloud from the scan. **Bottom:** this row depicts the point cloud after RANSAC plane estimation.

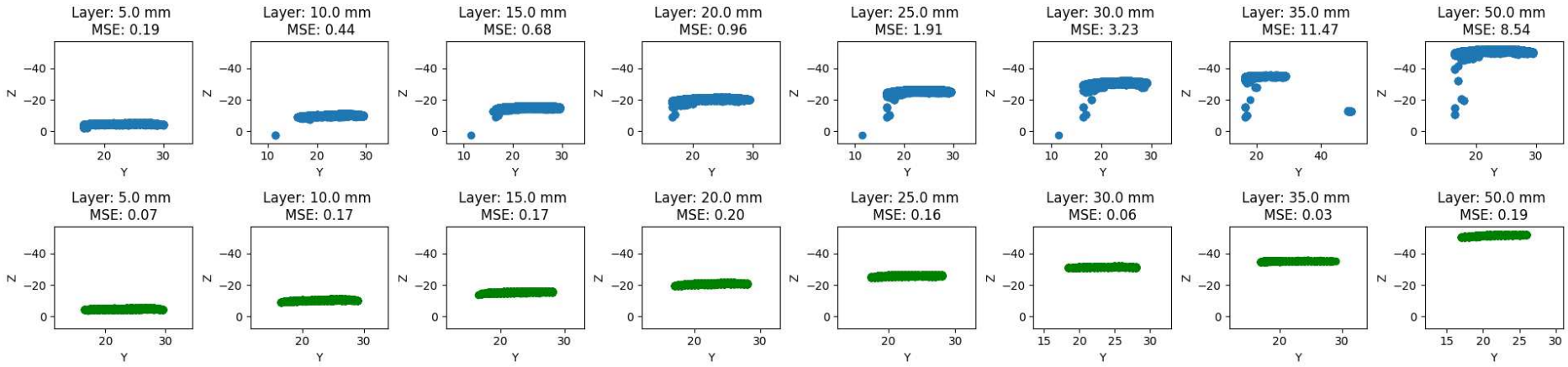

Figure C.4: Projection of YZ plane of the experiment, visualizing falling pixels. Each plot displays the expected layer height and the measured MSE, calculated as the mean of the z-coordinates. **Top:** this row presents the raw point cloud. **Bottom:** this row depicts the point cloud after RANSAC plane estimation.

Appendix D

Prior Study of Specialization Project

This section provides a brief visual overview of the preliminary studies under the specialization project[6]. Figure D.1 illustrates employing a rotation table in a simplified, replicated environment, facilitated by the use of an Arduino and a 3D printed rotation table. Despite the framework developed in the specialization project was never incorporated into the DED system, it set the foundation for further studies in this thesis.

Figure D.1: Experimental Setup: Replicating an Environment with a Rotation Table and VC Nano 3D-Z for 3D Reconstruction.

Appendix E

RANSAC Plane Alignment

This subsequent pseudocode presents the practical application of the RANSAC algorithm, specifically for the task of aligning the manufactured layers based on the base plate. Algorithm 3 shows the process of obtaining the rotation matrix from plane segmentation by explicitly calculating the transformation of fitted plane based on the normal using the RANSAC algorithm.

Algorithm 3 RANSAC Plane Alignment of XY Plane

Require: Point cloud $P = \{p_1, \ldots, p_n\}$
Ensure: Rotated P and rotation_matrix
1: Initialize RANSAC regressor
2: Fit RANSAC model to (x, y) pairs predicting z
3: Get coefficients a, b, and intercept d from the fitted RANSAC model
4: Set normal = $[a, b, -1]$
5: Set normal_xy = $[0, 0, 1]$
6: Compute w = cross_product(normal, normal_xy)
7: Compute cos_theta = $\frac{\text{dot\_product(normal, normal\_xy)}}{\text{norm(normal)} \times \text{norm(normal\_xy)}}$
8: Compute sin_theta = $\sqrt{1 - \text{cos\_theta}^2}$
9: Construct skew-symmetric matrix wx_matrix = $\begin{bmatrix} 0 & -w[2] & w[1] \\ w[2] & 0 & -w[0] \\ -w[1] & w[0] & 0 \end{bmatrix}$
10: Calculate rotation_matrix using Rodrigues' rotation formula
11: Rotate P using rotation_matrix around the origin
12: **return** Rotated P and rotation_matrix

Appendix F

Draft of Conference Paper

The work in this master's thesis will be turned into a conference paper to be submitted at the ICCMA 2023 conference.

Layer Height Estimation using Laser Line Scanners for Closed-Loop Directed Energy Deposition

1st Salar Adel
Dept. of Computer Science
Norwegian University of Science and Technology
Trondheim, Norway
salar@stud.ntnu.no

2nd Eirik B. Njaastad
Dept. of Production Technology
SINTEF Manufacturing
Trondheim, Norway
eirik.njaastad@sintef.no

3rd Mathias Hauan Arbo
Dept. of Production Technology
SINTEF Manufacturing
Trondheim, Norway
email address or ORCID

4th Frank Lindseth
Dept. of Computer Science
Norwegian University of Science and Technology
Trondheim, Norway
email address or ORCID

***Abstract*—Enhancing the geometric accuracy of additive manufacturing (AM) processes remains a vital challenge, particularly in the context of directed energy deposition (DED). This paper investigates using a laser line scanner for real-time layer height estimation during the DED process. The proposed system offers [...], enabling adaptive control and quality assurance in DED manufacturing. Experimental results demonstrate the effectiveness of the laser line scanner in achieving higher geometric accuracy in printed objects. The findings contribute to advancing quality control methodologies in AM, paving the way for broader adoption of DED technology.**

***Index Terms*—Computer vision, process control, closed loop systems**

I. Introduction

Additive manufacturing (AM) is an effective and promising manufacturing technology for quick prototyping and production technology. Achieving the desired geometry using AM requires either an accurate model of the deposition process for all possible material and geometry situations, allowing for an open-loop approach to depositing the material, or a closed-loop approach where sensor feedback of the layers as-built defines how the next layer is applied.

An industrially relevant AM process that accepts a wide range of metals is Directed Energy Deposition (DED). The DED process involves melting and fusing of metallic wire and/or powder using a thermal energy source like a laser, but its practical application is not without challenges. A critical aspect is achieving high geometric accuracy to achieve precise specifications, a requirement in various fields from aerospace to medical sectors. Although advances in AM have increased demand for its applications, regulating the geometry of deposited objects during the AM process remains a significant problem. As a result, significant breakthroughs in quality assurance and control are required to bring AM into widespread use [3, 4].

The work reported in this paper is based on activities within centre for research based innovation SFI Manufacturing in Norway, and is partially funded by the Research Council of Norway under contract number 237900.

Multiple methods have been tested to improve AM processes, including computer vision technology and structured light sensors for online monitoring, error detection, and correction during manufacturing. Charalampous et al. [5] employed a method for error detection in a Cartesian material extrusion printer using a structured light camera at a fixed position. In this research, a point cloud of the top layer was created, compared to a simulated point cloud, and an error was calculated using mean squared error (MSE). The suggested method primarily relies on point cloud registration methods, known for being stuck in local minima. Furthermore, the technique is based on the use of KD Tree [2] to build a tree in order to determine if the MSE is above a specific error threshold. This procedure can be difficult because it relies on constructing a tree and comparing distances after every layer. Methods more similar to DED processes can be found in the study by Garmendia et al. [7] which used structured light from a fixed position to measure the height relative to the build platform. After a specific number of layers was built, and the height deviation was calculated and layers were either removed or added to better achieve the desired CAD model. However, this method alters the geometrical characteristics of the printed object, which can cause inaccurate representation of the object and have problems with curvature overhangs. Zhou et al. [8] showcased a framework for in-process height control in a DED process using a camera to monitor the height and adjusting process parameters to optimize the building process. This was done by locating the highest pixel in the melt pool and then measure the distance to the nozzle. Using the differences, a new working distance between the nozzle and build plate was estimated, which resulted in a more accurate cube.

Computer vision has been illustrated as good method for feedback in the DED process. There are a lot of existing structured light-based methods that projects binary patterns [1] to retrieve point cloud from a scene, but the dimensional accuracy of simple laser line scanners are higher, although it only receives single profile scans. Most structured light

scanners captures diffuse reflection and use a method such as filter to reduce the outlier generated from specular reflection, but surface finish, material properties, and geometry affect the quality of the scan.

A DED process is capable of processing a number of metals with a wide range of reflection properties. As a result, this article describes a process for optimizing the scanner parameters based on a set of error metrics without considering the specific material being scanned. The resulting parameters are used to establish a scanning system for layer-by-layer monitoring of the built geometry. The layer is used to estimate the height layer for use with closed-loop control of the DED process.

II. Experimental Setup

In order to examine the two aspect of the research area, two different experimental setups were designed. Both setups use the VC Nano 3D-Z, a scanner based on structured light using a laser line.

A. Experiment 1

The first experimental setup involves testing a variety of plates with distinct shapes and materials manufactured from a DED process, as seen in Table I. It is important to note that some of the base plates have been grit blasted, a process that can result in more texture surfaces. In this setup, the VC Nano 3D-Z scanner is set to scan each plate iterating through a predetermined set of parameter configurations chosen for this experiment. These parameters include shutter time, RLC threshold and a set of three different exposure modes. To identify ideal parameter configurations, a set of error metrics is defined by using average distance between consecutive pairs of points, standard deviation between each consecutive point and maximum height variations based on the Z-coordinates. By iterating through different parameter configurations, the setup aims to find an ideal set of parameters that minimizes outliers generated from specular reflection.

TABLE I: Metal Types and their corresponding Base Metals for every Plate sampled for the experiment.

Plate	Top	Base
A	Carbon Steel	Carbon Steel
B	Aluminum	Aluminum (Grit blasted)
C	Bronze	Carbon Steel
D	Stainless Steel	Carbon Steel (Grit blasted)

1) Choice of Parameter Configurations: The VC Nano 3D-Z has a set of customizable parameter setups, which must be optimized to improve scan quality. The geometric shape and material characteristics of the object being scanned determine the configured values of certain objects. Due to the diversity of structured light, most of the time these parameters has to be adjusted manually. A robust and automated method of configuring the scanner to specific objects are required to reduce setup time. For the purpose of this experiment, we have focused on the adjusting of three parameters: shutter time, RLC threshold, and a selection of three distinct exposure modes which is described in Table II.

TABLE II: Experimental Configurations of VC Nano 3D-Z

Configuration	Description
Shutter Time [μs]	The duration of the camera's exposure to capture the image of the laser line.
RLC Threshold	The threshold value set for the RLC algorithm to detect the laser line.
Exposure Mode	The camera's exposure configuration, which includes three options: **AUTO EXPOSURE**: uses a fixed shutter time, **FIXED EXPOSURE**: Trying to find an estimate of an optimal shutter time, and **DOUBLE EXPOSURE**: Uses two extra shutter times.

2) Choice of Error Metric: Further, optimizing the scanner requires a set of error metric to distinguish suboptimal and optimal configurations. A number of statistically based error metrics were chosen, with the objective of identifying an ideal output by iterating through a range of configurations. The output is based on the following error metric: *average distance*, *standard deviation*, and *maximum z distance from mean*.

The average distance uses the Euclidean distance between each consecutive point pairs (x, z) is defined as

$$E_{avg} = \frac{1}{N}\sum_{j=1}^{N-1}\sqrt{(\mathrm{x}_{j+1}-\mathrm{x}_j)^2+(\mathrm{z}_{j+1}-\mathrm{z}_j)^2} \tag{1}$$

where N is the total number of points.

Similarly, the standard deviation is calculated using

$$E_{std} = \mathrm{std}\left(\left\{\sqrt{(\mathrm{x}_{j+1}-\mathrm{x}_j)^2+(\mathrm{z}_{j+1}-\mathrm{z}_j)^2}\right\}_{j=1}^{N-1}\right) \tag{2}$$

where $\{\}$ are used to denote the collection of distances.

Lastly, the maximum z distance from mean is defined as

$$E_{z,max} = \max_{j=1}^{N}\left|\mathrm{z}_j - \frac{1}{N}\sum_{i=1}^{N}\mathrm{z}_i\right| \tag{3}$$

and attempts to capture the situation when reflection issues result in few but significant outliers that are far from the true surface line.

B. Experiment 2

This experiment is conducted based on a MELTIO laser-based DED process integrated into a multi-axis KUKA Industrial robot, as seen in Fig.1. Using the robot's tool mount, the scanner can be integrated to create a scanning path for inspection by producing 3D reconstruction of the top layer. In this case, a simple scanning path was constructed that translates step-wise 0.5 mm along the x-axis. By performing an initial scan of the build plate it is possible to measure the height deviation relative to the build plate. In this experiment, a cube composed of ten layers is constructed, with a desired layer height of 1.0 mm. A scan of the top layer is performed

after each layer is deposited. The substrate and the manufactured material for this experiment is carbon steel. The scan provides a dense point cloud of the surface. Two measures that can be used to inform a control strategy are the height layer comparison using mean and variance of the scanned points, and by fitting a plane to the top layer and comparing the height differences between

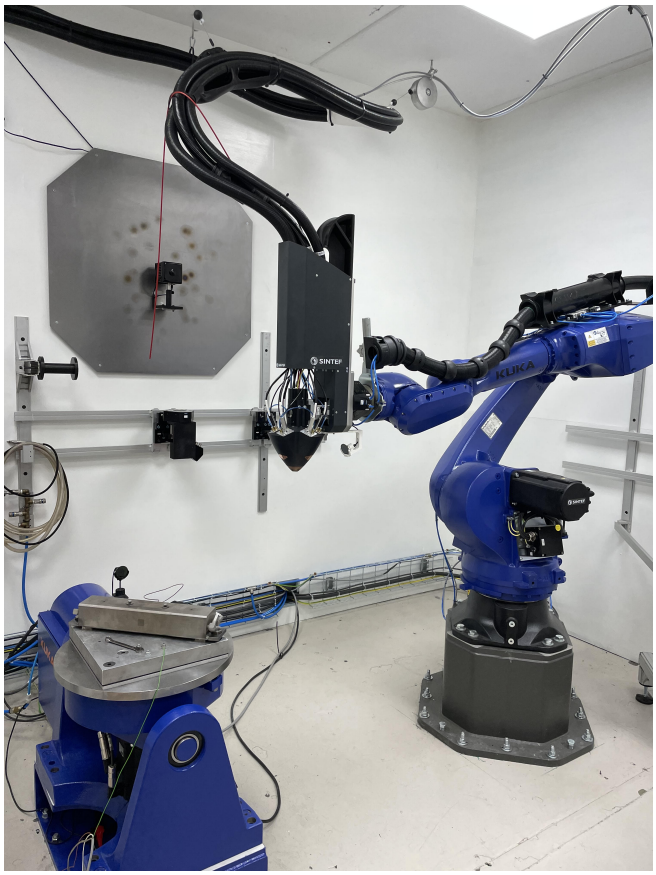

Fig. 1: The MELTIO system integrated with a KUKA Industrial robot for DED processes.

III. Results

A. Experiment 1

Table III presents the outcomes from varying the shutter time while keeping the remaining parameters at their default values. The three best results for each were selected to examine substantial variations when identifying the optimal shutter time based on the error metrics. In contrast to Plates A and C, which require substantially longer shutter times, Plates B and D have lower ideal shutter times. This finding suggests that the Plates B and D's materials have a high reflectivity, necessitating shorter shutter periods.

A further analysis of Plate B was conducted to confirm the parameter configurations were not arbitrary. The most ideal shutter time discovered was 3800 μs. Fig.2 demonstrates the disparities caused by the use of longer shutter duration, as well as the outliers they produce. Furthermore, the higher shutter time comparisons show an increase in reflection, which result in significant differences in the z-coordinates.

TABLE III: Best shutter times for each plate

Plate	Shutter time [μs]	Avg. dist. [mm]	SD [mm]	Var [mm]	Max. error [mm]
A	**9950**	**0.33**	**0.61**	**0.38**	**13.31**
	9500	0.33	0.61	0.38	13.31
	8750	0.33	0.61	0.38	13.31
B	**3800**	**0.32**	**0.58**	**0.34**	**17.78**
	3950	0.32	0.58	0.34	17.78
	3350	0.32	0.58	0.34	17.79
C	**9950**	**0.36**	**0.93**	**0.87**	**15.82**
	8750	0.36	0.93	0.87	15.82
	9500	0.36	0.94	0.88	15.80
D	**2600**	**0.51**	**2.03**	**4.13**	**13.53**
	2450	0.52	2.02	4.10	13.62
	1550	0.51	2.06	4.24	13.55

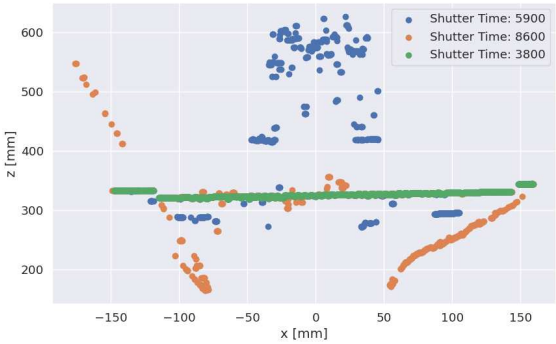

Fig. 2: Various shutter time configurations tested for Plate B, finding the optimal value of 3800 μs.

Table IV presents the optimal parameters for the RLC threshold, where the shutter time was selected based on the best values for each plate in Table III. It was observed before the experiment that values below 20 and above 40 gave not the best results. Therefore, these results were fine-tuned between this range. It can be observed that the threshold value stays relatively similar, with an exception to Plate D. Plate D exhibited the lowest threshold value, which could be the inherently low reflecting characteristics of its, stainless steel.

Table V presents the outcomes of the three different exposure mode compared with the optimal shutter time and RLC threshold from prior findings. For most of the plates, exposure mode 1 was discovered as the ideal one to use. In contrast, Plate B found that the best exposure mode was 0. The wide range of materials used in the DED process and the build plate might highly differ in reflection. The Plate D consist of a highly reflective build plate Carbon steel and a lower reflection manufactured material stainless steel.

TABLE IV: Best RLC threshold for each plate.

Plate	RLC thresh.	Avg. dist. [mm]	SD [mm]	Var [mm]	Max. error [mm]
	30	**0.32**	**0.61**	**0.38**	**13.30**
	29	0.33	0.65	0.42	13.32
A	31	0.33	0.63	0.40	13.29
	28	**0.31**	**0.56**	**0.32**	**17.78**
	30	0.32	0.58	0.34	17.80
B	29	0.32	0.58	0.33	17.78
	29	**0.35**	**0.89**	**0.80**	**15.88**
	30	0.36	0.93	0.86	15.83
C	31	0.36	0.95	0.91	15.79
	20	**0.43**	**1.85**	**3.41**	**25.83**
	21	0.44	1.88	3.53	26.04
D	22	0.46	1.93	3.72	26.25

B. Experiment 2

Figure 3 presents the final result of the cube manufactured, where each top layer was scanned, including the build plate. Each layer height was approximately was set to be 1.0 mm.

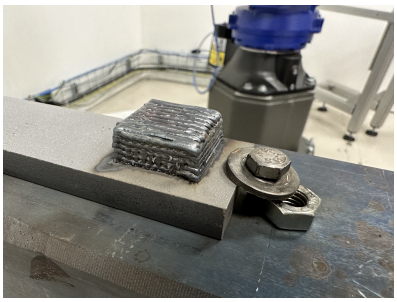

Fig. 3: Final result of 10 layered cube with 1.0 mm layer height manufactured in Carbon Steel.

Figure 4 presents the results of scanning each top layer. It can be seen some flucatations is this is because of the nature of wire-arc based DED processes have lower resolution when manufacturing small objects, in this case $14 \times 14 \times 10$ mm. The mean height of each layer is calculated relative to the build plate.

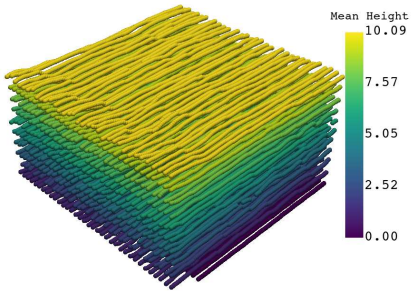

Fig. 4: Height Layer Comparisons using mean

Figure 5 illustrates the height deviation from each layer calculated the mean of the height of each layer, but also the variances to illustrate fluctuations of each top layer. The first top layer has a high error, but slowly decreases as the building progresses. This might be a result of the solidification between the build plate and first layer.

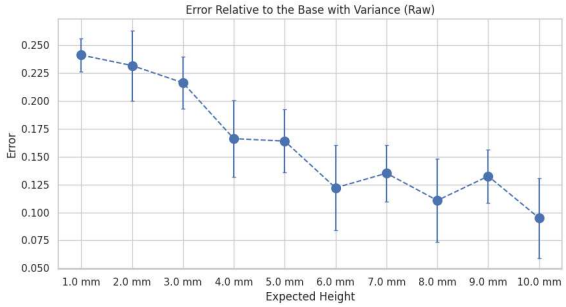

Fig. 5: Height Layer Comparisons using mean

Figure 6 presents the results from comparing each consecutive layer. The solidification can be better seen here that the error is relatively higher but decreases and stays relatively the same throughout the process. Because of the large variation in fluations, the Random sample consensus (RANSAC) algorithm [6] was used to estimate a plane on each top layer. This was done since comparing layer height are done by planar surfaces and specially when comparing the height with the Standard Tessellation Language (STL) model, which is a format that most AM system process to build objects.

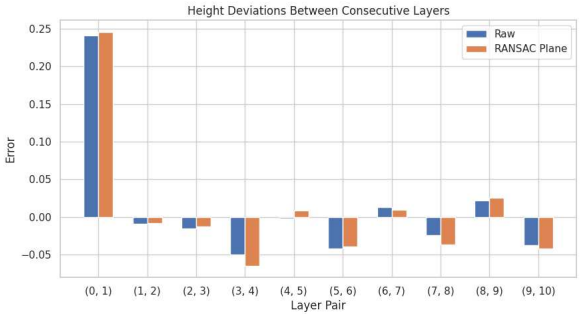

Fig. 6: Assessing height differences between consecutive layer pairs, where the expected height between layers is 1.0 mm.

IV. Discussion

A. Parameter Choices

B. Path Optimization

V. Conclusion

Acknowledgment

The authors would like to thank Trond Arne Hassel for his contributions to the experimental setup.

TABLE V: Best exposure modes for each plate.

Plate	Exposure mode	Shutter time	Double shutter 1	Double shutter 2	RLC thresh.	Avg. dist. [mm]	SD [mm]	Var [mm]	Max. error [mm]
A	0	9950	-	-	30	0.33	0.61	0.38	13.31
	1	**-**	**-**	**-**	**30**	**0.27**	**0.44**	**0.19**	**13.99**
	2	-	425	600	30	0.28	0.49	0.24	13.32
B	**0**	**3800**	**-**	**-**	**28**	**0.31**	**0.56**	**0.31**	**17.78**
	1	-	-	-	28	0.33	0.67	0.45	17.85
	2	-	325	300	28	0.33	0.65	0.43	18.03
C	0	9950	-	-	29	0.35	0.88	0.78	15.89
	1	**-**	**-**	**-**	**29**	**0.30**	**0.61**	**0.37**	**16.97**
	2	-	125	450	29	0.32	0.72	0.52	17.64
D	0	2600	-	-	20	0.43	1.85	3.41	25.76
	1	**-**	**-**	**-**	**20**	**0.39**	**1.57**	**2.46**	**23.86**
	2	-	185	850	20	0.43	1.82	3.31	25.96

REFERENCES

[1] Tyler Bell, Beiwen Li, and Song Zhang. "Structured light techniques and applications". In: *Wiley Encyclopedia of Electrical and Electronics Engineering* (1999), pp. 1–24.

[2] Jon Louis Bentley. "Multidimensional binary search trees used for associative searching". In: *Communications of the ACM* 18.9 (1975), pp. 509–517.

[3] Eden Binega et al. "Online geometry monitoring during directed energy deposition additive manufacturing using laser line scanning". In: *Precision Engineering* 73 (2022), pp. 104–114.

[4] Frédéric Cabanettes et al. "Topography of as built surfaces generated in metal additive manufacturing: A multi scale analysis from form to roughness". In: *Precision Engineering* 52 (2018), pp. 249–265.

[5] Paschalis Charalampous et al. "Vision-based real-time monitoring of extrusion additive manufacturing processes for automatic manufacturing error detection". In: *The International Journal of Advanced Manufacturing Technology* 115 (2021), pp. 3859–3872.

[6] Martin A Fischler and Robert C Bolles. "Random sample consensus: a paradigm for model fitting with applications to image analysis and automated cartography". In: *Communications of the ACM* 24.6 (1981), pp. 381–395.

[7] Iker Garmendia et al. "In-process height control during laser metal deposition based on structured light 3D scanning". In: *Procedia Cirp* 68 (2018), pp. 375–380.

[8] Vivian Zhou et al. "Development of a height control system using a dynamic powder splitter for directed energy deposition (DED) additive manufacturing". In: *Progress in Additive Manufacturing* 7.5 (2022), pp. 1085–1092.

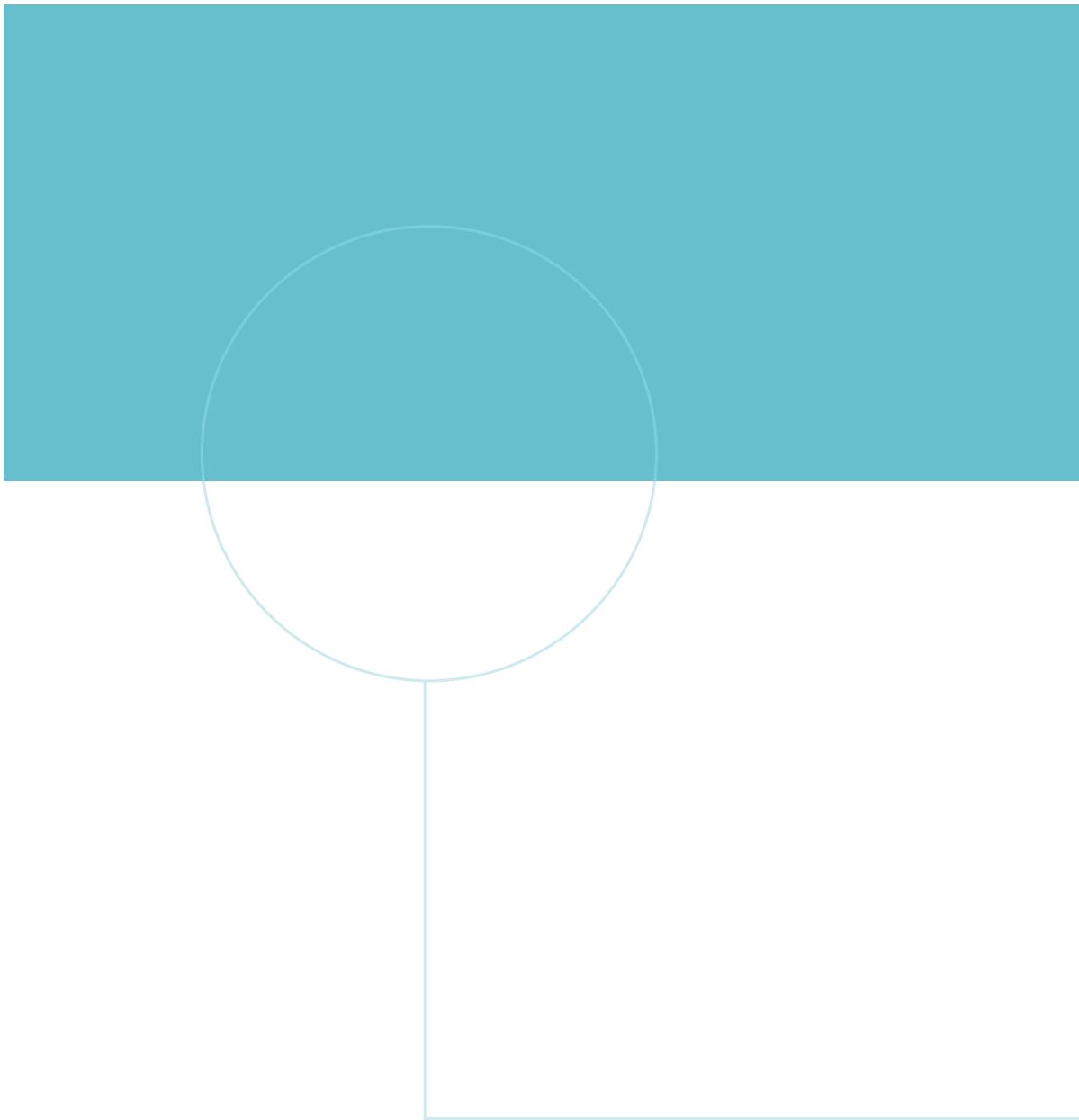

NTNU

Norwegian University of
Science and Technology